

DISSERTATION

MULTI-SCALE INTERACTIONS LEADING TO TROPICAL CYCLOGENESIS  
IN SHEARED ENVIRONMENTS

Submitted by

Chaehyeon Chelsea Nam

Department of Atmospheric Science

In partial fulfillment of the requirements

For the Degree of Doctor of Philosophy

Colorado State University

Fort Collins, Colorado

Fall 2021

Doctoral Committee:

Advisor: Michael M. Bell

Steven A. Rutledge

Eric D. Maloney

Steven C. Reising

Copyright by Chaehyeon Chelsea Nam 2021

All Rights Reserved

## ABSTRACT

# MULTI-SCALE INTERACTIONS LEADING TO TROPICAL CYCLOGENESIS IN SHEARED ENVIRONMENTS

To be, or not to be, that is the question of tropical cyclogenesis. Only a small fraction of tropical disturbances eventually develop into tropical cyclones (TCs). Accurate forecasts of tropical cyclogenesis are difficult because TC development involves a wide range of scales from the stochastic convective scale to a quasi-balanced large-scale flow. This dissertation examines the factors that increase uncertainty around the multi-scale tropical cyclogenesis problem, namely, vertical wind shear (VWS), environmental humidity, and convective organization. These factors were explored using multiple data sources including observations such as dual-Doppler radar, dropsonde soundings, and satellite data for mesoscale case studies, reanalyses data for synoptic and climatological analysis, and extensive ensemble mesoscale modeling for controlled experiments.

First, this dissertation presents a detailed observational analysis for multi-scale processes around an incipient wave pouch of Hagupit (2008) that survived through strong VWS and underwent TC genesis. The strong deep-layer VWS ( $> 20 \text{ m s}^{-1}$ ) had a negative impact on the development through misalignment of the low and mid-level circulations and dry air intrusion. However, the low-level circulation persisted and the system ultimately formed into a tropical cyclone after it had left the high-shear zone. Here we propose that a key process that enabled the pre-depression to survive through the upper-tropospheric trough interaction was persistent vorticity amplification on the meso- $\gamma$  scale that was aggregated on the meso- $\alpha$  scale within the wave pouch.

In the second part, twelve sets of Weather Research and Forecasting ensemble simulations were created to examine the combined impacts of VWS, environmental moisture, and the structure of the precursor vortex on the uncertainty of TC genesis. Here we hypothesized that the combination of moderate shear and dry air makes an unstable condition for a vortex to intensify or decay, which

implies that TC genesis in such environments may be intrinsically unpredictable in a deterministic sense. Based on the close examination of selected ensemble members and statistical analysis of geometric probability distribution and time-lagged correlations for all ensemble sets, we propose a theoretical pyramid diagram of the five processes leading to TC genesis in sheared and dry environments. First, inside their low-level circulations, deep convection emerged over a wider area. Second, a new smaller scale mid-level vortex formed inside the deep convection where the pre-existing mid-level vortex was carried away by VWS. Third, the mid-level vortex and low-level vortex went through a vertical alignment process. Fourth, with sustained vortex alignment, convection organized near the low-level center. Fifth, central pressure fell and wind speed increased; and the system reached tropical cyclone intensity. The results suggest that all successfully developing TCs share a common set of precursor events that lead to TC genesis, while a deficiency in any of the precursor events leads to a failure of genesis.

In the third part, we investigated the likelihood of subsequent TC genesis from the "monsoon tail" rainband for TCs in the monsoonal area of the western North Pacific (WNP). The monsoon tail rainband—an elongated rainband in the southwestern quadrant of the TC—is shown to be a common feature for TCs in the WNP due to the climatological northeasterly VWS. Variations in the convective activity are shown to be related to the strength of the low-level and upper-level monsoonal flow on synoptic and seasonal timescales, with VWS having the highest correlation to cold cloud tops in the southwest quadrant. Some monsoon tail rainbands sustain convective organization even after they separated from the pre-existing TCs, but despite the enhanced convective activity, the persistent VWS that produced the rainbands was an overriding negative factor that inhibits genesis.

This dissertation provides a detailed look at the complex interactions between VWS and the incipient TC depending on spatial scales, the vertical depth of shear, environmental moisture, and the structure of the TC vortex. The findings herein improve our process-based understanding of why moderate VWS, especially in combination with environmental dry air, produces unstable and uncertain conditions for TC genesis.

## ACKNOWLEDGEMENTS

I would first like to thank my advisor, Dr. Michael Bell. During the four years and three months of my Ph.D., I had multiple field campaign experiences, teaching opportunities, and freedom to explore diverse research projects, and I am grateful for my advisor's guidance and support through each stage of the process. I could grow as a researcher and a teacher thanks to him.

I appreciate my committee members, Dr. Steve Rutledge and Dr. Eric Maloney, for taking their time to serve on my Ph.D. committee and for all their feedback. I appreciate my outside committee member, Dr. Steve Reising, for stepping in to help out serving as the outside committee. Thank you to Dr. Imme Ebert-Uphoff for serving as an outside committee member for my preliminary exam and the proposal meeting. Thank you to Dr. Dandan Tao for providing feedback on the WRF ensemble study and Dr. Phil Klotzbath for contributing to the monsoon tail chapter.

This Ph.D. research was funded by the National Science Foundation award AGS-1701225, Office of Naval Research awards N000141613033 and N000142012069. Computational resources for Chapter 3 were provided by XSEDE allocation TG-ATM190001.

I am so thankful for the Bell Research Group, all the past and current members. Special thank you to Jhordanne and Ting-Yu for accompanying me on walks when I needed "ventilation." I want to thank Erin, Yoonjin and Dr. Yoo-Jeong Noh because I could make a smooth transition thanks to their help when I first moved from Seoul to Fort Collins. I'd also thank Dr. Doo-Sun Park and Dr. Minhee Chang for the guidance and discussion continued from my Master's time.

I thank God every day for my husband, Juni, since he has been a ray of sunshine even on my darkest days. I am grateful for my family in South Korea. My mom and dad have always believed in me and I know that became my source of confidence. I appreciate Trent and Joan Sauder for their love and prayers. Thank you to Simchan, Jangho, and Jinkyul. Friends from Bridges and the Fort Collins Korean Church have been a great support for me as well. I would not have been able to finish all this work without these precious people in my life.

## TABLE OF CONTENTS

<b>ABSTRACT . . . . .</b>	<b>ii</b>
<b>ACKNOWLEDGEMENTS . . . . .</b>	<b>iv</b>
<b>LIST OF TABLES . . . . .</b>	<b>vii</b>
<b>LIST OF FIGURES . . . . .</b>	<b>viii</b>
<b>Chapter 1      Introduction . . . . .</b>	<b>1</b>
1.1      Motivation . . . . .	1
1.2      Literature Review . . . . .	2
1.2.1      Large scale: thermodynamic conditions for tropical cyclogenesis . . . . .	3
1.2.2      Synoptic scale: pre-existing disturbance . . . . .	3
1.2.3      Mesoscale: tropical cyclogenesis paradigms . . . . .	4
1.2.4      The meeting point of multi-scale processes: wave pouch theory . . . . .	5
1.2.5      The deal breaker: vertical wind shear . . . . .	6
1.3      Dissertation Objectives and Outline . . . . .	8
<b>Chapter 2      Multi-scale shear impacts during the genesis of Hagupit (2008) . . . . .</b>	<b>11</b>
2.1      Introduction . . . . .	11
2.2      Data and Methods . . . . .	14
2.3      Results . . . . .	16
2.3.1      Large-scale influences: trough influences on wave pouch evolution . . . . .	16
2.3.2      Upscale vortex merger process: vortical convection in a sheared pre-depression . . . . .	24
2.4      Discussion and Conclusions . . . . .	36
<b>Chapter 3      Bifurcation points for tropical cyclone genesis in sheared and dry environments . . . . .</b>	<b>42</b>
3.1      Introduction . . . . .	42
3.2      Experimental Design and Model Setup . . . . .	44
3.3      Results . . . . .	48
3.3.1      Overview of TC development . . . . .	48
3.3.2      Probabilistic approach to TC genesis . . . . .	57
3.3.3      Time-lagged correlation analysis . . . . .	61
3.3.4      Sensitivity to vortex structure . . . . .	66
3.4      Discussion and Conclusions . . . . .	72
<b>Chapter 4      Monsoon tail rainband and its effects on subsequent tropical cyclogenesis . . . . .</b>	<b>76</b>
4.1      Introduction . . . . .	76
4.2      Data and Methods . . . . .	80
4.2.1      Data . . . . .	80
4.2.2      Methods . . . . .	82

4.3	Results . . . . .	84
4.3.1	Climatology of "monsoon tail" rainbands . . . . .	84
4.3.2	Interannual variability of the "monsoon tail" rainband . . . . .	89
4.3.3	Subsequent tropical cyclogenesis from the "Monsoon tail" rainband . . .	94
4.4	Discussion and Conclusion . . . . .	101
Chapter 5	Conclusions . . . . .	104
References	. . . . .	107

## LIST OF TABLES

3.1 List of experiments with corresponding experimental setups. . . . .	45
---	----

## LIST OF FIGURES

1.1	Scale-dependence of tropical cyclone dynamics adapted from Ooyama (1982). Darkened area implies the existence of cloud-organizing mesoscales within the deterministic regime of the balanced flow. . . . .	2
1.2	Conceptual diagram of how tropical storm forms in a wave pouch (adapted from Fig. 3 of Wang et al. (2010)) . . . . .	6
2.1	Vorticity at 850 hPa around pre-depression Hagupit from 0000 UTC 12 September to 0000 UTC 19 September. Red boxes are $6^\circ \times 6^\circ$ centered on Hagupit's wave pouch at each time. Contoured in gray scale is potential vorticity field at 200 hPa. . . . .	17
2.2	MTSAT infrared water vapor channel (near $6.7 \mu\text{m}$ ) brightness temperature showing pre-depression Hagupit and upper-level trough to the northeast at 2335 UTC 13 September. The red box is $6^\circ \times 6^\circ$ around the pouch center. . . . .	18
2.3	Streamlines (black contour) and vertical relative vorticity (shading) from 12 to 15 September at 500 hPa and 850 hPa around Hagupit's wave pouch. Green lines indicate the critical latitude (where the zonal flow is equal to the wave phase speed) and blue lines indicate the wave trough axis (where the meridional velocity is zero) at 850 hPa. The center of the wave pouch is defined as the intersection of the green and blue lines. The red box is $6^\circ \times 6^\circ$ around the pouch center. . . . .	19
2.4	As in Fig. 2.3 from 16 to 19 September. . . . .	20
2.5	Time-series of vertical structure inside Hagupit's wave pouch (12 hourly averaged over $6^\circ \times 6^\circ$ box): <b>a</b> ) circulation, <b>b</b> ) relative humidity, and <b>c</b> ) vertical wind shear (VWS) magnitude (color) and wind direction (vector) from 00 UTC 10 September to 12 UTC 19 September. VWS was calculated between each pressure level minus wind at 850 hPa. The black line indicates the aircraft mission (00 UTC 14 September), and the white dotted line marks when Hagupit was designated as a tropical depression by the Joint Typhoon Warning Center (00 UTC 19 September). . . . .	22
2.6	Thermodynamic and dynamic quantities averaged over the box centered on the wave pouch center as a function of time (from 10 September to 19 September) and box length; <b>a</b> ) Circulation at 850 hPa, <b>b</b> ) 200 hPa – 850 hPa vertical wind shear, <b>c</b> ) relative vorticity at 850 hPa, <b>d</b> ) column water vapor, <b>e</b> ) relative vorticity at 500 hPa, and <b>f</b> ) median brightness temperature (BT) from infrared window channel (near $11 \mu\text{m}$ ). The green line on panel (f) shows the fractional coverage of cloud tops of $-60^\circ\text{C}$ or colder within $6^\circ \times 6^\circ$ square box around the pouch center. Cyan dashed lines indicate the box size that are used in our meso- $\alpha$ scale analysis. The black solid and white dotted lines denote the aircraft mission and genesis as in Fig. 2.5 . . . . .	23
2.7	Visible satellite image with flight track around 700 hPa level in green line and wind barbs denoting 1000 hPa winds measured by dropsondes deployed from the flight mission. The center of the wave pouch ( $18.4^\circ\text{N } 151^\circ\text{E}$ ) is indicated by a red star. Red box denotes the radar analysis domain in Fig. 2.8a . . . . .	25

2.8 Radar reflectivity (shading, dBZ) and vertical vorticity (contours, $1 \times 10^{-3} \text{ s}^{-1}$ with zero omitted and negatives denoted by dashed lines) at 2 km in the zoomed-in domain of the convective area inside the wave pouch of pre-depression Hagupit around 00 UTC September 14. <b>a</b> ) radar observation composited for 0058–0114 UTC inside the 120 km x 80 km domain (red box in Fig. 2.7). Yellow boxes in panel (a) are zoomed in for more detail: N box in the time periods of <b>b</b> ) 0030–0037 UTC, <b>c</b> ) 0037–0043 UTC, and S box in the time periods of <b>d</b> ) 0121–0128 UTC, <b>e</b> ) 0128–0135 UTC. . . . .	26
2.9 Meso-gamma scale evolution of N cell from (left panels, (a)-(e)) 0030–0037 UTC flight to (right panels, (f)-(j)) 0037–0043 UTC flight. <b>a), f)</b> radar reflectivity (shading), stretching (contours), and horizontal wind velocity (vectors) at 2 km within the 7 minutes time interval. <b>b), g)</b> same shading as (a) and (f) but tilting at 2 km as contours. <b>c), h)</b> convergence (shading) and vertical vorticity (contours) at 2 km. <b>d), i)</b> horizontal vorticity magnitude and direction (shading and vectors) and vertical velocity (contours) at 2 km. <b>e), j)</b> radar reflectivity (shading), vertical velocity (contours), and horizontal velocity (vectors) at 7 km. For all contours, zeros are omitted and negative values are denoted with dashed lines. . . . .	28
2.10 Meso-gamma scale evolution of S cell from (left panels, (a)-(e)) 0121–0128 UTC flight to (right panels, (f)-(j)) 0128–0135 UTC flight. The panels are the same as in Fig. 2.9. .	29
2.11 Meso-gamma scale evolution of N cell from (left panels, (a)-(e)) 0030–0037 UTC flight to (right panels, (f)-(j)) 0037–0043 UTC flight. <b>a), f)</b> radar reflectivity (shading), stretching (contours), and horizontal wind velocity (vectors) at 2 km within the 7 minutes time interval. <b>b), g)</b> same shading as (a) and (f) but tilting at 2 km as contours. <b>c), h)</b> convergence (shading) and vertical vorticity (contours) at 2 km. <b>d), i)</b> horizontal vorticity magnitude and direction (shading and vectors) and vertical velocity (contours) at 2 km. <b>e), j)</b> radar reflectivity (shading), vertical velocity (contours), and horizontal velocity (vectors) at 7 km. For all contours, zeros are omitted and negative values are denoted with dashed lines. . . . .	31
2.12 Meso-gamma scale evolution of S cell from (left panels, (a)-(e)) 0121–0128 UTC flight to (right panels, (f)-(j)) 0128–0135 UTC flight. The panels are the same as in Fig. 2.11. .	32
2.13 Meso- $\alpha$ scale structure of pre-depression Hagupit at 0000 UTC 14 September. <b>a)</b> radar reflectivity at 2 km (shading) with wave-relative streamlines at 1 km (black) and wind vectors at 10 km (blue). Orange and green boxes are 120 km x 120 km encompassing regions of primarily convective and stratiform precipitation in the pouch, respectively. The dotted lines indicate nine ensemble boxes shifted for (-10, 0, 10 km) in x- and y-direction. <b>b-c)</b> circulation and stretching tendency with height, respectively. Orange and green lines are averaged over the nine dotted orange and green boxes in panel (a). .	35

2.14 Schematic of the multi-scale interactions in Hagupit's cyclogenesis. <b>a)</b> Synoptic scale active features are the upper-level trough and easterly wave which carries the marsupial wave pouch, denoted as red circulation. <b>b)</b> In the meso- $\alpha$ scale wave pouch, the low-level cyclonic streamlines are shown with circulation center marked with black cross and mid-level center as yellow cross. Overlain on the clouds to the southwest of the low-level center is vorticity (positive: red, negative: blue), illustrating vorticity dipoles from tilting, enhanced vorticity from stretching, and a mid-level MCV over the stratiform area. <b>c)</b> In the meso- $\beta$ scale, the local wind shear profile that influences the convective organization is composed of winds from cyclonic circulation inside pouch, easterly wave propagation, and the trough. <b>d)</b> Meso- $\gamma$ scale convective cells produce vorticity that serve as building blocks for the wave pouch intensification through tilting of horizontal vorticity associated with low-level wind shear (S cell) and stretching of the local vertical vorticity (N cell). See text for description of each physical process... . . . . .	37
3.1 Vertical profiles of <b>(a)</b> environmental zonal wind for SH5, SH7.5 and SH10 experiments <b>(b)</b> water vapor mixing ratio for outer-core region ( $> 300$ km radius) for Moist100, Moist50, Moist 25; <b>(c)</b> Water vapor mixing ratio at the surface level from one of the Moist50 experiments. . . . .	46
3.2 Cross-section of the tangential wind profiles for the sensitivity experiments from <b>(a)</b> REF, <b>(b)</b> Weak, and <b>(c)</b> Midlevel experiments. . . . .	47
3.3 Timeseries of hourly minimum sea level pressure for 20 ensemble members of 9 experimental sets from the Main Set. Timings of tropical cyclogenesis and rapid intensification onset are marked with black circles and red crosses, respectively. . . . .	48
3.4 Time series of hourly saturation fraction for all 20 ensemble members of 9 experimental sets from the Main Set. Saturation fraction is the innermost domain averaged (720 x 720 km) for the vertical layer of 0-6 km. Both the dotted vertical line and the line color indicate the timings of tropical cyclogenesis of each ensemble member. . . . .	51
3.5 Time series of precursor events for <b>(a)</b> slowest developing ensemble member and <b>(b)</b> fastest developing ensemble member of SH7.5_Moist50 experimental sets. Grey dashed lines in <b>(a)</b> indicates the timesteps highlighted in Figs. 3.6 and 3.7 . . . . .	52
3.6 Snapshot of simulated TC from the slowest developing member of SH7.5_Moist50 at hour-75 (Fig.3.5a). Pressure anomaly and the streamlines at altitude of <b>(a)</b> 6 km, <b>(c)</b> 1 km, simulated reflectivity at 6km inside 200 x 200 km box around the center of <b>(b)</b> mid-level vortex center, <b>(d)</b> low-level vortex center. Red and white 'x' indicate the vortex center at 1 km and 6 km altitude, respectively. The 200 x 2000 km red and white boxes in <b>(a)</b> , <b>(c)</b> are centered on the vortex center at 1 km and 6 km. The white box is zoomed in as the domain of panel <b>(b)</b> , and the red box corresponds to the domain of panel <b>(d)</b> . . . . .	55
3.7 Snapshot of simulated TC from the slowest developing member of SH7.5_Moist50 at hour-150 (Fig.3.5 a). Panel information is the same as Fig. 3.6. . . . .	56
3.8 Low-level convective coverage as a function of minimum sea level pressure decrease with color denoting the simulation time for SH7.5 simulations. Low-level convective coverage threshold is 14%, which is an average value of low-level convective coverage for all developing members in the Main Set. . . . .	58

3.9	Histograms of the number of TC genesis precursor events occurring before the timing of genesis. Histograms of <b>(a)</b> , <b>(c)</b> , <b>(g)</b> , and <b>(e)</b> are composed by shear magnitude. Histograms of <b>(b)</b> , <b>(d)</b> , <b>(f)</b> , and <b>(h)</b> are for SH7.5 simulations only, and composed by environmental moisture magnitude. . . . .	60
3.10	Timing of the TC genesis precursor events compared to timing of genesis. Each event is counted with the precursor parameter keeping its value below or beyond the threshold for 3 hours continuously. . . . .	62
3.11	Time-lagged Pearson correlations between time series of minimum sea level pressure (SLP) and <b>(a)</b> vortex tilt, <b>(b)</b> mid-level vorticity, <b>(c)</b> low-level convective coverage, <b>(d)</b> mid-level convective coverage for the SH7.5_Moist50 experimental set. Red dotted vertical lines indicate the time-lag of maximum/minimum correlation for each ensemble member, and red solid lines indicate the mean time-lag for the ensembles with genesis timing $\leq$ 168-hour. Positive time-lag means each precursor event happens before SLP drops and vice versa. . . . .	64
3.12	Time-lag Pearson correlation between time series of minimum sea level pressure (SLP) and mid-level convective coverage as a function of time-lag for the whole main set experiments. Annotation is the same as Fig. 3.11. . . . .	65
3.13	Time-lag correlation analysis results for the time series of minimum sea level pressure (MSLP) and each of the four precursor variables with mean of time-lag for y-axis and standard deviation of the time-lag of 20 ensemble members in x-axis. The size of the circle is proportional to the mean correlation between two time series at the time-lag. The combination that had correlation not significant at 95% level is marked with ‘x’ rather than a circle. The ensemble sets that do not have any developing members are not shown. . . . .	67
3.14	Time series of minimum sea level pressure deepening for 20 ensemble members of sensitivity simulations of <b>(a)</b> REF, <b>(b)</b> Midlevel, <b>(c)</b> Weak. REF is the same as SH7.5_Moist50 except that it’s run by WRF3.9 instead of WRF3.1.1. Midlevel is the same as REF except that the initial vortex is centered at 600-hPa instead of 850-hPa. Weak set is the same as SH5_Moist100 but its initial vortex has maximum wind speed of $12.5 \text{ m s}^{-1}$ instead of $15 \text{ m s}^{-1}$ and it is run by WRF3.9 instead of WRF3.1.1. . . . .	69
3.15	Time series of precursor events for <b>(a)</b> slowest developing ensemble member and <b>(b)</b> fastest developing ensemble member of the Midlevel sensitivity experimental set. . . . .	70
3.16	Time series of precursor events for <b>(a)</b> slowest developing ensemble member and <b>(b)</b> fastest developing ensemble member of the Weak sensitivity experimental set. . . . .	70
3.17	Histograms of the number of TC genesis precursor events occurring before the timing of genesis for the sensitivity test sets. . . . .	71
3.18	A pyramid diagram of tropical cyclogenesis in moderately sheared and dry environments	72
4.1	TERRA MODIS Infrared image of Supertyphoon Jebi (2018) at 12:20 UTC 31st August. The brightness temperature is in Fahrenheit. The elongated rainband in the southwestern quadrant (i.e., “monsoon tail” rainband) is highlighted with a yellow circle. Modified image courtesy of the US Naval Research Laboratory (NRL). . . . .	77

4.2	Daily Gridsat-B1 infrared brightness temperature over the western North Pacific from 01/09/2018 to 04/09/2018. Typhoon Jebi is marked with a ‘J’ and the research vessel (R/V) Thompson’s location is marked with an ‘S’. The area marked with an ‘I’ is an area of widespread convection, which was monitored as an Invest for potential tropical cyclogenesis by the Joint Typhoon Warning Center. . . . .	78
4.3	A diagram of the methodology used to calculate infrared brightness temperature (BT) and environmental variables from ERA5 in our TC-centered analysis. BT data are taken as an annulus with $1^{\circ}$ width, and ERA5 data are calculated using a square box. For example, for an analysis at $4^{\circ}$ radius, BT grid points inside the yellow area are used, and ERA5 grid points spanning an $8^{\circ} \times 8^{\circ}$ box are used. . . . .	83
4.4	2-D histogram of infrared brightness temperature anomalies from the radial mean of the annulus around the tropical cyclone (TC) center for 0–30 $^{\circ}$ N, 100–150 $^{\circ}$ E for June–September 1980–2019 for the (a) northwestern, (b) northeastern, (c) southwestern, (d) southeastern quadrant of the TC. . . . .	85
4.5	As in Fig. 4.4 but for deep convection coverage anomalies. . . . .	86
4.6	Pearson correlation between southwestern quadrant brightness temperature (“monsoon tail” proxy) and environmental/tropical cyclone (TC) variables as a function of radius from the TC center. Environmental variables are in red and TC variables are in black. . . . .	88
4.7	40-year summertime (June–September) climatology of (a) divergence and winds at 200 hPa, (b) relative vorticity and winds at 850 hPa, (c) relative humidity at 850 hPa and deep-layer (200–850 hPa) vertical wind shear over the western North Pacific. . . . .	90
4.8	Time series of the normalized (a) ENSO Longitude Index (ELI) and the (b) Western North Pacific (WNP) monsoon index averaged for JJAS from 1980–2019. Normalized index values exceeding $\pm 1$ standard deviation are denoted with red (positive) and blue (negative) circles. Orange lines indicate the normalized JJAS mean “monsoon tail” rainband anomaly over the WNP. For more details, refer to section 4.3.2. . . . .	92
4.9	Zonal and meridional deep-layer (200–850 hPa) vertical wind shear composited for the seasons that have anomalous (greater than $\pm 1$ standard deviation) ENSO longitude index values (a, b, c, d) and western North Pacific monsoon index values (e, f, g, h). . . . .	93
4.10	Boxplots of mean brightness for a radius range from $4$ – $10^{\circ}$ composed by TC quadrants and (a) the ENSO longitude index (ELI) or (b) the western North Pacific (WNP) monsoon index . . . . .	95
4.11	Okubo-Weiss parameter and streamlines at 850 hPa for 12-hourly observations from 01/09/2018 12 UTC to 05/09/2018 00 UTC. A ‘J’ marks the location of Super Typhoon Jebi, and an ‘I’ indicates the broad convective area tracked as Invest 98W (Fig. 4.2). The red $5^{\circ} \times 5^{\circ}$ square in (b) marks the cross-section area in Fig. 4.13. . . . .	96
4.12	Okubo-Weiss parameter and streamlines at 850 hPa for 12-hourly observations from 04/09/2019 12 UTC to 08/09/2019 00 UTC. An ‘L’ marks the location of Typhoon Lingling, and a ‘T’ marks the location of TD19 that emerged from the monsoon tail rainband of Lingling. The red $5^{\circ} \times 5^{\circ}$ square in (d) marks the cross-section area in Fig. 4.13. . . . .	97



# Chapter 1

## Introduction

### 1.1 Motivation

Many researchers have studied tropical cyclone (TC) formation since the early 1900s (e.g. Weightman 1919). One of the reasons that this topic has intrigued numerous researchers is that a tropical cyclone (TC), once developed, can cause enormous damage to society through torrential rain, storm surge, and wind gusts. Another reason is that tropical cyclogenesis is a complex multi-scale process so that many questions on tropical cyclogenesis still remain unanswered after many decades of research.

One of the most important puzzles in our knowledge of tropical cyclogenesis lies in the interaction between a TC and the environment surrounding it. Individual clouds in a TC have stochastic turbulent characteristics. On the other hand, TCs are under the influence of large-scale environments that can be regarded as quasi-balanced flows (Fig. 1.1). Then, to what extent a TC is determined by the environment and to what extent by the stochastic turbulence?

An increasing number of studies have recently investigated tropical cyclogenesis in sheared environments. Deep-layer vertical wind shear (VWS) is defined as the difference between the upper-atmospheric (200-hPa) and lower-atmospheric (850-hPa) wind fields. The presence of moderate VWS ( $4.5\text{--}11 \text{ m s}^{-1}$ ) makes TC intensity prediction most uncertain (Rios-Berrios and Torn 2017). Some TCs decay in the sheared environment due to dry-air intrusion and vortex misalignment, but a fair number of TCs withstand it and even intensify under the same magnitude of shear (Nolan and McGauley 2012; Tao and Zhang 2015). We do not fully understand how vertical wind shear influences the incipient TCs, especially in context of mid-level moisture and interaction of the shear with the parent synoptic scale precursor.

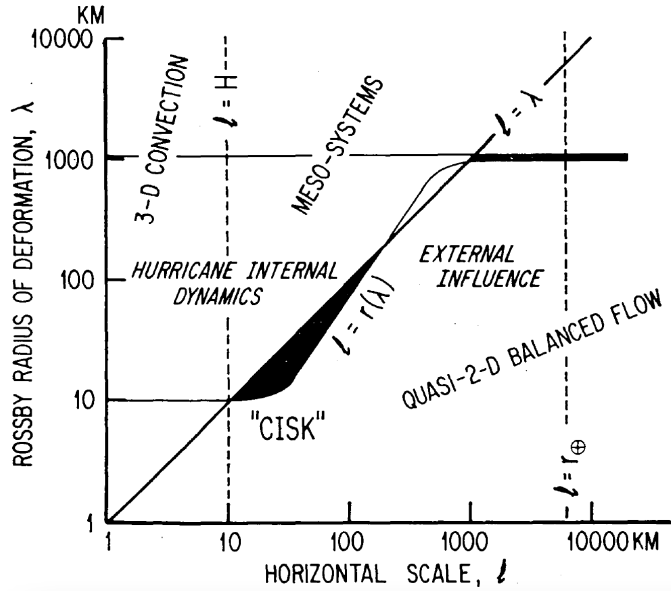


**Figure 1.1:** Scale-dependence of tropical cyclone dynamics adapted from Ooyama (1982). Darkened area implies the existence of cloud-organizing mesoscales within the deterministic regime of the balanced flow.

This doctoral study scrutinizes the factors that increase uncertainty regarding the multi-scale tropical cyclogenesis problem, namely, vertical wind shear (VWS), environmental humidity, and precursor vortex structure.

## 1.2 Literature Review

A developing vortex is designated as a tropical storm by operational forecast centers when its sustained winds are regarded as exceeding  $17 \text{ m s}^{-1}$ . However, it is somewhat artificial to pinpoint the exact timing of cyclogenesis. In reality, tropical cyclogenesis is a continuous, multiscale process.

In this section, the theories on tropical cyclogenesis – the precursors and mechanisms, are reviewed: warm ocean, types of synoptic cyclonic disturbances, low to moderate VWS, deep organized convection in the moist deep wave pouch, and with the associated dynamic and thermodynamic interactions. Over the past century, researchers have made a huge progress in our understanding of tropical cyclogenesis, but as highlighted throughout this section, many questions still remain open.

### **1.2.1 Large scale: thermodynamic conditions for tropical cyclogenesis**

Gray (1979) found the large-scale thermodynamic conditions for tropical cyclogenesis to be the presence of conditional instability through a deep layer in association with a moist atmosphere and a well-mixed, warm oceanic layer. The warm ocean is the source of energy for TCs. TCs extract sensible and latent heat energy from the ocean and export that energy in the upper troposphere through convection. In this regard, TCs differ from extratropical cyclones, which extract energy from horizontal temperature gradients in the atmosphere.

A sea surface temperature (SST) greater than 26°C has been generally regarded as the threshold for tropical cyclogenesis (e.g. Palmen 1948; Gray 1968). Though there exist several formation cases over cooler water, according to a climatological study of all TCs 1981 – 2010 (Dare and McBride 2011), nearly 98% formed over SSTs greater than 25.5°C. One thing to note is that TCs interact with the upper layer of the ocean, not just with the sea surface skin. Several recent studies have argued that TC forecast models should use the upper ocean heat content as a parameter, instead of SST to improve accuracy (Goni et al. 2009; Lin et al. 2013).

Environmental moisture is also an important environmental condition for tropical cyclogenesis. Peng et al. (2012) compared developing and nondeveloping disturbances over the North Atlantic and suggested that the vertically integrated moisture, rain rate, 750-hPa relative humidity (RH), and divergence are the most important factors in determining whether or not a tropical disturbance will develop into a tropical storm. They also found that prior to rapid development into a tropical storm, developing disturbances may not possess stronger vorticity than their nondeveloping counterparts. Comparing the developing wave pouch (pre-Karl) and nondeveloping wave pouch (ex-Gaston), Montgomery et al. (2012) and Davis and Ahijevych (2013) revealed that a key difference between developing and nondeveloping disturbances is the mid-level humidity.

### **1.2.2 Synoptic scale: pre-existing disturbance**

Tropical cyclogenesis might occur in the absence of a precursor disturbance through spontaneous aggregation with sufficiently high SST (e.g. Wing et al. 2016). However, it took more than

14 days for a TC to develop without any pre-existing disturbance in numerical simulations (Nolan et al. 2007). Also, Davis (2015) showed that the genesis process begins only after a dominant vortex self-organizes through the positive feedback between convection and circulation. Dunkerton et al. (2009) argued that “spontaneous aggregation cranking up the underlying ocean heat is likely nature’s last resort in the real world”.

In the real atmosphere, tropical cyclogenesis is associated with pre-existing synoptic-scale disturbances. They provide enhanced low-level absolute vorticity to the pre-genesis vortex. There exist multiple different synoptic flow regimes that favor TC formation. They can be broadly classified as: (1) a tropical-wave pathway (e.g. tropical easterly waves, Rossby waves, and Kelvin waves), (2) a geophysical turbulence pathway (e.g. monsoon troughs and Madden Julian Oscillation), (3) extratropical influence pathway (e.g. tropical transition of extratropical trough) and (4) topographic flow pathway (Ritchie and Holland 1999; Dunkerton et al. 2009; McTaggart-Cowan et al. 2013). This pathway classification is not rigid though because multiple pathways can act together for one genesis case.

### **1.2.3 Mesoscale: tropical cyclogenesis paradigms**

Although TCs develop in different synoptic environments, as Gray (1968) noted, “the basic physical processes which accompany the development of these warm-core cyclones must be very similar”. In other words, tropical cyclogenesis is hypothesized to follow the same mesoscale evolution universally regardless of environmental background. However, there remains a debate on the precise mechanisms and importance of various factors and processes.

Many studies (sometimes referred to as ‘top-down theory’) emphasize the importance of a mid-level vortex in the stratiform precipitation region. Bister and Emanuel (1997) proposed that the low-level cyclonic circulation is built downward from the mid-level vortex, which forms in response to vertical gradient of diabatic heating in the stratiform precipitation region. More recent studies further emphasized the role of a mid-level vortex in moistening and stabilizing the thermodynamic profile (Raymond and Sessions 2007; Davis and Ahijevych 2013). They argue that the

mid-level vortex and stratiform precipitation lead to the vertical mass flux profile becoming more bottom-heavy, and favorable for further convection.

Another group of studies (sometimes referred to as 'bottom-up theory') argue for the primacy of low-level convective processes that precede mid-level stratiform processes. Wang (2012) showed in numerical simulations that the low-level meso-beta scale vortex appears first, then meso-alpha scale mid-level vortex follows, and finally the surface meso-alpha scale vortex develops in that order. The bottom-up theory suggests that vortical hot towers (VHTs), or rotating cumulonimbus clouds, are the building blocks for tropical cyclogenesis. A VHT acts as a heat source for a TC proto-vortex and it generates vorticity through stretching. Although the lifetime of VHT convection is of the order of one-hour, vorticity anomalies generated by deep convection last much longer (Wissmeier and Smith 2011a).

Recent studies suggest that both deep convective heating and stratiform heating are important in TC genesis, with deep convection and stratiform precipitation contributing to the low-level and mid-level spinup of the TC vortex, respectively. Bell and Montgomery (2019) showed that the stratiform precipitation can play a supporting role of conditioning the environment for deep convection by increasing the relative humidity and lowering the level of free convection.

#### **1.2.4 The meeting point of multi-scale processes: wave pouch theory**

As a meeting point of downscale processes and upscale processes, Dunkerton et al. (2009) proposed the "wave pouch theory". The basis of the pouch theory is that tropical depression formation is greatly favored in the critical-layer region of the synoptic-scale predepression wave or subtropical disturbance. It describes how a hybrid wave-vortex structure becomes a tropical depression. In the approximately closed circulation of the pouch, an upscale vorticity aggregation process is protected from strain/shear deformation. This conceptual model is labeled as the marsupial paradigm, as the cyclogenesis sequence is likened to the development of a marsupial infant in its mother's pouch (Montgomery et al. 2012). The formation of the wave pouch has been suggested as a necessary condition for wave to tropical cyclone transition throughout the series of papers by Dunkerton, Montgomery, Wang and co-authors.

Figure 1.2 shows the formation of a tropical storm within a wave pouch. The dashed contours represent the streamlines of the marsupial wave in the ground-based frame of reference, which usually has an inverted-V pattern. However, when it comes to the wave-relative Lagrangian frame (moving at the same speed with the wave), the streamlines show a quasi-closed circulation, which is indicated as solid streamlines. The closed circulation inside the pouch can protect the mesoscale vortices from the hostile environment, such as the dry Saharan air layer (SAL in Fig. 1.2). The intersection of the critical latitude (CL) and the trough axis pinpoints the pouch center as the preferred location for tropical cyclogenesis (Wang et al. 2010; Wang 2012).

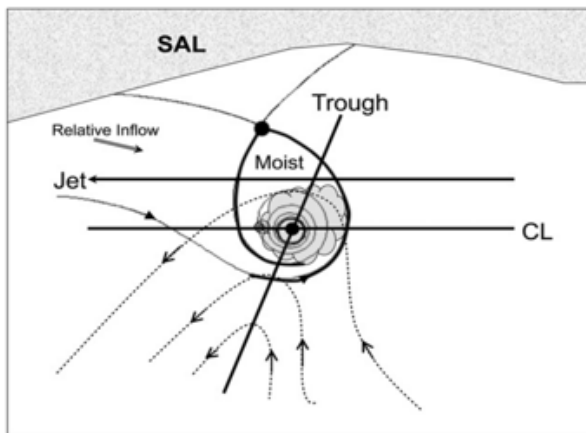


**Figure 1.2:** Conceptual diagram of how tropical storm forms in a wave pouch (adapted from Fig. 3 of Wang et al. (2010))

### 1.2.5 The deal breaker: vertical wind shear

Many prior studies have considered TC formation in quiescent environments with no mean wind flow and no wind shear (so-called, “hurricane in a box”). With this set-up, numerical models show that every initial disturbance develops into a TC, shortly followed by a rapid intensification (Montgomery et al. 2006; Zhang and Tao 2013). However, in reality, only about 20% of tropical disturbances develop into tropical cyclones (Dunkerton et al. 2009). When moderate VWS is applied, genesis from the precursor vortex can be delayed, and for stronger VWS, genesis can be suppressed completely (Nolan and McGauley 2012).

This negative impact of VWS on tropical cyclogenesis has been recognized since the early 1940s. Riehl and Shafer (1944) reported a vertical wind profile with easterlies at the surface and westerlies at 14,000 ft “prevented development of strong rotating vortices” in the North Atlantic based on analysis of balloon-based wind charts. From composite satellite observations, Gray (1968) showed TC development occurred the most where 200-850hPa VWS was a minimum or zero. DeMaria and Kaplan (1994) found, from their statistical model for TC intensity prediction, 200-850 hPa VWS was the most important predictor having a negative regression coefficient.

It is true that the chances of tropical cyclogenesis decrease with increasing VWS magnitude, but recent studies have reported that small to intermediate magnitude of shear ( $2.5\text{-}5 \text{ m s}^{-1}$ ) can be actually more favorable for TC formation compared to zero shear (Bracken and Bosart 2000; Nolan and McGauley 2012).

We do not fully understand why most TCs weaken in the presence of VWS, but several physical mechanisms have been suggested, including vortex tilt, precipitation asymmetry, and ventilation. First, vortex tilt tears down the vertical structure of TCs by increasing stability above the low-level center, and it induces eddy fluxes of low momentum and low entropy in the vortex core (Jones 1995). Second, precipitation asymmetry is detrimental to TC formation by displacing the location of diabatic heating from the center of circulation. Diabatic heating is the most effective for TC intensification when it occurs near the vortex center (Pendergrass and Willoughby 2009; Vigh and Schubert 2009). Third, ventilation means intrusion of cool and dry air, which dilutes convection and thus limits diabatic heating (Tang and Emanuel 2012).

We have even fewer answers to the question of how some TCs form/intensify in spite of shear. Recently, researchers have begun to examine this problem. In terms of vortex tilt, Jones (1995) introduced the concept of “vortex precession”, which is the advection of one vortex by the winds of the other vortex. Through vortex precession, mid-level and low-level vortices can be re-aligned (e.g. Reasor et al. 2004a; Reasor and Montgomery 2015). Molinari et al. (2006) and Nguyen and Molinari (2015) proposed another mechanism called “downshear reformation.” When there is a mid-level vortex in sheared environment, an updraft is caused downshear by thermal wind balance.

Downshear reformation is a phenomenon in which the center of the TC reforms downshear side, underneath the intense convection through diabatic heating. Rios-Berrios et al. (2018) hypothesized that genesis in sheared environments was due to downshear reformation in combination with a vortex merger process (Van Sang et al. 2008).

Despite these recent advances, the complexities of tilt, ventilation, precession, and reformation are not fully understood and the precise role of the shear in suppressing or organizing convection within the incipient TC remains to be clarified.

### 1.3 Dissertation Objectives and Outline

This dissertation presents a sequence of three research projects that investigate convective organization and tropical cyclogenesis in sheared environments. The objective of the dissertation is to identify and understand key multi-scale precursors leading to tropical cyclone genesis in the marginally favorable, sheared environments, so that we can assess the sources of increased uncertainty of TC genesis in such environments.

**Chapter 2** is a detailed observational case study of Typhoon Hagupit (2008) that survived through strong VWS and eventually developed into a typhoon. A multi-scale analysis was conducted using high temporal and spatial resolution dual-Doppler radar and dropsonde data from aircraft observations along with satellite and reanalysis data. The strong deep-layer VWS ( $> 20 \text{ m s}^{-1}$ ) had a negative impact on the development of pre-depression Hagupit through misalignment of the low and mid-level circulations and dry air intrusion. However, the low-level circulation persisted and the system ultimately formed into a tropical cyclone after it had left the high-shear zone. Here we propose that a key process that enabled the pre-depression to survive through the upper-tropospheric trough interaction was persistent vorticity amplification on the meso- $\gamma$  scale that was aggregated on the meso- $\alpha$  scale within the wave pouch. Multi-Doppler wind analysis indicates that cumulus congestus tilted the low-level horizontal vorticity into the vertical in the early stage of the convective life-cycle, followed by stretching from maturing deep convection. Variations in low-level VWS on the meso- $\beta$  scale affect convective organization and horizontal vorticity gener-

ation. The results of this study provide new insights into multi-scale processes during TC genesis and the interactions of a pre-depression with VWS at various spatial scales.

**Chapter 3** is a large ensemble numerical modeling study for TC genesis in moderately sheared and dry environments. A number of idealized TC simulation sets with 20-member ensembles with varying VWS magnitude and environmental humidity are used, with sensitivity tests for different types of initial vortex (mid-level centered and weaker vortex). In this study, we investigate which processes may lead to bifurcation points between the TCs that do develop and the ones that are suppressed under the same magnitude of VWS. A key finding is that there are repetitive cycles of precursor events lining up together before tropical cyclogenesis, and slow or non-developing ensemble members of the marginal environments go through a number of the cycles of precursor events that are very close to successful ones. The complete cycle of precursor events is as follows. In time order, 1) increased deep convective coverage over the broader circulation, 2) mid-level vortex reformation, 3) sustained vortex reformation, 4) convection organized near the low-level center, and finally 5) tropical cyclogenesis. We show the probability distribution of the ensemble members for each precursor event, and identify which process among the above five processes is the bifurcation point between developing and non-developing ensemble members depending on the environmental setup. The results of this study improves our knowledge on why the combination of moderate VWS and environmental dry air makes an unstable and uncertain setup for TC genesis.

**Chapter 4** outlines climatological and case studies of the "monsoon tail" rainband—an elongated strong rainband in the southwestern quadrant of TCs over the monsoonal area of the western North Pacific (WNP). The monsoon tail rainband was observed for the majority of TCs during the Propagation of Intra-Seasonal Tropical OscillationNs (PISTON) field campaign (2018–2019). The monsoon tail rainband showed potential as a route of subsequent tropical cyclogenesis; the monsoon tail rainband of Typhoon Jebi (2018) and Typhoon Lingling (2019) sustained convective organization even after it separated from the pre-existing TC, and became Invest 98W and TD 19 afterwards. The results of this study show that the monsoon tail rainband is a common feature of TCs in the WNP monsoonal area, and its presence and longevity are a result of TCs interacting

with both the low-level and upper-level flow. Despite the demonstrated convective enhancement, the environment around the separated monsoon tail rainband is not generally found to be favorable for subsequent genesis due to enhanced VWS.

**Chapter 5** synthesizes the dissertation's findings about tropical cyclogenesis in sheared environments, and provides concluding remarks and implications for future work.

# Chapter 2

## Multi-scale shear impacts during the genesis of Hagupit (2008)<sup>1</sup>

### 2.1 Introduction

Many researchers have studied tropical cyclone formation (i.e., tropical cyclogenesis) since the early 1900s (e.g. Weightman 1919). Over one century, researchers have made a huge progress in our knowledge of tropical cyclogenesis but many research questions still remain unanswered due to the complexity of the multi-scale processes involved. The multiple spatio-temporal scales of dynamic and thermodynamic processes involved in tropical cyclogenesis range from large scale ocean environments and background flows to convective scale processes. One of the challenges to investigate these multi-scale interactions is that high resolution observations in a pre-genesis storm are scarce. During the Tropical Cyclone Structure 2008 (TCS08) and THORPEX Pacific Area Regional Campaign (T-PARC) field experiments (Elsberry and Harr 2008), a complex interaction between convection and background wind flow within the pre-depression Hagupit (2008) was observed by research aircraft at high temporal and spatial resolution.

Pre-depression Hagupit (2008) developed from an easterly wave propagating along 18 N latitude. Hagupit could be first identified with active convective bursts in satellite imagery on 8 September and with total precipitable water in GFS analysis that was 10–20 mm higher than in the surrounding region around 00 UTC 9 September (Bell and Montgomery 2010). Then, it was 10 days later at 0000 UTC 19th September 2008 that the pre-depression was designated as a tropical depression (TD) by the Joint Typhoon Warning Center (JTWC). On average, it takes 3.2 days for a pre-depression to develop from the convective stage to the TD designation according to Zehr

---

<sup>1</sup>The results outlined in Chapter 2 have been published in the *Monthly Weather Review*: Nam, C. C., and M. M. Bell, 2021: Multiscale shear impacts during the genesis of hagupit (2008). *Monthly Weather Review*, **149** (2), 551 – 569, doi: 10.1175/MWR-D-20-0133.1. ©American Meteorological Society. Used and adapted with permission.

(1992). The delay of pre-depression Hagupit's development was due in part to its interaction with an upper-level trough during 13–14 September.

In Hagupit's case, the influence from the upper-tropospheric trough was largely unfavorable for TC genesis, but an upper-tropospheric trough can be a favorable ingredient for TC genesis. In the tropical transition paradigm, the upper-tropospheric potential vorticity can be vertically redistributed toward the developing surface vortex through deep convection (Davis and Bosart 2003; Chang et al. 2019). McTaggart-Cowan et al. (2013) showed about 20 % of TC genesis in the West Northern Pacific is trough-induced or via tropical transition, and a favorable interaction occurs when the VWS from the upper-tropospheric trough is relatively small and the sea surface temperatures are warm. Similarly, Fischer et al. (2019) found that the upper-tropospheric troughs that are associated with TC rapid intensification (RI) have smaller zonal wave length and induce smaller VWS over the TC (mostly below  $10 \text{ m s}^{-1}$ ) compared to the majority of upper-tropospheric troughs associated with non-RI episodes.

The upper-tropospheric trough that Hagupit interacted with induced strong VWS over the pre-depression. Strong VWS ( $> 10 \text{ m s}^{-1}$ ) is known to delay or suppress the genesis completely (Tao and Zhang 2014a). Several physical mechanisms have been suggested to explain why most TCs weaken in the presence of VWS, including vortex misalignment (Jones 1995), precipitation displacement (Pendergrass and Willoughby 2009; Vigh and Schubert 2009), and ventilation (Tang and Emanuel 2010, 2012). VWS is not always a negative factor for TC genesis though. Recent studies have shown that small to intermediate magnitudes of shear ( $2.5\text{--}5 \text{ m s}^{-1}$ ) can be actually more favorable for TC formation compared to zero shear (e.g. Nolan and McGauley 2012). We do not fully understand how VWS influences incipient TCs, especially in the context of the interaction with mid-level dry air and the parent synoptic scale precursor (Aiyyer et al. 2014). The presence of moderate VWS ( $4.5\text{--}11 \text{ m s}^{-1}$ ) in particular increases uncertainty in tropical cyclone (TC) intensity prediction (Rios-Berrios and Torn 2017). The uncertainty arises because many TCs decay in the sheared environment, but a fair amount of TCs withstand the shear impact and even intensify under the same magnitude of VWS.

Hagupit survived the impacts of strong VWS in its early developing phase then ultimately intensified into a TC. Fewer mechanisms have been suggested to explain why some TCs form and intensify in the presence of VWS. In terms of vortex misalignment, Jones (1995) introduced the concept of “vortex precession”, which is the advection of one vertical layer of a vortex by the winds of another layer. Through vortex precession, mid-level and low-level vortices can be re-aligned (e.g. Reasor et al. 2004a; Reasor and Montgomery 2015). Molinari et al. (2006) and Nguyen and Molinari (2015) proposed a thermodynamic mechanism that they called “downshear reformation”, where the center of the TC reforms underneath the intense convection stimulated downshear by the interaction between VWS and the mid-level vortex (Raymond and Jiang 1990). Chen et al. (2018) examined downshear reformation in detail with a case study of typhoon Vicente (2012), and highlighted the role of convective bursts inside the downshear precipitation area in initiating the reformation process through tilting and upward vorticity advection. Rios-Berrios et al. (2018) extended the downshear reformation hypothesis by combining it with the vortex merger paradigm of Van Sang et al. (2008), arguing that the vortex realignment process is not through advective procession but through vortex merger process. The “re-structuring” process proposed by Rios-Berrios et al. (2018) starts with the asymmetric precipitation due to VWS then progressively symmetrizes via vortex merger, which reduces vortex misalignment.

All the aforementioned mechanisms that explain how some TCs withstand VWS require a well-defined mid-level vortex. Although the role of a mid-level vortex is dynamically and thermodynamically essential for TC development (Raymond and Sessions 2014; Bell and Montgomery 2019), for certain period, a pre-depression may only have a low-level closed circulation (LCC) and not have a mid-level vortex (Reed and Recker 1971). The numerical simulations of tropical cyclogenesis from Wang (2012) showed that the low-level meso- $\beta$  scale vortex appears first, then mid-level meso- $\alpha$  scale vortex follows, and finally the surface meso- $\alpha$  scale vortex develops. In contrast, some pre-depression systems that originate from African easterly waves or extratropical disturbances may have a mid-level vortex but no well-developed LLC (Davis and Bosart 2003; Chang et al. 2019; Pytharoulis and Thorncroft 1999).

In this study, we examine the factors that allow a pre-depression to survive in a sheared environment with a mid-level vortex that was severely displaced ( $> 500$  km) from the LLC with a case study of Hagupit. We focus on two key factors that enable a pre-depression to withstand the detrimental effects of environmental shear, namely the wave pouch and localized low-level VWS. First, the Lagrangian closed circulation colloquially called the 'wave pouch' can protect the incipient pre-depression from dry air intrusion (Dunkerton et al. 2009). Keeping moist air in the recirculating wave pouch sustains deep convection due to reduced entrainment and reduced convective downdrafts (Bell and Montgomery 2019). Second, strong mid- or low-level shear can actually promote the organization of tropical deep convection (LeMone et al. 1998; Johnson et al. 2005). In this study we consider the combined impact of these two factors, and how VWS and wave pouch interactions play an important role in cyclogenesis. In particular, we take a novel approach to investigate these interactions across a range of scales from synoptic to meso- $\gamma$  scale using observational data.

From the two research flight missions over the pre-depression Hagupit on 14 and 15 September 2008, Bell and Montgomery (2010) provided an unprecedented look at the structure of deep meso-gamma scale convection under the influence of VWS. In this paper, building on Bell and Montgomery (2010), we will investigate what enabled the pre-depression to survive through the high shear and to eventually undergo cyclogenesis through analysis of these unique aircraft observations, along with large-scale satellite and reanalysis data. The rest of this chapter is outlined as follows. Section 2.2 introduces the datasets from TCS08/T-PARC and the analysis methodology used in this study. Section 2.3 describes the results from the multi-scale analysis of pre-depression Hagupit. Section 2.4 synthesizes the results and provides concluding remarks.

## 2.2 Data and Methods

For synoptic scale and meso- $\alpha$  scale analysis, we used a specialized  $0.25^\circ$  resolution Year of Tropical Convection (YOTC) reanalysis (August 2008 – July 2009, Rienecker et al. 2008) and the 3-hourly  $0.07^\circ$  resolution Grid Satellite (GridSat-B1) data (Knapp 2014). For meso- $\beta$  and meso- $\gamma$  scale analysis, we used measurements collected during the TCS08/T-PARC field campaigns: the

three-dimensional wind field and reflectivity from the high-resolution dual-Doppler radar observation from the Electra Doppler Radar (ELDORA) and soundings from low-altitude (3km) dropsondes deployed during the aircraft mission around 0000 UTC 14 September 2008. During this flight mission, multiple passes around a convective line between 0030 UTC and 0130 UTC captured the evolution of convective cells in detail.

A variational analysis package called SAMURAI (Bell et al. 2012; Foerster et al. 2014) was utilized in this study to synthesize the observations from radar and dropsondes with a prior estimate of atmospheric state. For the meso- $\alpha$  scale SAMURAI analysis, ELDORA Doppler velocity and reflectivity were integrated with dropsonde data at 5 km horizontal and 1 km vertical grid resolution using YOTC thermodynamic and dynamic fields at 0000 UTC 14 September as the prior state estimate. For the meso- $\beta$  and meso- $\gamma$  scale analyses, we synthesized ELDORA Doppler velocity and reflectivity at 500 m horizontal and vertical grid resolution without a prior estimate or dropsonde data. Gaussian filters with length scales of  $4\Delta x$  in the horizontal and  $2\Delta z$  in the vertical were used to reduce noise and focus on the scales of interest for each analysis.

To follow the movement of the wave pouch and examine its evolution, we tracked the center of the pouch, defined as the intersection of the critical latitude (where the zonal flow is equal to the wave phase speed) and the wave trough axis (where the meridional velocity is zero), using the YOTC wind field at 850 hPa following Wang et al. (2010). For the phase speed, we used  $-5 \text{ m s}^{-1}$ , the 3-hour average phase speed around 00 UTC 14 September identified from the flight mission, as the default value and tested with a range of phase speed from  $-2$  to  $-6 \text{ m s}^{-1}$  to accommodate daily variations in easterly wave translation speeds. When the intersection of the critical latitude and the wave trough axis matches with the center of the 850 hPa streamline circulation, we called it the phase speed value at that point in time.

We identify three kinds of vertical wind shear in terms of vertical layers: deep-layer (200–850 hPa), mid-level (500–800 hPa), and low-level (800–1000 hPa) shear. The winds retrieved from ELDORA data have height as the vertical coordinate, thus we use 2–6 km for the mid-level shear and 0–2 km for the low-level shear as equivalent criteria with the pressure coordinate.

To examine the vorticity evolution at the meso scales, we use the vertical vorticity equation in Cartesian coordinates neglecting the solenoidal term (Holton 2004, p. 101):

$$\frac{D\eta}{Dt} = -\eta \left( \frac{\partial u}{\partial x} + \frac{\partial v}{\partial y} \right) - \left( \frac{\partial w}{\partial x} \frac{\partial v}{\partial z} - \frac{\partial w}{\partial y} \frac{\partial u}{\partial z} \right) \quad (2.1)$$

where  $\eta$  is absolute vertical vorticity on an  $f$ -plane,  $u$  is zonal velocity,  $v$  is meridional velocity, and  $w$  is vertical velocity. Equation 2.1 states that the rate of change of the absolute vorticity following the motion is determined by the stretching and the tilting terms.

## 2.3 Results

A wide range of spatial scales was important in pre-depression Hagupit's genesis. First, we focus on the impacts of the synoptic scale upper-level trough on the wave pouch at meso- $\alpha$  scale. Then, we will focus on mesoscale processes inside the wave pouch, in terms of localized vertical wind shear, convection, and its associated vorticity generation.

### 2.3.1 Large-scale influences: trough influences on wave pouch evolution

A wave pouch became evident on 12 September and was trackable by the intersection of the critical latitude and the wave trough axis. Figure 2.1 shows vorticity evolution inside the wave pouch from 12 September to 19 September when it was designated as a TD by JTWC. Anomalously high potential vorticity (PV) at 200 hPa was found at the northeast side of the pouch from 13 through 14 September (Figs. 2.1b, c). Figure 2.2 shows the PV intrusion as an upper-level trough in water vapor satellite imagery with dry northerly air impinging on the pre-depression.

Streamline analysis of the wave pouch in a Lagrangian framework from 12 to 19 September is shown in Figs. 2.3 and 2.4. Prior to the trough interaction, on 12 September, the wave pouch had a weak closed circulation at 850 hPa and an open cyclonic wave at 500 hPa at about 200 km east of LLC center. Due to strong VWS during 13–14 September, the mid-level circulation became less organized and further carried away from the LLC center. From the 12th to 14th, the low-level vorticity kept increasing with an approximately closed Lagrangian circulation, but then low-level vorticity decreased and it was the weakest on 15 September. Although the low-level pouch was

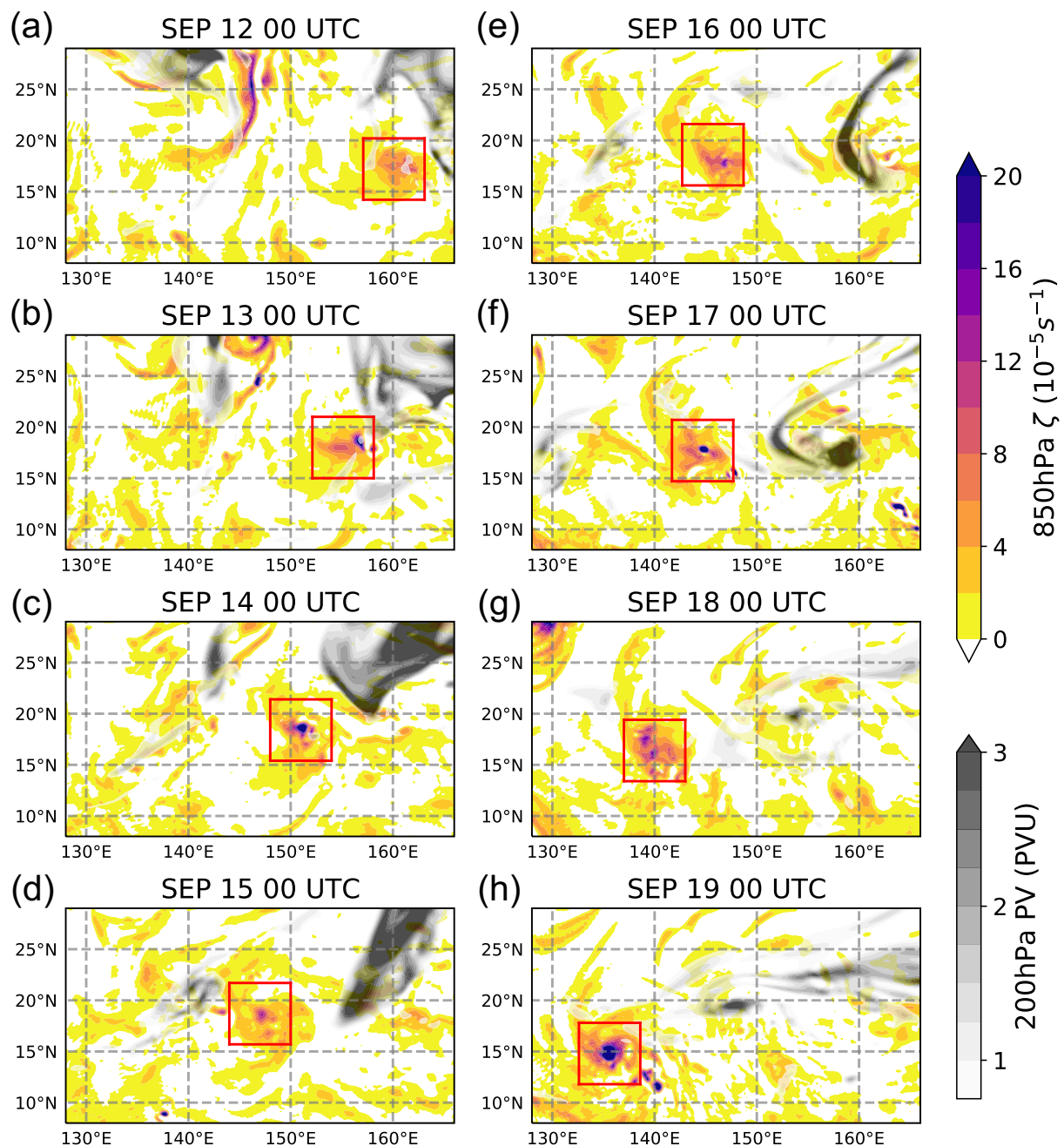


**Figure 2.1:** Vorticity at 850 hPa around pre-depression Hagupit from 0000 UTC 12 September to 0000 UTC 19 September. Red boxes are  $6^\circ \times 6^\circ$  centered on Hagupit's wave pouch at each time. Contoured in gray scale is potential vorticity field at 200 hPa.

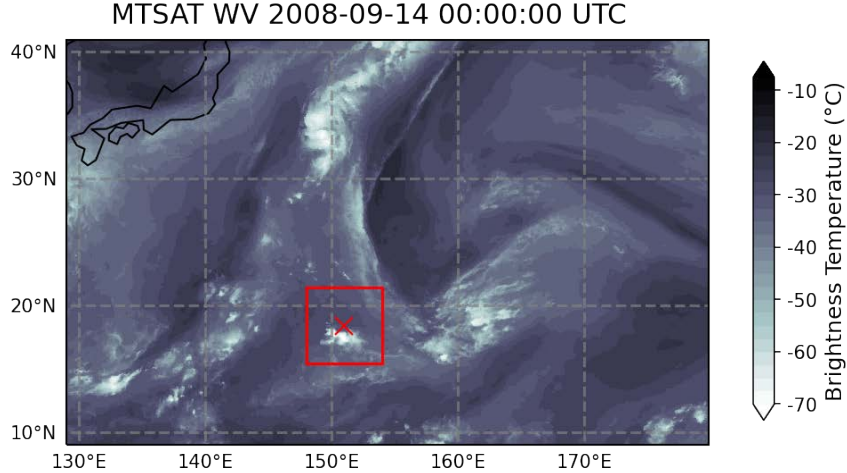


**Figure 2.2:** MTSAT infrared water vapor channel (near  $6.7\text{ }\mu\text{m}$ ) brightness temperature showing pre-depression Hagupit and upper-level trough to the northeast at 2335 UTC 13 September. The red box is  $6^\circ \times 6^\circ$  around the pouch center.

slightly open at its northwestern corner on 15 September (Fig. 2.3d), a two-plane mission around 00 UTC revealed that the LLC was persistent (see Supplemental Fig. ES2). At the mid-level, a weak circulation was evident on the 13th, but was not evident on 14 or 15 September (Fig. 2.3f-h). From the 16th, both low-level and mid-level vorticity started to increase again. On the 17th, the pouch obtained a closed LLC again (Fig. 2.4b), and with northeasterly wind above the easterly wave resulting in northerly vertical wind shear, a mid-level circulation became apparent downshear to the south of the LLC center (Fig. 2.4f). Figures 2.4f-h show that vorticity inside the mid-level circulation was aggregating at the mid-level circulation center from 17–19 September.

Hagupit was designated as a TD on the 19th. At that time, the mid-level circulation was closed and vertically better aligned with the LLC ( $\sim 100$  km apart). From then, the vortex continued intensifying and Hagupit became a Category 4 typhoon on the 23rd and dissipated after landfall in southern China.

Figure 2.5 shows the evolution of circulation, relative humidity, and VWS over the wave pouch area. Figure 2.5c shows that 200–850 hPa VWS was close to  $20\text{ m s}^{-1}$  during 13–14 September averaged over a  $6^\circ$  latitude/longitude square box surrounding the center of the pouch. We chose a  $6^\circ$  box size for analysis as a reasonable compromise to capture environmental influences and to

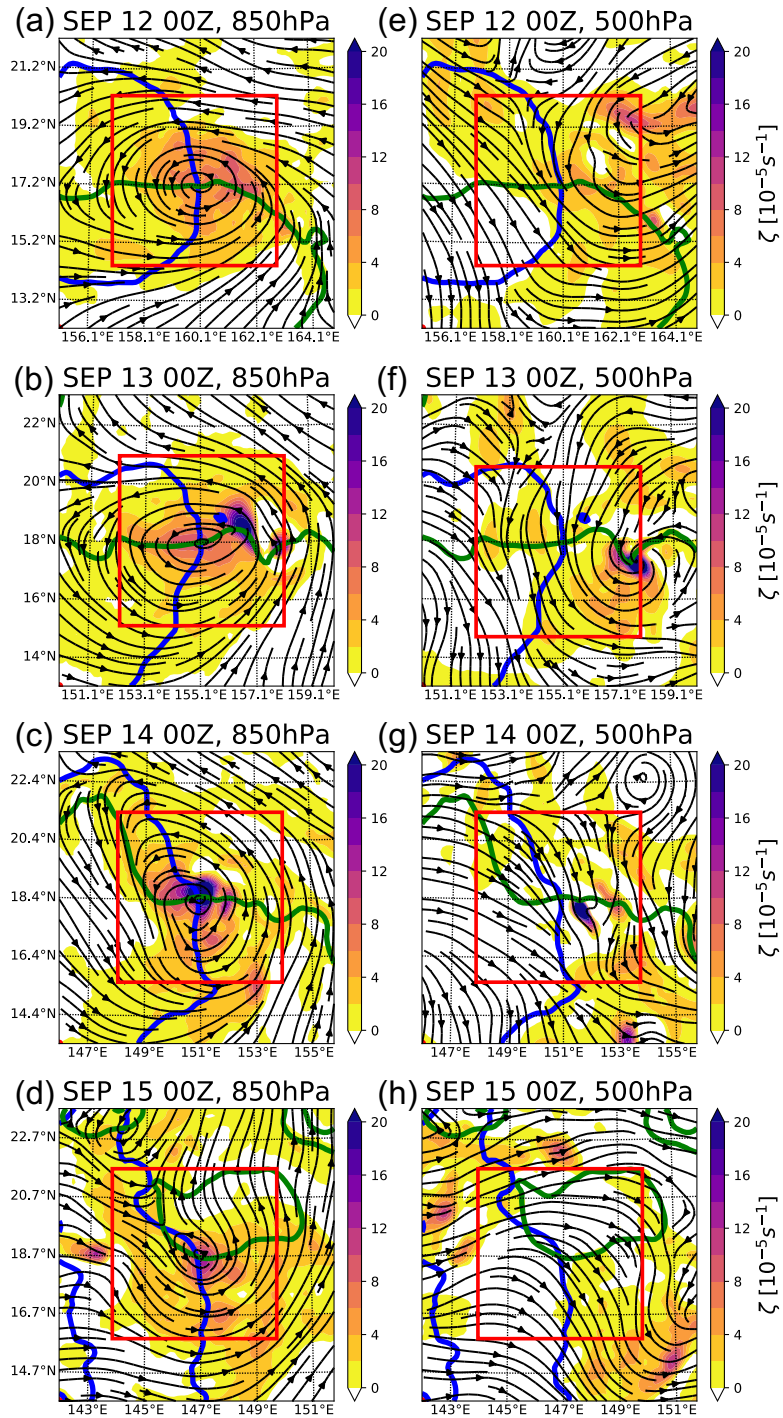


**Figure 2.3:** Streamlines (black contour) and vertical relative vorticity (shading) from 12 to 15 September at 500 hPa and 850 hPa around Hagupit's wave pouch. Green lines indicate the critical latitude (where the zonal flow is equal to the wave phase speed) and blue lines indicate the wave trough axis (where the meridional velocity is zero) at 850 hPa. The center of the wave pouch is defined as the intersection of the green and blue lines. The red box is  $6^\circ \times 6^\circ$  around the pouch center.

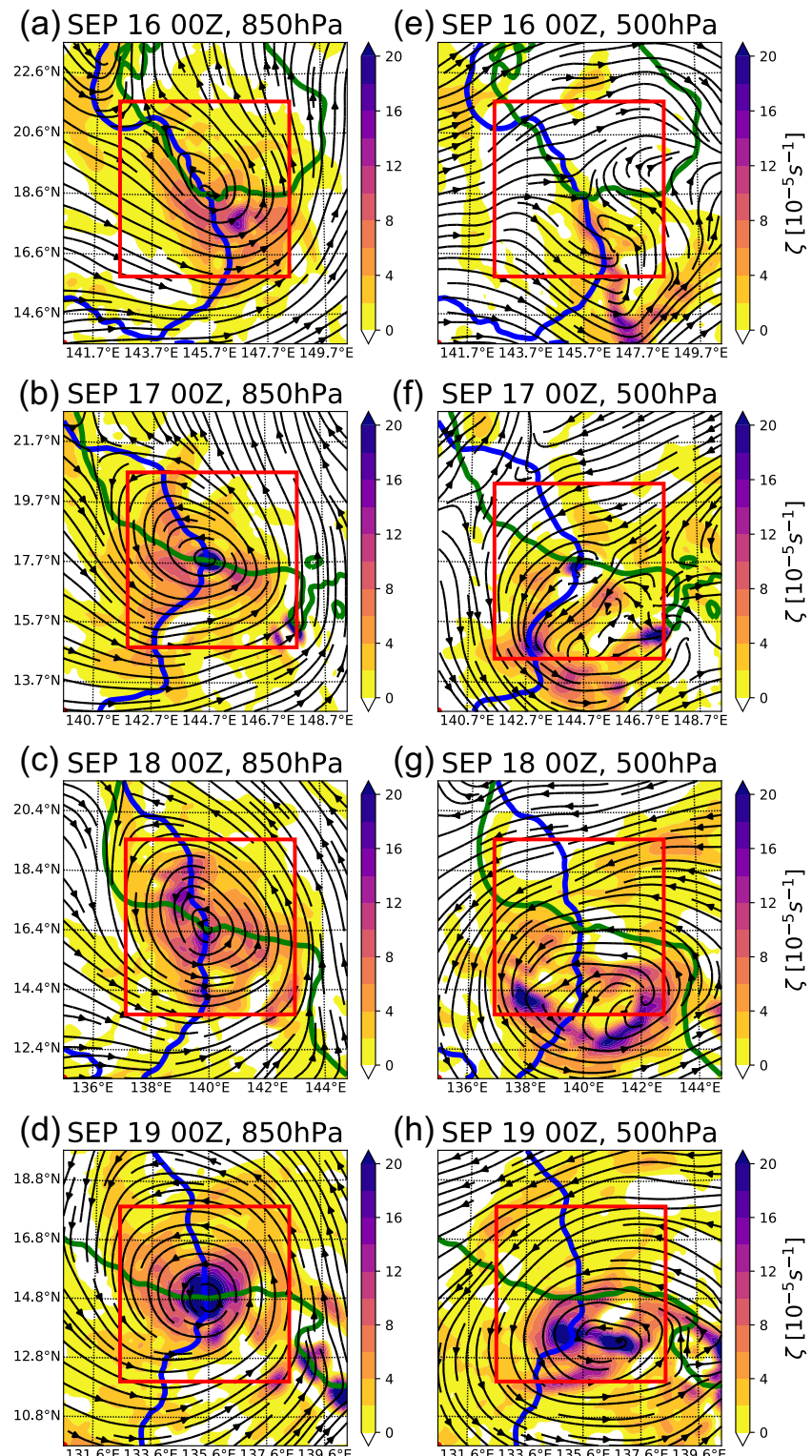
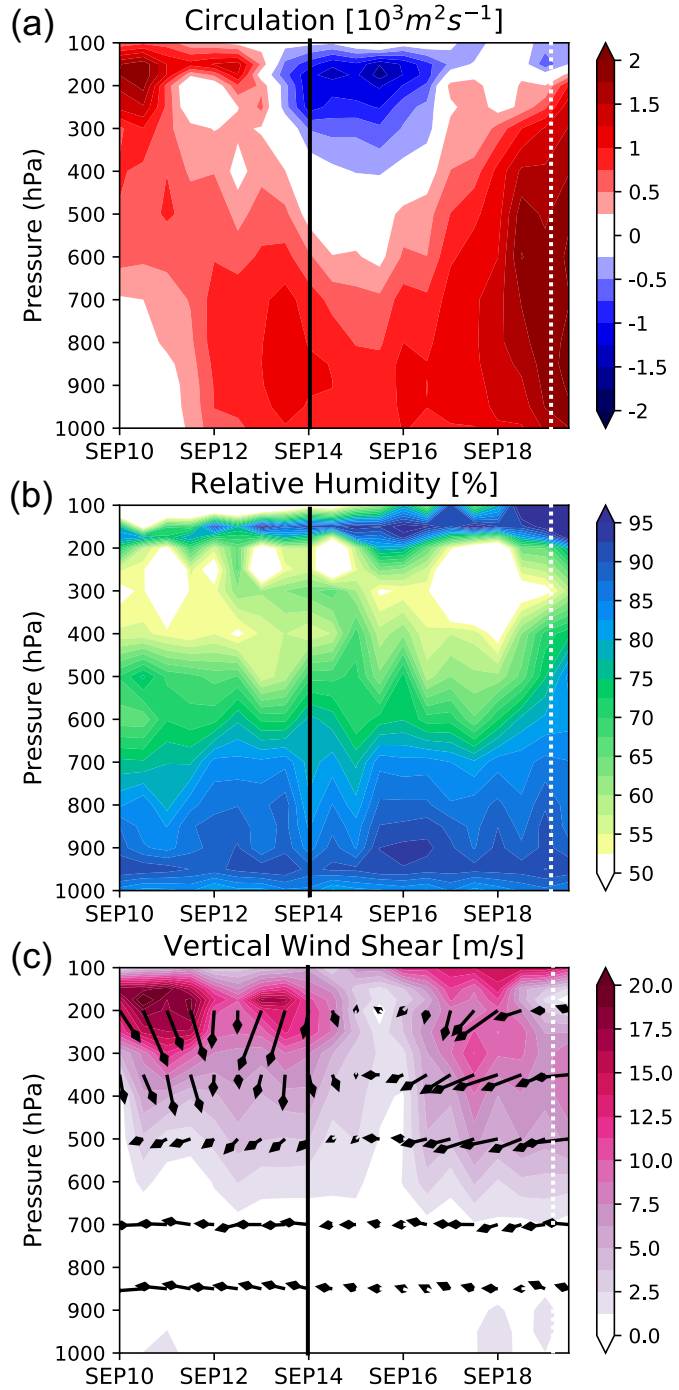


**Figure 2.4:** As in Fig. 2.3 from 16 to 19 September.

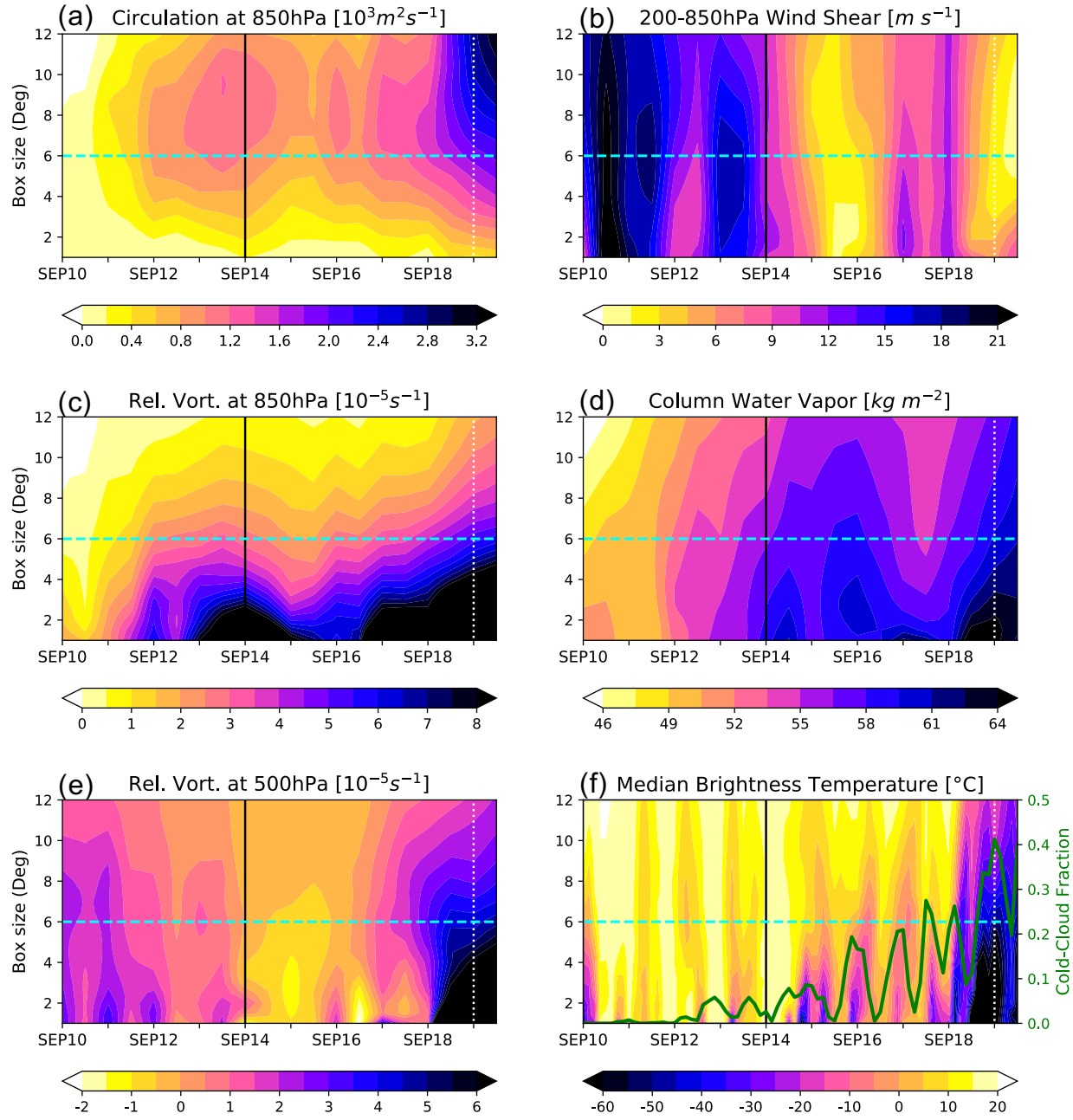
represent the thermodynamic and dynamic characteristics inside the wave pouch. The sensitivity to box size is discussed in the next paragraph. In both TC and non-TC environments, VWS most frequently occurs in shallow layers in the upper troposphere (Finocchio et al. 2016), however the deep-layer VWS is still relevant for the low-level centered wave pouch because the deep convection and stratiform clouds inside the pouch can interact with mid- to upper-tropospheric shear. Under the strong VWS, mid- to upper-level circulation over the wave pouch area decreased significantly, and on 14 September it became anticyclonic (Fig. 2.5a). Low-level circulation, in contrast, kept increasing until the 14th and persisted during the time of strong VWS. Both mid-level and low-level circulation reached a minimum on the 15th and then started to increase again on the 16th. There was some dry air intrusion on 14–15 September resulting in a decrease in relative humidity around 700–850 hPa (Fig. 2.5b).

Figure 2.6 shows the average circulation, low-level/mid-level vorticity, VWS, column water vapor (CWV), and infrared brightness temperature as a function of time for different box sizes following the pouch center. The wave pouch had vorticity and moisture concentrated near the pouch center over time. The average values decrease when they are averaged over bigger square boxes (Figs. 2.6c, d, e). On the other hand, circulation (Fig. 2.6a), which is equal to the integral of vorticity inside the box, increases as the box size increases up to  $8^{\circ}$ , then decreases due to contributions of negative vorticity outside of the pouch (see Figs. 2.3, 2.4). Vertical wind shear magnitude (Fig. 2.6b) is not as sensitive to the box size because it is induced by a synoptic-scale trough.

It is interesting that CWV kept increasing without any hiatus despite the strong VWS during 13–14 September (see Figs. 2.6b, d). Geostationary Infrared brightness temperature (BT) analysis revealed convective bursts having BT colder than  $-60^{\circ}\text{C}$  consistently inside the wave pouch (Fig. 2.6f, and supplemental Fig. ES3). The cold cloud fraction over the wave pouch area (green line in Fig. 2.6f) shows persistent diurnal pulses of convective bursts for 13–15 September. Bell and Montgomery (2010) also documented sheared deep convective cells in Hagupit observed around 00 UTC 15 September. We hypothesize that this consistent convection was still moistening the



**Figure 2.5:** Time-series of vertical structure inside Hagupit's wave pouch (12 hourly averaged over  $6^\circ \times 6^\circ$  box): **a)** circulation, **b)** relative humidity, and **c)** vertical wind shear (VWS) magnitude (color) and wind direction (vector) from 00 UTC 10 September to 12 UTC 19 September. VWS was calculated between each pressure level minus wind at 850 hPa. The black line indicates the aircraft mission (00 UTC 14 September), and the white dotted line marks when Hagupit was designated as a tropical depression by the Joint Typhoon Warning Center (00 UTC 19 September).



**Figure 2.6:** Thermodynamic and dynamic quantities averaged over the box centered on the wave pouch center as a function of time (from 10 September to 19 September) and box length; **a)** Circulation at 850 hPa, **b)** 200 hPa – 850 hPa vertical wind shear, **c)** relative vorticity at 850 hPa, **d)** column water vapor, **e)** relative vorticity at 500 hPa, and **f)** median brightness temperature (BT) from infrared window channel (near 11  $\mu m$ ). The green line on panel (f) shows the fractional coverage of cloud tops of  $-60^{\circ}C$  or colder within  $6^{\circ} \times 6^{\circ}$  square box around the pouch center. Cyan dashed lines indicate the box size that are used in our meso- $\alpha$  scale analysis. The black solid and white dotted lines denote the aircraft mission and genesis as in Fig. 2.5

air column inside the wave pouch on the 13th and 14th. CWV decreased on 17 September under weaker deep-layer (200–850 hPa) VWS compared to the 13–14th, but stronger mid-level (500–850 hPa) VWS (see Fig. 2.5c). Mid-level VWS could be more detrimental to column moistening than deep-layer VWS especially for weaker TCs (Finocchio et al. 2016). However, Fig. 2.6c shows that CWV near the pouch center did not decrease significantly and remained over  $60 \text{ kg m}^{-2}$  until genesis. It is noteworthy that Hagupit was designated as a TC only after the pouch had deepened and acquired a well-defined mid-level vortex. Comparing Fig. 2.6e and Fig. 2.6f, there is a correlation between the rapid increase in mid-level vorticity and cloud top height, indicated by the median BT, over the wave pouch area around 00 UTC 18 September.

Overall, the reanalysis suggests that the wave pouch was able to protect the low-level circulation and moisture during the upper-level PV intrusion on 13–14 September, although the pouch became quite shallow as the mid-level vortex became misaligned or completely dissipated. In the following subsection, we will examine the dynamics and thermodynamics on the mesoscale inside the

### **2.3.2 Upscale vortex merger process: vertical convection in a sheared pre-depression**

A research flight was conducted into pre-depression Hagupit around 0000 UTC on 14 September. In the following section, we investigate the complex local impacts of the VWS on organization and development of convection using high-resolution dual-Doppler radar data (500 m grid spacing) with a short time interval (7 minutes) and vertical thermodynamic profiles from dropsondes. Furthermore, we assess the upscale impacts of the meso- $\gamma$  and meso- $\beta$  scale convective structures on the tropical cyclogenesis of pre-depression Hagupit.

#### **Meso- $\beta$ and meso- $\gamma$ scales: localized shear and convection**

The flight track and the locations of 14 dropsondes deployed during the mission are shown in Fig. 2.7, overlaid over a visible satellite image of Hagupit. The research aircraft flew around 700 hPa pressure level, and the wind barbs indicate winds at 1000 hPa measured by the dropsondes. The wind barbs show a weak cyclonic circulation near the surface with a center that corresponds

well with the pouch center, indicated by the red star ( $18.4^{\circ}\text{N}$   $151^{\circ}\text{E}$ ), calculated from the 850 hPa YOTC reanalysis velocity field. Convection was located to the west and south of the LLC center.

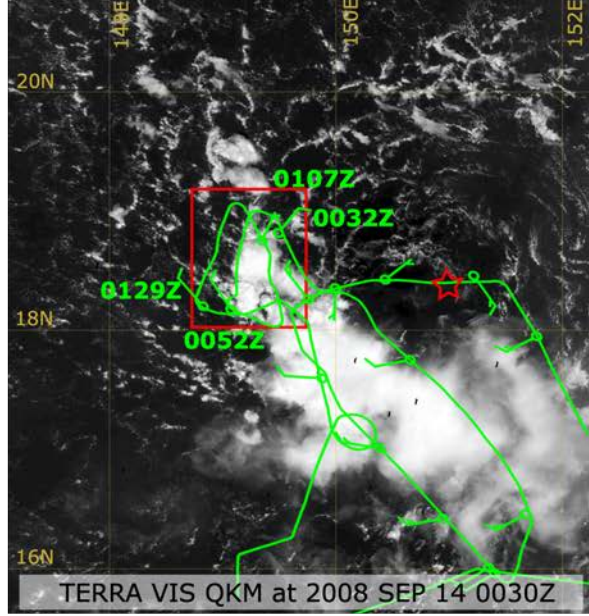


**Figure 2.7:** Visible satellite image with flight track around 700 hPa level in green line and wind barbs denoting 1000 hPa winds measured by dropsondes deployed from the flight mission. The center of the wave pouch ( $18.4^{\circ}\text{N}$   $151^{\circ}\text{E}$ ) is indicated by a red star. Red box denotes the radar analysis domain in Fig. 2.8a

In the red box in Fig. 2.7, the convection is organized linearly like a squall line from north to south. Figure 2.8 zooms in on this convective region and shows vertical vorticity at 2 km altitude calculated from the dual-Doppler analysis overlaid on the radar reflectivity. Two sub-regions along the convective line denoted the North (N) and South (S) box are highlighted in Fig. 2.8a. Figures 2.8 b-c and d-e show the snapshots of N box and S box in seven minute intervals, respectively. The average 2 km reflectivity of the N box is larger than S box. The reflectivity did not change much in seven minutes, but the vorticity evolved noticeably within the same period. There are newly generated vorticity maxima and also several dissipating vortical structures.

Here we focus on the vortical structure of one convective cell in each box (N cell and S cell in Fig. 2.8) that are representative of multiple convective cells in each box. Vorticity budget analysis was conducted for the two cells using Eq. 2.1. The left columns of Figs. 2.9 and 2.10 are snapshots

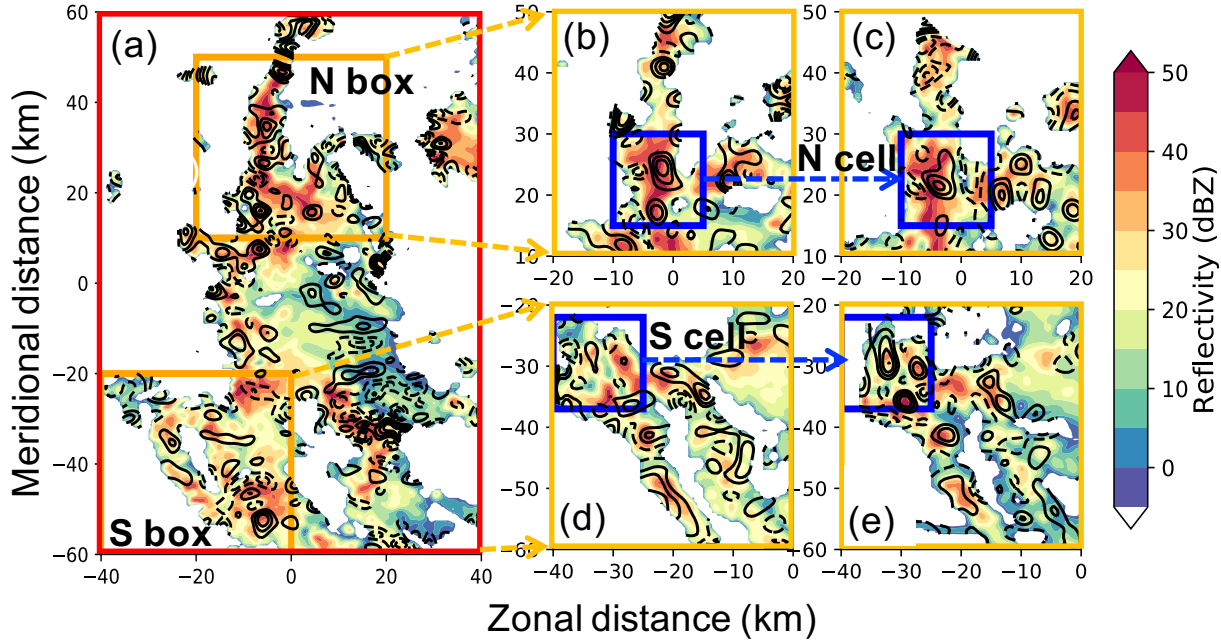


**Figure 2.8:** Radar reflectivity (shading, dBZ) and vertical vorticity (contours,  $1 \times 10^{-3} \text{ s}^{-1}$  with zero omitted and negatives denoted by dashed lines) at 2 km in the zoomed-in domain of the convective area inside the wave pouch of pre-depression Hagupit around 00 UTC September 14. **a)** radar observation composed for 0058–0114 UTC inside the 120 km x 80 km domain (red box in Fig. 2.7). Yellow boxes in panel (a) are zoomed in for more detail: **b)** 0030–0037 UTC, **c)** 0037–0043 UTC, and **d)** 0121–0128 UTC, **e)** 0128–0135 UTC.

of the cells at 0033 and 0125 UTC, respectively. The right columns are seven minutes later (0040 and 0132 UTC). In the first two rows of Figs. 2.9 and 2.10, the stretching and tilting vorticity generation terms are contoured on reflectivity at 2 km altitude. It was not possible to close the vorticity budget due to non-negligible horizontal advection over the seven minute time interval and missing wind data in clear air. The residual was in the same order of magnitude ( $10^{-6} \text{ s}^{-2}$ ) with all the other budget terms.

Starting from Fig. 2.9a, the N cell has a local maximum in stretching larger than  $6 \times 10^{-6} \text{ s}^{-2}$  collocated with a reflectivity maximum above 50 dBZ. The large stretching term results from low-level convergence coincident with a vertical vorticity maximum shown in Fig. 2.9c. Then, seven minutes later, the magnitude of the stretching term significantly decreased (Fig. 2.9f) as the low-level convergence decreased rapidly while the vorticity persisted (Fig. 2.9h). While the low-level convergence decreased, the updraft at 7 km altitude increased from  $12 \text{ m s}^{-1}$  to  $15 \text{ m s}^{-1}$  (Figs. 2.9e, j). Overall, the N cell appears to be a mature cell starting to decay. Although the convection was still active as evidenced by the growing updraft, by 0040 UTC it had lost the low-level supporting convergence.

The S cell had several pronounced differences from the N cell in its vorticity evolution (Fig. 2.10). The S cell was captured during its rapidly developing stage. The maximum reflectivity of the S cell is about 15 dBZ lower than that of the N cell (N cell's maximum above 50 dBZ and S cell's maximum between 35–40 dBZ). During the seven minute interval displayed in Fig. 2.10, S cell's 2 km vorticity and 7 km updraft magnitude tripled. The stretching term cannot explain this vigorous vorticity increase. Prior to the vorticity increase at 0125 UTC the stretching term was not apparent at 2 km (Fig. 2.10a) and there was no significant low-level convergence either (Fig. 2.10c). A positive tilting term is collocated with a weak low-level vorticity center near where the convection erupts. Figure 2.10d shows a weak updraft at 2 km was tilting the northwestward horizontal vorticity vector, which partially contributed to the increase in positive vertical vorticity. By 0133 UTC, the stretching term became the dominant source of vorticity generation as low-level westerly winds increased on the west side of the domain (Fig. 2.10f), resulting in a large

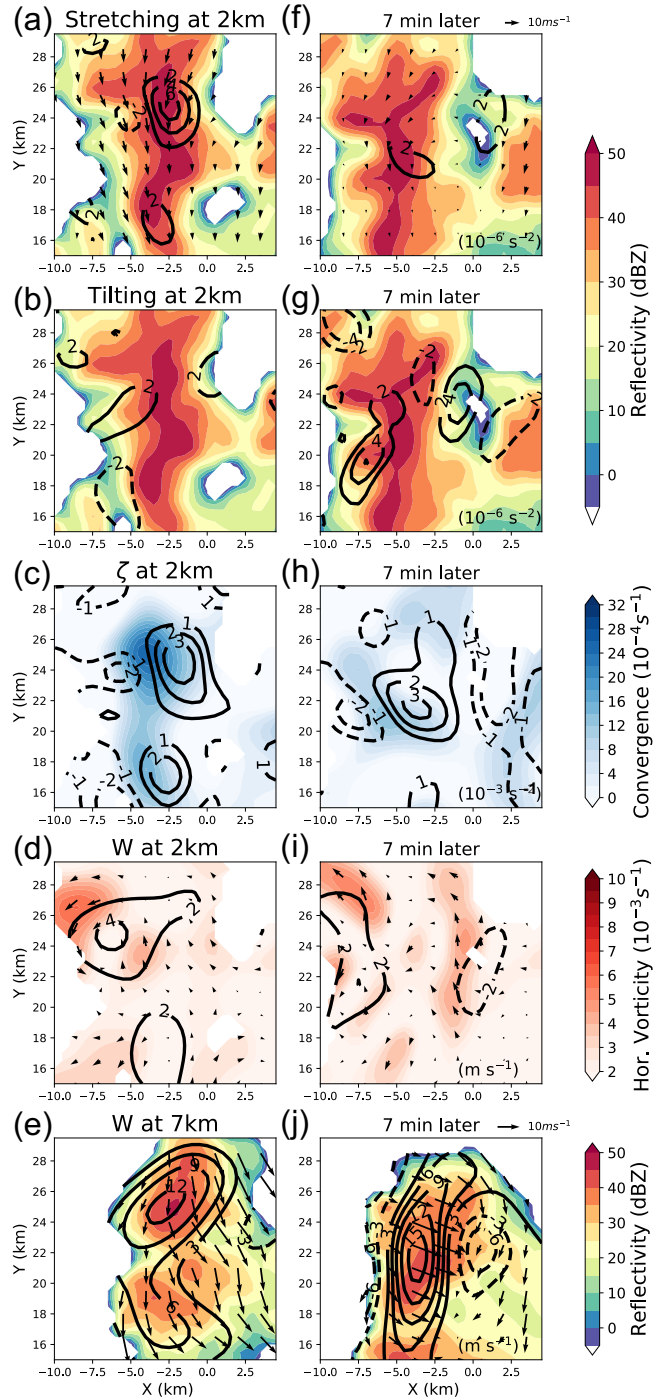


**Figure 2.9:** Meso-gamma scale evolution of N cell from (left panels, (a)-(e)) 0030–0037 UTC flight to (right panels, (f)-(j)) 0037–0043 UTC flight. **a), f)** radar reflectivity (shading), stretching (contours), and horizontal wind velocity (vectors) at 2 km within the 7 minutes time interval. **b), g)** same shading as (a) and (f) but tilting at 2 km as contours. **c), h)** convergence (shading) and vertical vorticity (contours) at 2 km. **d), i)** horizontal vorticity magnitude and direction (shading and vectors) and vertical velocity (contours) at 2 km. **e), j)** radar reflectivity (shading), vertical velocity (contours), and horizontal velocity (vectors) at 7 km. For all contours, zeros are omitted and negative values are denoted with dashed lines.

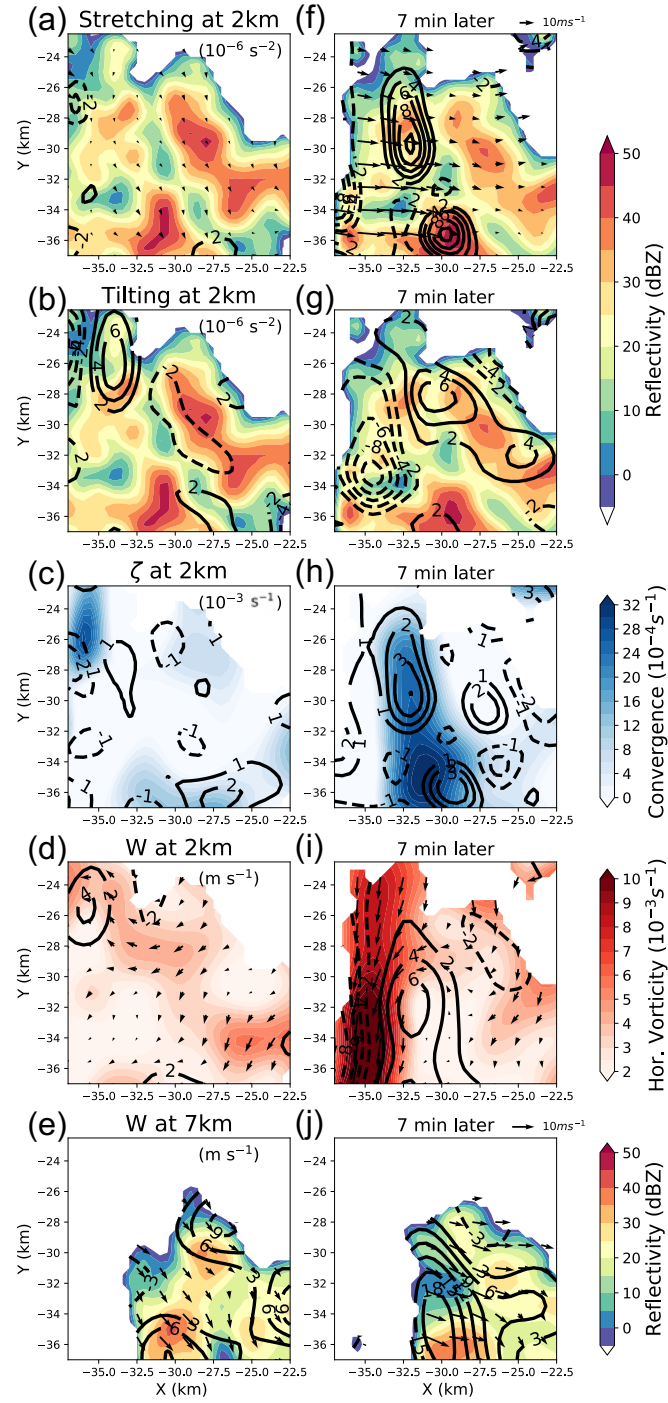


**Figure 2.10:** Meso-gamma scale evolution of S cell from (left panels, (a)-(e)) 0121–0128 UTC flight to (right panels, (f)-(j)) 0128–0135 UTC flight. The panels are the same as in Fig. 2.9.

value of low-level convergence collocated with the vorticity maxima (Fig. 2.10h). The difference of tilting-dominant and stretching-dominant vorticity generation mechanism between S cell and N cell can be explained by two factors: 1) local low-level wind shear and 2) the stage of the convective life-cycle. These factors are further explored using the aircraft observations in the following paragraphs.

Figures 2.11 and 2.12 compare the vertical wind profile and vertical cross-sections of N cell and S cell. Vertical wind profiles inside N box and S box, obtained by the four dropsondes and dual-Doppler radar data, are plotted on the hodographs in Figs. 2.11a-b and 2.12a-b. Dropsonde winds are plotted with cooler colors and radar-retrieved winds are plotted with warmer colors. Dropsonde profiles are available from the surface to the aircraft flight level of 700 hPa (3 km). Winds from dual-Doppler radar are averaged over the  $40 \text{ km} \times 40 \text{ km}$  N box and S box to represent the meso- $\beta$  scale vertical wind profile. The winds from dropsondes and radar are generally in good agreement, although radar low-level winds represent a larger spatial scale than the dropsondes due to coarser vertical resolution and meso- $\beta$  scale averaging.

For the N box, the wind was predominantly from the east or east-north-east around  $7.5 \text{ m s}^{-1}$  from the surface to 5 km (Figs. 2.11a-b). Low-level (surface to 3 km) wind shear produces horizontal vorticity that is then available for tilting into the vertical. The minimal low-level wind shear in the N box explains why the N cell did not have appreciable low-level tilting at this time. In mid-to-upper levels, the wind direction and speed changes to strong northerlies due to the upper-level trough, producing large shear aloft. A vertical cross-section in the N cell (Figs. 2.11c-d) suggests that the cell was in a mature stage and near the end of the convective life-cycle. Between 0033 and 0040 UTC, the reflectivity and the vorticity in the low-levels decreased. In the upper-levels, the echo top of N cell had grown from 12 to 16 km and a very intense vorticity dipole formed above 10 km over the 7 minutes. The dipole is likely due to tilting of shear-generated horizontal vorticity associated with the upper-level trough.

One noticeable difference between N box and S box is that the low-level shear ( $0\text{--}2 \text{ km}$ ) in the S box is stronger and exceeds  $8 \text{ m s}^{-1}$  (Fig. 2.11). As a result, the S box had more horizontal

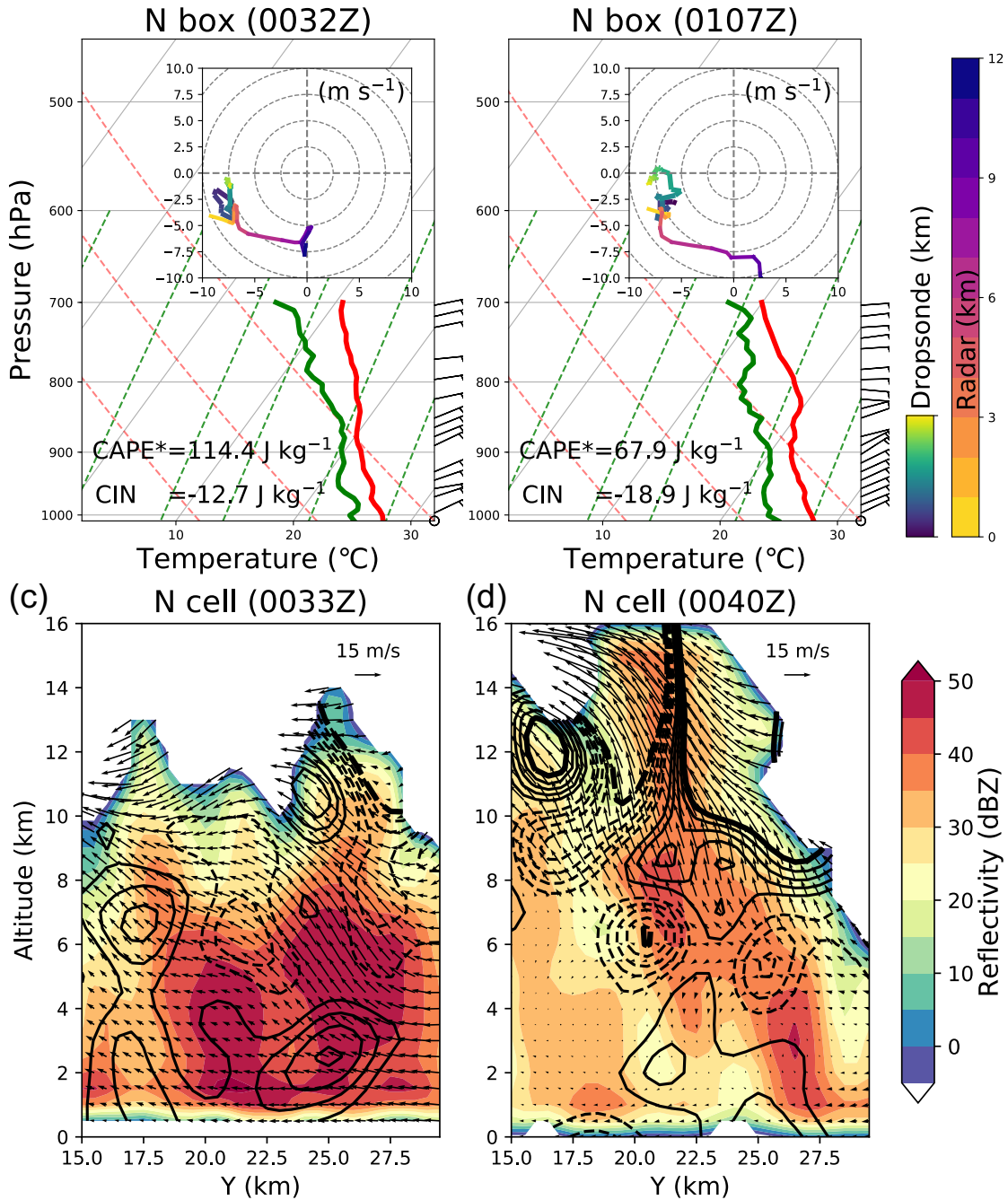


**Figure 2.11:** Meso-gamma scale evolution of N cell from (left panels, (a)-(e)) 0030–0037 UTC flight to (right panels, (f)-(j)) 0037–0043 UTC flight. **a), f)** radar reflectivity (shading), stretching (contours), and horizontal wind velocity (vectors) at 2 km within the 7 minutes time interval. **b), g)** same shading as (a) and (f) but tilting at 2 km as contours. **c), h)** convergence (shading) and vertical vorticity (contours) at 2 km. **d), i)** horizontal vorticity magnitude and direction (shading and vectors) and vertical velocity (contours) at 2 km. **e), j)** radar reflectivity (shading), vertical velocity (contours), and horizontal velocity (vectors) at 7 km. For all contours, zeros are omitted and negative values are denoted with dashed lines.

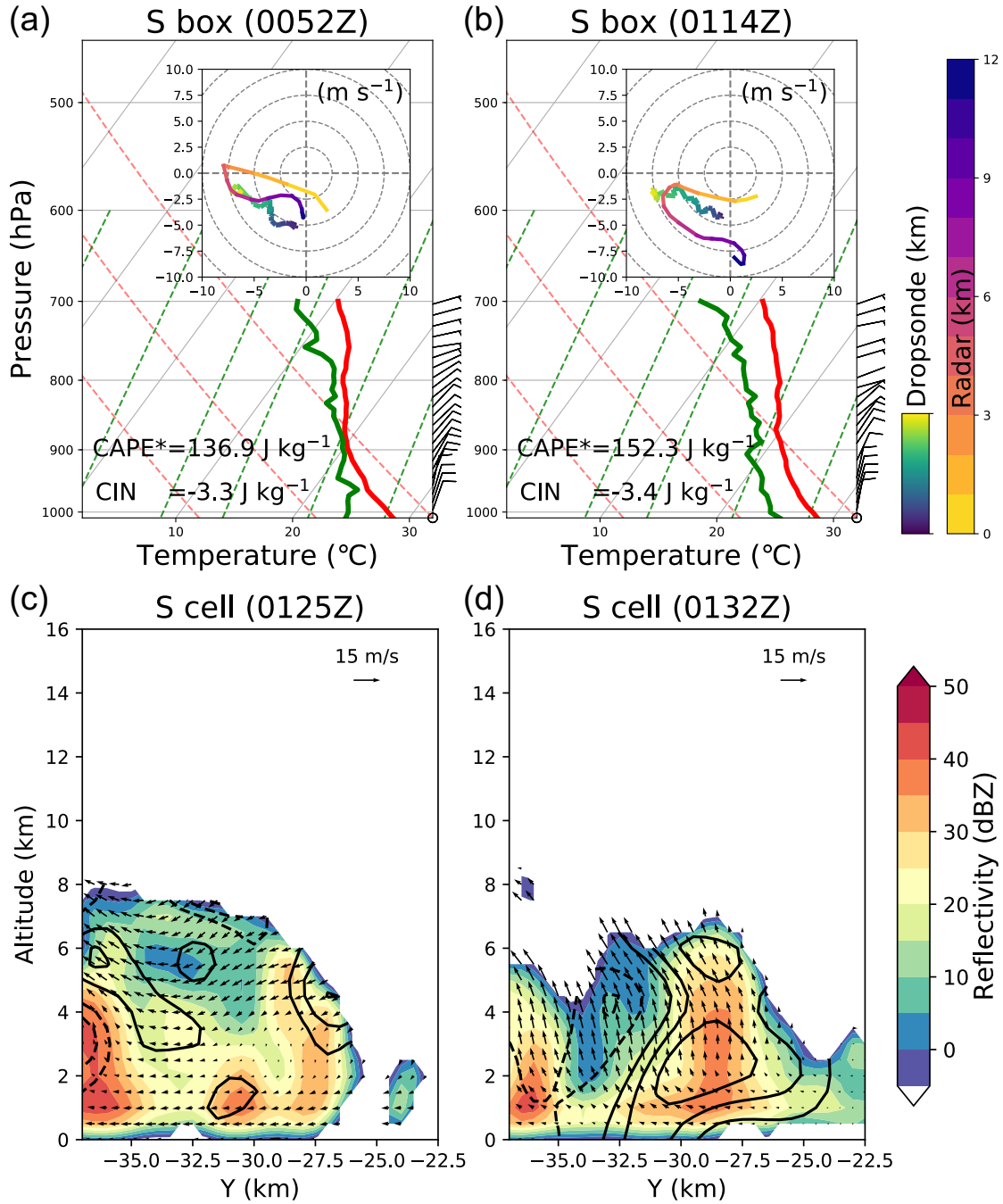


**Figure 2.12:** Meso-gamma scale evolution of S cell from (left panels, (a)-(e)) 0121–0128 UTC flight to (right panels, (f)-(j)) 0128–0135 UTC flight. The panels are the same as in Fig. 2.11.

vorticity which could be tilted into vertical (Fig. 2.10i). In mid- to upper-levels, the wind patterns in both the N box and the S box are similar and dominated by the synoptic scale easterly wave and upper-level trough. The S box has weaker upper-level northerlies compared to the N box, as it is relatively farther from the trough. The near-surface winds are largely determined by the position relative to the LLC which persisted despite the strong deep-layer VWS. The N box was located to the northwest from the LLC center, while the S box was to the west (Fig. 2.8); the near-surface winds shift from east-north-east in the N box to more northerly in the S box, resulting in different low-level VWS across the 80 km distance between the two boxes. The northerly mid-level shear (2–6 km) in N box is parallel to the N-S linear organization in Figs. 2.8b-c. The east-south-easterly strong low-level shear in S box is near parallel to the NW-SE linear squall-line like convection shown in Figs. 2.8d-e. This shear and convective structure relationship is consistent with the findings of LeMone et al. (1998) and Johnson et al. (2005), which will be detailed in the Discussion section.

Skew T – log P diagrams show lower convective inhibition (CIN) and higher convective available potential energy (CAPE) in soundings in the S box (Figs. 2.12a-b) compared to soundings in the N box (Figs. 2.11a-b). The soundings suggest the S box had a slightly more favorable thermodynamic environment for new convective cells to emerge. In Figs. 2.12c-d, the S cell has an echo top below 8 km with increasing reflectivity and vertical vorticity from the low- to mid-levels between 0125 and 0132 UTC. The S cell could be classified as a cumulus congestus in the early stage of the convective life-cycle based on the echo top height and its convective characteristic (Johnson et al. 1999).

Using the N and S cells as representative of the convective and vortical evolution from cumulus congestus to mature deep convection, the analysis suggests that vorticity generation starts from tilting of the ambient horizontal vorticity into the vertical from the initial convective updraft. Enhanced low-level convergence follows as the buoyant plume rises and stretches the vertical vorticity. As the convective cell matures, the buoyancy is consumed and low-level convergence and vorticity decreases. The results suggest that the low-level vertical vorticity generated through the

convective life-cycle outlives the convection consistent with Wissmeier and Smith (2011b) and Kilroy et al. (2014). The role of low-level VWS in helping the convective organization inside the wave pouch and providing ingredients for vorticity amplification via tilting, will be discussed further in the concluding section.

### Meso- $\alpha$ scale: vorticity accumulation inside the wave pouch

Here we quantify the upscale cascade from meso- $\gamma$  scale vorticity generation to meso- $\alpha$  scale system development. Figure 2.13 shows reflectivity and wave-relative meso- $\alpha$  scale winds from the flight mission on September 14th (see Fig. 2.7 for flight track). Streamlines at 10 km altitude (blue) show northwesterly wind over the whole domain associated with the upper-level trough to the northeast of Hagupit. At 1 km altitude, a weak but closed cyclonic circulation is apparent in the wave-relative frame. The convection is not symmetric around the LLC center. The strong convective line, closely examined on meso- $\beta$  and meso- $\gamma$  scales in the previous section, was located to the west of the circulation center. A broad region of stratiform precipitation was located to the south of the LLC center, cyclonically downstream of the convective area. This pattern of the convective initiation at downshear right quadrant and a wider region of stratiform in downshear left is in agreement with the previous studies that have examined the shear-relative convective characteristics of TCs (Corbosiero and Molinari 2002; DeHart et al. 2014), but it is an open question whether this pattern is due to the same mechanism suggested by the previous studies since the pre-depression Hagupit did not have a well-defined mid-level vortex above at this point.

The circulation associated with the convective (orange) and stratiform (green) regions is calculated along the perimeter of each box in Fig. 2.13b. To examine the impacts of convective activity on the circulation, the stretching tendency in each box is calculated as  $-\oint \eta \vec{V} \cdot \hat{n} dl$  (see Eq. (3) of Davis and Galarneau 2009, for the detailed circulation tendency equation). Although the role of tilting in vorticity generation was highlighted above from the meso- $\gamma$  scale analysis, the tilting contribution on the meso- $\alpha$  scale was near-zero (not shown).<sup>2</sup> On September 14th, the YOTC

---

<sup>2</sup>Lifting of a horizontal vortex line produces a dipole of vorticity, such that tilting only affects the circulation if the dipole straddles the boundary. To test the sensitivity to the boundary, we took the ensemble mean of nine different

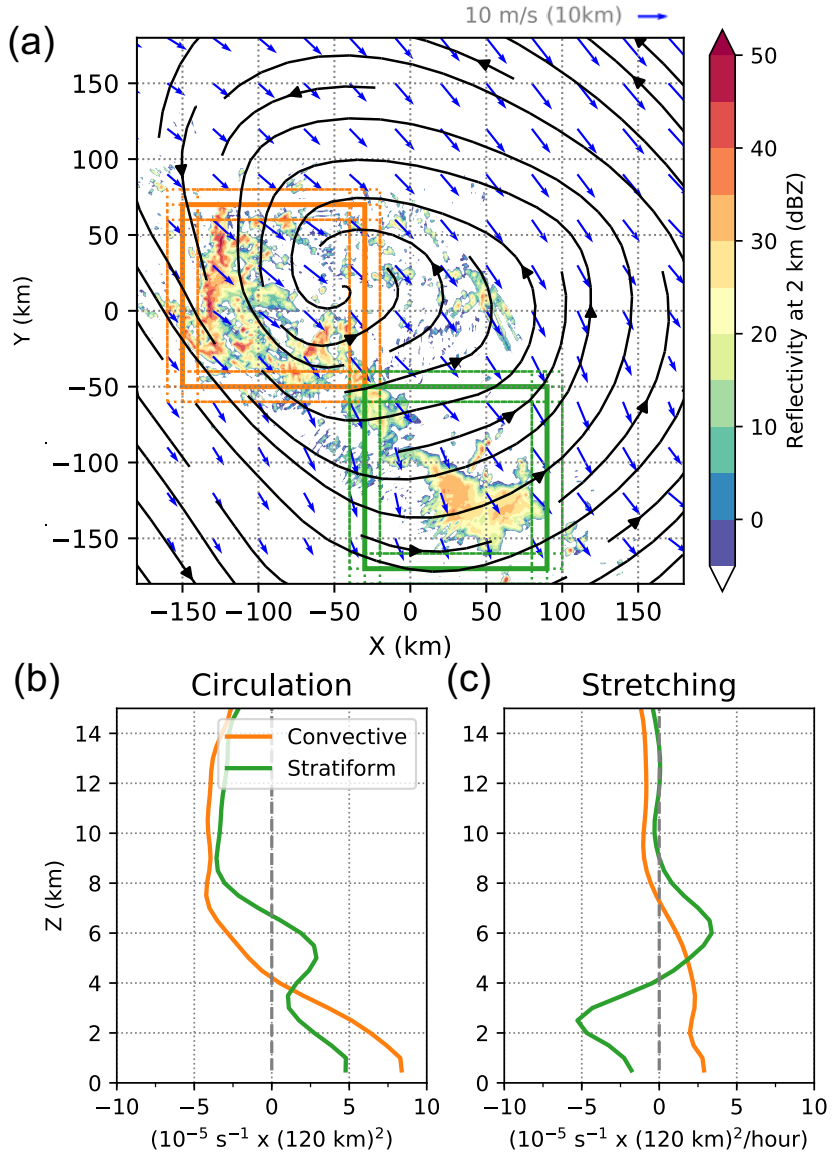


**Figure 2.13:** Meso- $\alpha$  scale structure of pre-depression Hagupit at 0000 UTC 14 September. **a)** radar reflectivity at 2 km (shading) with wave-relative streamlines at 1 km (black) and wind vectors at 10 km (blue). Orange and green boxes are 120 km  $\times$  120 km encompassing regions of primarily convective and stratiform precipitation in the pouch, respectively. The dotted lines indicate nine ensemble boxes shifted for (-10, 0, 10 km) in x- and y- direction. **b-c)** circulation and stretching tendency with height, respectively. Orange and green lines are averaged over the nine dotted orange and green boxes in panel (a).

analysis shows that circulation of pre-depression Hagupit was decreasing throughout the whole vertical column (Fig. 2.5), yet the meso-scale radar analysis indicates that vertical vorticity was being actively generated through stretching in the convective area. The depth of the cyclonic circulation was generally below 4–6 km (Fig. 2.13b), and the convective region had positive stretching from the surface up to 6 km (Fig. 2.13c). While the convective region shows positive circulation maximized near the surface, the stratiform region shows two peaks in the vertical profile of circulation - one near the surface and another in the mid-level around 5 km (Fig. 2.13b). As shown in Fig. 2.13c, stratiform precipitation has mid-level convergence and low-level divergence and thus positive stretching at the mid-levels and negative at the low-levels. At the level of maximum convergence in the stratiform region of an MCS, a mid-level mesoscale convective vortex (MCV) can form (e.g. Houze Jr. 2004).

Once created, the vorticity generated in the convective and stratiform areas outlives the convection (Fang and Zhang 2011; Wissmeier and Smith 2011b; Davis 2015). Thus, vorticity can be accumulated inside the closed circulation of the pouch, and aggregated through a vortex merger process (Van Sang et al. 2008). The results presented here support the conclusions of previous studies that argued that deep convection plays a primary role in genesis by generating vorticity through stretching (Ooyama 1969; Zehr 1992; Raymond et al. 1998; Bell and Montgomery 2019). The results are consistent also with the hypothesis of Bell and Montgomery (2019) that stratiform precipitation that forms from the waning convection plays an important supporting role by strengthening the mid-level circulation.

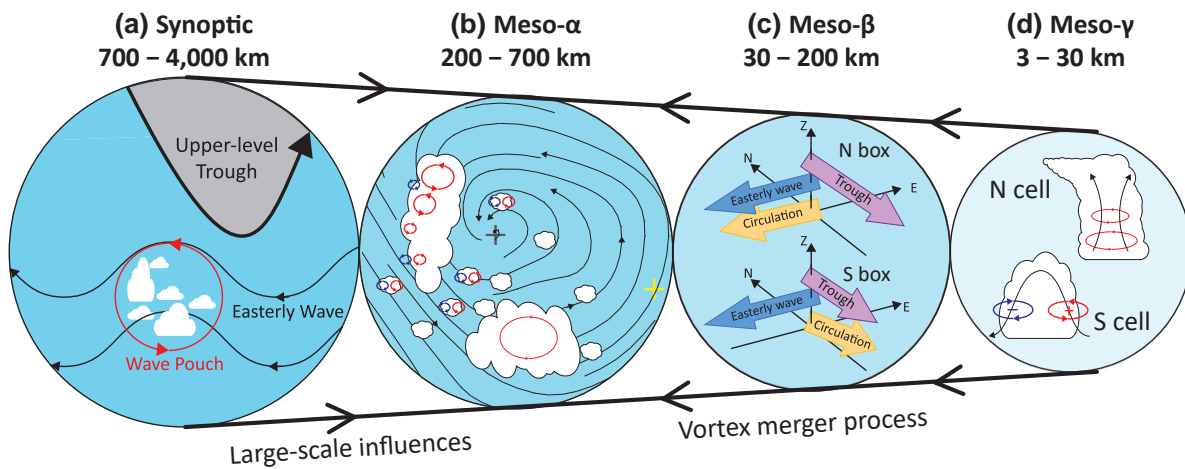
## 2.4 Discussion and Conclusions

Figure 2.14 summarizes the key results from this study and the multi-scale interactions of Hagupit's cyclogenesis in a sheared environment. This telescoping schematic depicts the important factors at each spatial scale inside the circles. The most important factors at synoptic scale (Fig. 2.14a) include the upper-level trough and easterly wave carrying the marsupial wave pouch. The

---

boxes around the convective and stratiform regions (dotted boxes in Fig. 2.14a). Taking the ensemble-mean of the tilting term for the nine boxes with 10 km shifted locations resulted in near-zero net impacts of tilting.

recirculating wave pouch is at meso- $\alpha$  scale (Fig. 2.14b), and it is the focal point where the downscale influences from synoptic scale and the upscale cascade from meso- $\beta$  and - $\gamma$  scales meet. At meso- $\beta$  scale (Fig. 2.14c), the local VWS profile and its impact on squall-like convective organization is illustrated. Finally, at the meso- $\gamma$  scale (Fig. 2.14d), there are convective cells producing vorticity through stretching and tilting through interaction of the updraft with the local shearing flow throughout the convective life-cycle. Below, we will discuss each circle in more detail incorporating the relevant results.



**Figure 2.14:** Schematic of the multi-scale interactions in Hagupit's cyclogenesis. **a)** Synoptic scale active features are the upper-level trough and easterly wave which carries the marsupial wave pouch, denoted as red circulation. **b)** In the meso- $\alpha$  scale wave pouch, the low-level cyclonic streamlines are shown with circulation center marked with black cross and mid-level center as yellow cross. Overlain on the clouds to the southwest of the low-level center is vorticity (positive: red, negative: blue), illustrating vorticity dipoles from tilting, enhanced vorticity from stretching, and a mid-level MCV over the stratiform area. **c)** In the meso- $\beta$  scale, the local wind shear profile that influences the convective organization is composed of winds from cyclonic circulation inside pouch, easterly wave propagation, and the trough. **d)** Meso- $\gamma$  scale convective cells produce vorticity that serve as building blocks for the wave pouch intensification through tilting of horizontal vorticity associated with low-level wind shear (S cell) and stretching of the local vertical vorticity (N cell). See text for description of each physical process.

Tropical cyclogenesis of pre-depression Hagupit was delayed while it interacted with upper-level trough, experiencing strong VWS. For the downscale influences from the synoptic to meso- $\alpha$  scale, our analysis showed that pre-depression Hagupit was significantly affected by the strong

northerly vertical wind shear. The mid-level vortex of the pre-depression was shifted to the south-east (Fig. 2.14b yellow cross), and became misaligned with the low-level vortex by more than  $5^{\circ}$  (Figs. 2.3 and 2.4). In addition to the vortex misalignment, convective precipitation was shifted to the southwest of the LLC center (Fig. 2.7, Fig. 2.13a, Fig. 2.14b).

However, Hagupit survived through the hostile, strongly sheared environment, and eventually developed into a tropical cyclone after it escaped from the influence of upper-level trough. Despite the shear and misalignment, the low-level circulation inside the wave pouch persisted through 13–14 September. Then, during 16–17 September the wave pouch deepened and developed a mid-level vortex, which ultimately led to designation as a tropical depression on 19 September (Fig. 2.5a, Fig. 2.6e). It is hypothesized that the upscale cascade from the persistent deep convection (Fig. 2.6f) and its vorticity amplification through vortex tube stretching (Fig. 2.13, Fig. 2.14d) was a key process that enabled the pouch to persist even under strong VWS. The localized vertical vorticity generated from deep convective cells is aggregated through a vortex merger process in the closed Lagrangian circulation inside the marsupial pouch (Fig. 2.14b).

In the meso- $\beta$  scale circle (Fig. 2.14c), we illustrate the localized shear profile and how that impacts the organization of the convective cells and vortical characteristics of the MCSs inside the wave pouch. The shear profile depended on the distance from the upper-level trough and relative location from the LLC center (Fig. 2.12). Comparing the meso- $\beta$  scale N box and S box, the influence of the trough is reduced to the south, while the magnitude of low-level shear is increased across the 100 km distance. The mid-level shear (500–800 hPa) was generated by the difference between the easterly wind and the upper-level trough. The low-level shear (800–1000 hPa) was generated by the difference between the cyclonic circulation near the surface and easterly wind at mid-levels associated with the easterly wave. The linear organization of convection in N box and S box can be explained by the low-level and mid-level shear configuration in each box. LeMone et al. (1998) proposed a conceptual framework for the relationship between the shear profile and the mesoscale convective structure in the tropics based on the Tropical Ocean Global Atmosphere Coupled Ocean–Atmosphere Response Experiment (TOGA COARE), and Johnson et al. (2005)

added two new categories to the frame work based on South China Sea Monsoon Experiment (SC-SMEX). In the N box, the mature N-S linear convection agrees with the convective structure mode with large northerly mid-level shear and small low-level shear (category 3 of LeMone et al. 1998).<sup>3</sup> In the S box, the characteristic and orientation of the squall-line like convection is consistent with the convective structure mode under strong low-level shear and weak mid-level shear (category 2r of Johnson et al. 2005). This mode is characterized with dry air aloft with linear organization parallel to the low-level shear vector and relatively short ( $\sim 7$  km echo top) and weak (maximum below 40 dBZ) reflectivity. The geometry of the situation suggests that in general for a wave pouch carried by an easterly wave, the low-level shear should be the largest to the south of the LLC center and the smallest to the north. In general, easterly waves have maximum easterly winds at 700–850 hPa (Serra et al. 2008), and with the cyclonic circulation near the surface, westerlies can be found to the south of the LLC center and easterlies to the north. Whether the arrangement of low-level shear and organization of convection with respect to the LLC and the marsupial wave can be generalized to other tropical cyclogenesis cases beyond Hagupit is an interesting topic for future research. We note that the low-level shear organizes convection, but that convective processes such as cold pools can affect shear profiles in turn. Given the consistent low-level shear profile for 30 minute period in both the N box and the S box (Figs. 2.11 and 2.12), we believe the shear profiles in the meso- $\beta$  scale are largely controlled by the downscale processes from synoptic and meso- $\alpha$  scales.

In the meso- $\gamma$  scale circle (Fig. 2.14d), vortical convection is illustrated. The convective cells are the building blocks for the pre-depression intensification. The wave pouch protects the convective cells from environmental dry air induced by the upper-level trough. Then the convective cells, in turn, enhance the circulation by generating and amplifying vertical vorticity. In the S box, where low-level shear was much stronger than N box, the convective cells (e.g. S cell) had larger values of the tilting term in the low-levels. Congestus clouds like the S cell can provide initial vertical vorticity by tilting the horizontal vortex tube. The importance of low-level shear

---

<sup>3</sup>Note the difference between mid-level shear definition of our study (800–500 hPa) and that of LeMone et al. (1998) and Johnson et al. (2005) (800–400 hPa).

and tilting in the incipient tropical disturbance prior to genesis was emphasized by Davis (2015). In the weak cyclonic environment of the pre-depression, tilting by cumulus congestus can play a major role providing the initial vertical vorticity to stretch. Tilting alone cannot contribute to net increase of vorticity in the wave pouch as long as the wave pouch fully encompasses both cyclonic and anticyclonic parts of vorticity dipoles generated by tilting. However, the cyclonic part of the dipole can be stretched further by the maturing convective cell (Hendricks et al. 2004; Montgomery et al. 2006). Then, stretching can produce a net positive vorticity generation in meso-gamma scale, which can feed up to meso-alpha scale (Fig. 2.13c).

Recent observational studies have found that higher mid-level humidity is one of the most distinctive differences between developing and non-developing disturbances (Montgomery et al. 2012; Davis and Ahijevych 2013; Komaromi 2013; Zawislak and Zipser 2014). Despite the evident vortex misalignment at mid-levels, Hagupit's low-level recirculating pouch was apparently able to continue providing moisture above the boundary layer (Fig. 2.5b). The closed low-level pouch protected the developing disturbance from nearby dry air intrusions. Then the convective clouds initiated from the low-level (especially convective congestus) moisten the mid-troposphere above the boundary layer through vertical moisture flux (Wang 2014). The continuous moistening inside the wave pouch evident in reanalysis (Figs. 2.6) suggests that the convection on the 14th was able to sufficiently maintain the pre-depression. It is noteworthy that Hagupit had a favorable sea surface temperature throughout its pre-genesis to genesis period above 30 °C that supported strong surface moisture flux.

Hagupit intensified into a TD only after it had a mid-level vortex above the low-level circulation. The rapid increase in cold cloud coverage over the wave pouch area was correlated with the mid-level vorticity intensification around 00 UTC 18th September (Figs. 2.6e,f). Previous studies have shown that mid-level vortex can spin up through the convective processes, including vertical vorticity advection from deep convection (e.g. Chen et al. 2018) and mid-level stretching associated with ice processes from stratiform precipitation (e.g. Bell and Montgomery 2019). Our ability to explain the later period of Hagupit genesis in 16–19 September is limited because we do

not have high resolution radar observation for this period, but we hypothesize that the feedback of water vapor, convection, and circulation in the early stage of Hagupit's tropical cyclogenesis during 13–15 September allowed for the subsequent genesis process of vortex realignment and precipitation symmetrization after Hagupit escaped from the upper-level trough and strong VWS (Rios-Berrios et al. 2018; Chen et al. 2018).

This case study provides a detailed observational analysis of multi-scale processes around an incipient wave pouch surviving through strong VWS. Further observational and modeling studies are needed to investigate the complex processes across spatial scales during tropical cyclogenesis, especially in sheared environments. The roles of localized low-level shear and cumulus congestus clouds inside the wave pouch at the early stage of tropical cyclogenesis in particular warrant further exploration.

## **Chapter 3**

# **Bifurcation points for tropical cyclone genesis in sheared and dry environments**

### **3.1 Introduction**

In order to improve tropical cyclone (TC) intensity forecast skill, it is necessary to identify the sources of uncertainty in predicting TC formation. Vertical wind shear (VWS) is one of the most important factors for TC genesis and intensity change. Weak VWS makes a favorable environment for TC development, while strong VWS could tear apart the TC vortex. Moderate vertical wind shear (VWS) is defined as the range of VWS magnitudes that are neither too weak to have negligible impacts on TC intensity change nor too strong to completely thwart TC intensification. Ensemble modeling studies of Tao and Zhang (2015) showed that tropical cyclogenesis and intensification is the most unpredictable with moderate VWS. The climatological study of Rios-Berrios and Torn (2017) also verified that the likelihood of intensifying or weakening is comparable with moderate VWS, whereas the likelihood is skewed toward intensification or weakening for weak and strong VWS, respectively.

Another factor that increases uncertainty around tropical cyclogenesis is environmental dry air. Moisture is essential to sustain moist convection that fuels tropical cyclones, such that dry atmosphere can suppress TC development. Studies comparing developing and nondeveloping tropical disturbances have found that a key difference is the moisture, especially the mid-level humidity (Peng et al. 2012; Montgomery et al. 2012; Davis and Ahijevych 2013). The dry mid-level air affects the overall upward vertical mass flux via entrainment of less buoyant air parcel (James and Markowski 2010) and convective downdrafts into the subcloud layer (i.e., downward ventilation), which results in a longer recovery time for subsequent deep convection (Alland et al. 2017). The

ventilation process is more efficient with VWS as the vortex tower is tilted by shear and both radial and downward ventilation can more easily impact the inner-core convection (Alland et al. 2021). Tao and Zhang (2015) showed that the uncertainties around intensification scenarios increase with ventilation, until ventilation is too big to make an extremely hostile condition for TCs.

A developing TC is at the border of stochastic cloud-organizing mesoscales and quasi-balanced synoptic scale (Ooyama 1982). Our hypothesis is that the stochastic character of moist convection is more dominant in marginally favorable environments such as moderately sheared and dry environments. In this study, we aim to gain a process-based understanding on why the combination of moderate VWS and environmental dry air makes an unstable and uncertain setup for TC genesis. Recent observational and modeling studies revealed that TCs that successfully develop or intensify under moderate to large VWS undergo "downshear reformation" (Nguyen and Molinari 2015; Rios-Berrios et al. 2018; Chen et al. 2018; Nam and Bell 2021). The downshear reformation process starts with convection shifted to the downshear area by the VWS. Inside the convective area in the downshear region, vorticity is produced through vortex tilting, vortex stretching, and vertical advection of vorticity. The newly produced vorticity is accumulated inside the broader circulation through a vortex merger process. Thus, multiple thermodynamic and dynamic processes need to come together: namely, deep convection in the downshear region, vorticity generation, and vortex alignment through vortex merger. Then, our question is which processes may lead to bifurcation points between the TCs that do develop and the ones that are suppressed under the same magnitude of VWS.

A number of idealized TC simulation sets with 20-member ensembles with varying VWS magnitude and environmental humidity are used to answer the above scientific question. Sensitivity to different types of initial vortex (mid-level centered and weaker vortex) was also explored. The ensemble numerical simulations have been used by many TC studies that examine the intrinsic predictability of weather (e.g. Lorenz 1969; Melhauser and Zhang 2012). The rest of this chapter is outlined as follows. Section 3.2 entails the experimental design and the ensemble model setup. Section 3.3 describes the results from those simulations, emphasizing different bifurcation points

of TC development depending on the environmental conditions. Section 3.4 synthesizes the results and explores the underlying cause of the uncertainties for the marginally favorable environments.

### 3.2 Experimental Design and Model Setup

Tropical cyclone interactions with vertical wind shear and dry environment were simulated with the Advanced Research version of Weather Research and Forecasting (ARW-WRF; Skamarock et al. 2008) Model. Three two-way nested domains were used with 18-, 6-, and 2-km horizontal grid spacing. The three domains contained 240 x 240, 240 x 240, and 360 x 360 grid points respectively, which yields the domain sizes of 4320 km x 4320 km, 1440 km x 1440 km, and 720 km x 720 km. All domains had 40 vertical levels with the model top at 20 km. The two inner domains were designed to follow the center of the prescribed vortex center at 850 hPa level. The configuration and choice of physics packages included Yonsei University (YSU) boundary layer scheme (Hong et al. 2006), WRF single-moment 6-class (WSM6) microphysics (Hong et al. 2004). No cumulus parameterization nor short- or long-wave radiation schemes were used in our simulations.

Table 3.1 shows descriptions of all the ensemble sets analyzed in this study. There are in total 9 different experimental sets as the Main Set to investigate the combined impacts of shear and dry air, and three additional experimental sets to investigate sensitivity to vortex structure.

For all simulations, a weak, warm-core vortex was prescribed in the initial conditions with a modified Rankine vortex profile having a set maximum tangential wind (15 or  $12.5\text{ ms}^{-1}$ ) at 850 hPa height and 135-km radius. All simulations were set on a constant sea surface temperature (SST) of 29 °C and a constant planetary vorticity (i.e., a doubly periodic f-plane) corresponding to 20°N.

Around the tropical cyclone-like vortex, different profiles of environmental winds, and thermodynamic soundings were specified. The 9 sets of the Main Set have each combination of 3 different vertical wind shear profiles and 3 environmental moisture profiles, and run with WRF version 3.1.1. These ensembles of the Main Set were previously shown and analyzed in ensemble

**Table 3.1:** List of experiments with corresponding experimental setups.

	Name	WRF	Wind Shear	Outer-core Moisture	Initial Vmax
MAIN SET	SH10_Moist100	3.1.1	$10 \text{ m s}^{-1}$	Dunion Non-SAL	$15 \text{ m s}^{-1}$ at 850-hPa
	SH10_Moist50	3.1.1	$10 \text{ m s}^{-1}$	50% of Moist100	$15 \text{ m s}^{-1}$ at 850-hPa
	SH10_Moist25	3.1.1	$10 \text{ m s}^{-1}$	25% of Moist100	$15 \text{ m s}^{-1}$ at 850-hPa
	SH7.5_Moist100	3.1.1	$7.5 \text{ m s}^{-1}$	Dunion Non-SAL	$15 \text{ m s}^{-1}$ at 850-hPa
	SH7.5_Moist50	3.1.1	$7.5 \text{ m s}^{-1}$	50% of Moist100	$15 \text{ m s}^{-1}$ at 850-hPa
	SH7.5_Moist25	3.1.1	$7.5 \text{ m s}^{-1}$	25% of Moist100	$15 \text{ m s}^{-1}$ at 850-hPa
	SH5_Moist100	3.1.1	$5 \text{ m s}^{-1}$	Dunion Non-SAL	$15 \text{ m s}^{-1}$ at 850-hPa
	SH5_Moist50	3.1.1	$5 \text{ m s}^{-1}$	50% of Moist100	$15 \text{ m s}^{-1}$ at 850-hPa
	SH5_Moist25	3.1.1	$5 \text{ m s}^{-1}$	25% of Moist100	$15 \text{ m s}^{-1}$ at 850-hPa
SENSITIVITY	REF	3.9	$7.5 \text{ m s}^{-1}$	50% of Moist100	$15 \text{ m s}^{-1}$ at 850-hPa
	Midlevel	3.9	$7.5 \text{ m s}^{-1}$	50% of Moist100	$15 \text{ m s}^{-1}$ at 600-hPa
	Weak	3.9	$5 \text{ m s}^{-1}$	Dunion Non-SAL	$12.5 \text{ m s}^{-1}$ at 850-hPa

mean perspective in Tao and Zhang (2014b). For the vortex structure sensitivity runs, a newer version of WRF (3.9) was used.

Figure 3.1 describes the environmental setup. Figure 3.1a shows the vertical profile of zonal that is prescribed for the simulations. For SH5, SH7.5, and SH10 configurations, westerly vertical wind shear of 5, 7.5, and  $10 \text{ ms}^{-1}$  was imposed with a method of “point-downscaling” developed by Nolan (2011).

For Moist100 simulations, the Dunion non-SAL mean hurricane season sounding (Dunion 2011) was used for the initial thermodynamic profile. To investigate the impact of environmental dry air intrusion, for Moist50 and Moist25 sets, the initial field of water vapor mixing ratio was modified as shown in Fig. 3.1b, as the water vapor mixing ratio for all heights in outer-core regions (outside the radius of 300 km) is reduced to 50% and 25% of the Dunion non-SAL sounding. For all simulations, the moisture is set the same in the inner-core regions (within a 200 km radius), and between 200- and 300-km radius the moisture decreased linearly (see Fig. 3.1c). Each set of experiments consists of 20 ensemble members. To generate the ensembles, small amplitude random moisture perturbations are introduced; the initial field of water vapor mixing ratio below

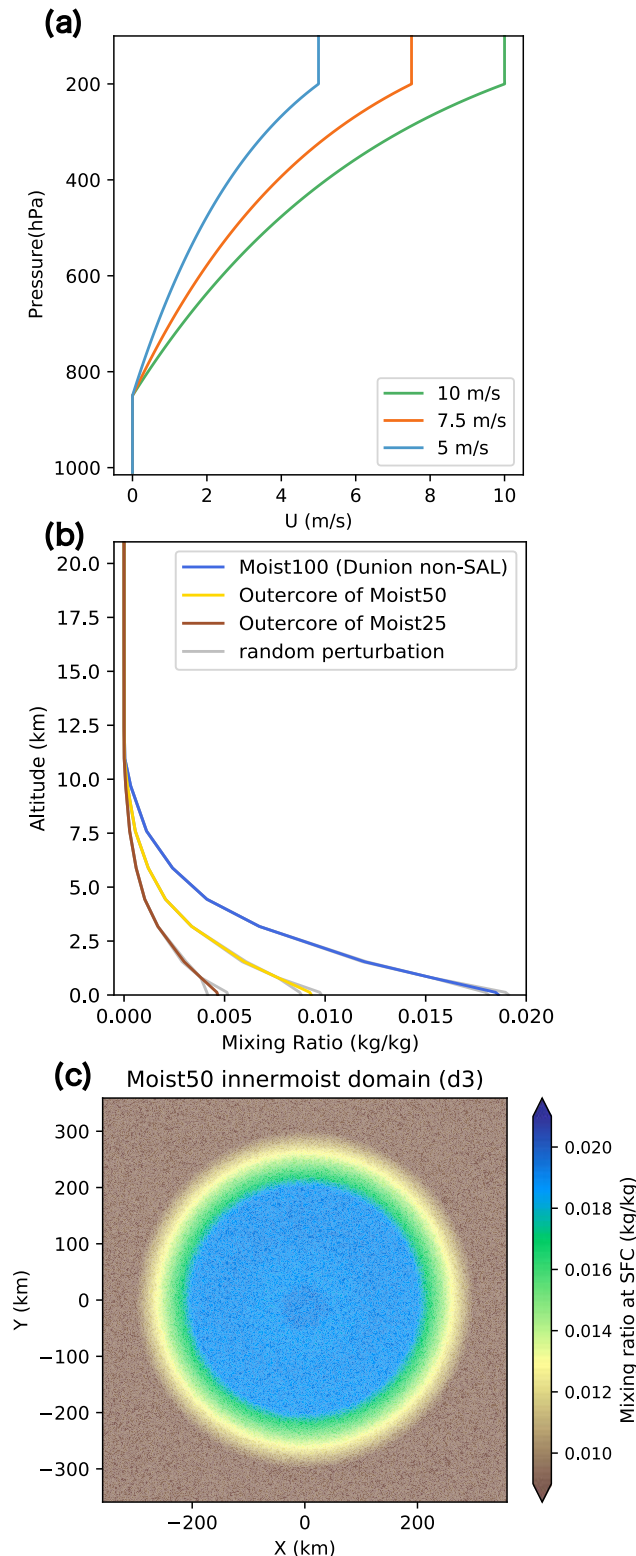


**Figure 3.1:** Vertical profiles of (a) environmental zonal wind for SH5, SH7.5 and SH10 experiments (b) water vapor mixing ratio for outer-core region ( $> 300$  km radius) for Moist100, Moist50, Moist 25; (c) Water vapor mixing ratio at the surface level from one of the Moist50 experiments.

950 hPa was perturbed with random noise between  $-0.5$  and  $0.5 \text{ g kg}^{-1}$  sampled from a uniform distribution (Zhang and Tao 2013).

For the three sets of vortex sensitivity experiments, the vortex profiles are modified as in Fig. 3. The REF set is as same as one of the Main Set, SH7.5 Moist50, but only different in that the experiments were run by a more recent version of the WRF model. The Weak sensitivity set starts with a weaker initial vortex with a maximum tangential wind of  $12.5 \text{ m s}^{-1}$  (other sets' initial maximum wind speed is  $15 \text{ m s}^{-1}$ ). The Midlevel sensitivity experiment has an initial vortex centered at 600 hPa (other sets's vortex is centered at 850 hPa). For all vortex profiles, tangential winds vanish at a 800-km radius and decay vertically following an exponential function (Moon and Nolan 2010).

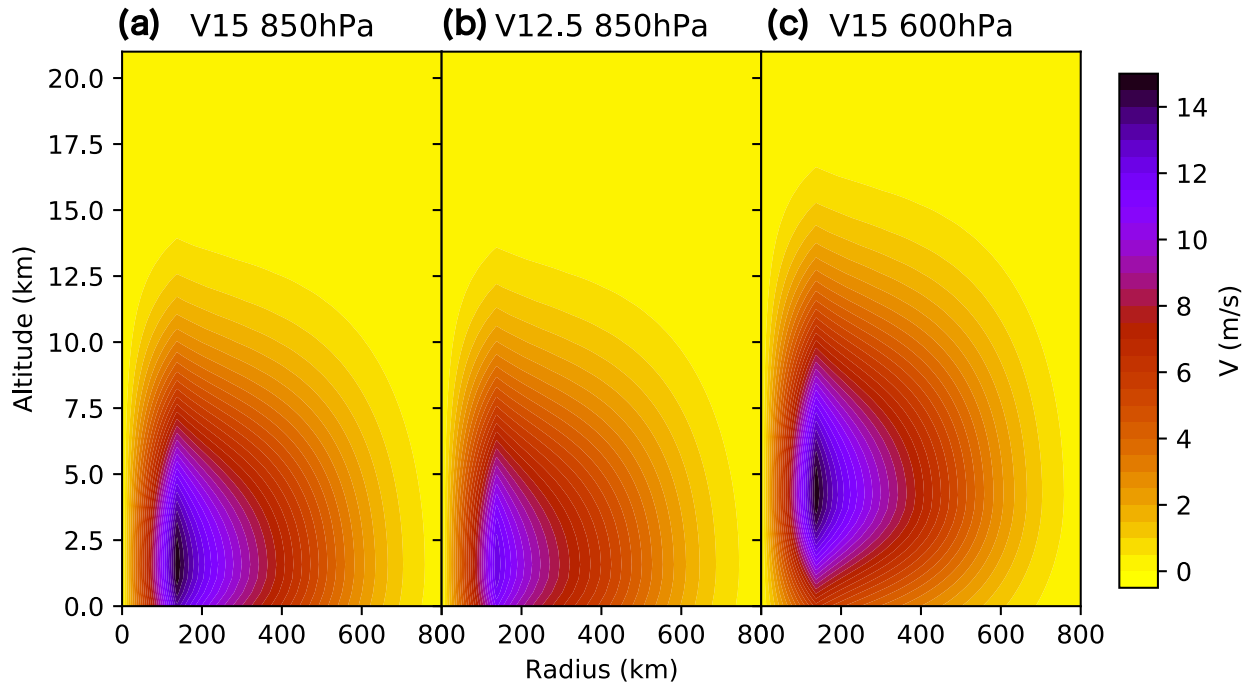


**Figure 3.2:** Cross-section of the tangential wind profiles for the sensitivity experiments from (a) REF, (b) Weak, and (c) Midlevel experiments.

### 3.3 Results

#### 3.3.1 Overview of TC development

Vertical wind shear (VWS) and dry air together have profound impacts on the evolution of the simulated tropical cyclones. Fig. 3.3 displays the time series of minimum sea level pressure (MSLP) for the 9 ensemble sets of the Main Set.

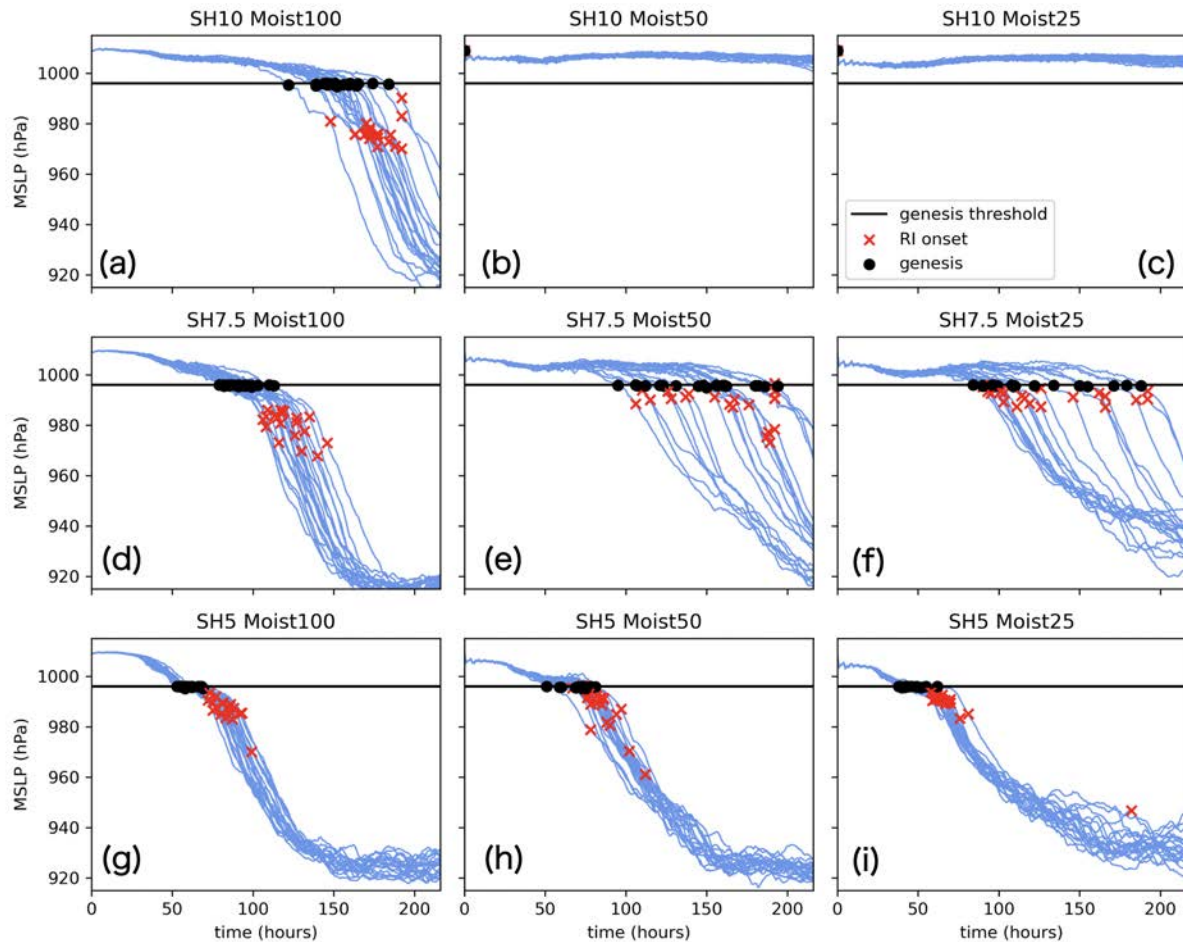


**Figure 3.3:** Timeseries of hourly minimum sea level pressure for 20 ensemble members of 9 experimental sets from the Main Set. Timings of tropical cyclogenesis and rapid intensification onset are marked with black circles and red crosses, respectively.

We decided to use MSLP rather than maximum wind speed to measure TC genesis and intensification because the central pressure deficit is an intensity measure that combines maximum

wind speed, storm size, and background rotation rate (Chavas et al. 2017), and is more stable with time than maximum wind speed. MSLP also correlates better with damage and fatalities than does maximum wind speed, and is easier to estimate (Klotzbach et al. 2020).

In Fig. 3.3, the timing of genesis and rapid intensification (RI) onset is marked. In our study, the timing of TC genesis is determined as the timing of the simulation obtaining MSLP below a threshold of 996 hPa. It can be tricky to determine the exact timing of TC genesis for a simulated tropical disturbance system. In operation, declaring TC genesis involves recognition of satellite image patterns in addition to other parameters such as SLP and maximum wind speed. In our idealized simulations, the environmental SLP (the initial SLP of the outermost domain far enough from the initial vortex) was uniform around 1009 hPa, and so 996 hPa means 13 hPa deficit of central pressure ( $\Delta P$ ) compared to the environment. The guidance of Dvorak CI-number of 2.5, which corresponds to transition from TD to tropical storm (TS), correlates with 13 hPa of  $\Delta P$  (Knaff and Zehr 2007; Courtney and Knaff 2009). The RI onset is calculated as the timing of the start of a 24-hour period of maximum SLP drop during the 9-day simulation.

For all ensembles, during the first 36 hours the simulated tropical cyclones undergo minimal SLP deepening. Substantial differences depending on VWS and environmental humidity appear after the first 36 hours. In general, the weaker VWS and the more moist, the faster ensembles develop, but among the three SH5 sets, the drier sets develop faster in the order of Moist25, Moist50 and Moist100 although the difference is not big (see Fig. 3.3 g, h, i). Most of the SH5 ensembles reach a steady-state of MSLP around hour-150 and the steady-state MSLP is lower in the moister simulations. In sum, with the small magnitude of VWS ( $5 \text{ m s}^{-1}$ ), simulated TCs develop a little faster in drier environments, but eventually those in moister environments become more intense TCs. For the strongest VWS of  $10 \text{ m s}^{-1}$ , only the ensembles with Moist100 underwent genesis during the 9 days of simulation time, and no ensembles from SH10\_Moist50 and SH10\_Moist25 reached a point of tropical cyclogenesis (Fig. 3.3 a, b, c). SH7.5\_Moist100 is right in between SH5\_Moist100 and SH10\_Moist100 in terms of genesis timing and ensemble spread (Fig. 3.3d). The largest ensemble spread was found in the drier sets of SH7.5 (Fig. 3.3 e,f). Drier environments

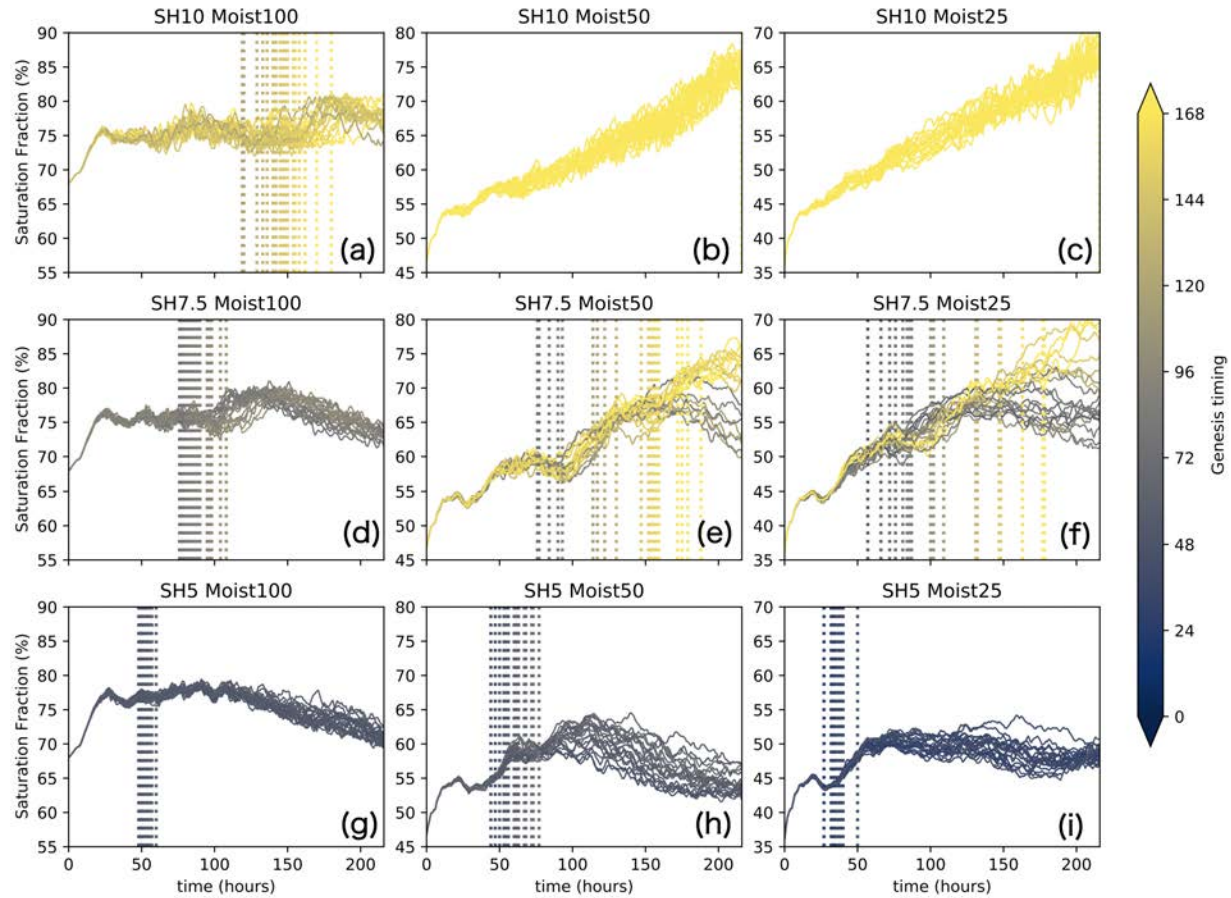
under VWS of  $10 \text{ m s}^{-1}$  and  $5 \text{ m s}^{-1}$  did not increase the uncertainty of the TC development scenarios. For SH10, it simply killed the possibility of TC development, and for SH5, the ensemble spread was still pretty narrow, not so different from Moist100 simulations. In contrast, for SH7.5, having a drier environment made the ensemble spread of SLP time series much wider, which implies a difficult forecast problem; minimal amounts of random water vapor perturbation produced completely different TC development scenarios with 99 hours discrepancy in genesis timing between the fastest developing member and slowest developing member of SH7.5\_Moist50.

Figure 3.4 displays the time series of saturation fraction averaged over the inner-moist domain ( $720 \times 720 \text{ km}$ ) for all the ensembles of the Main Set. Saturation fraction is calculated as the integrated relative humidity for vertical layers between surface to 6 km. One thing to note is that the range of y-axis is different for each column of Fig. 3.4 because Moist100 simulations have an initial domain-averaged saturation fraction of 67 % whereas Moist50 ensembles start with 47 % and Moist25 with 37 %. All the 180 ensembles show saturation fraction increasing quickly in the first 36 hours as convection in each simulation moistens the surrounding atmosphere.

A key takeaway from Fig. 3.4 is that there is no "magic" number of saturation fraction to trigger tropical cyclogenesis. The saturation fraction value at the timing of genesis varies from 45 % to 80 % depending on the shear and humidity configurations. SH10\_Moist25 and SH10\_Moist50 ensembles keep moistening the environment beyond 70 % of saturation fraction but TC genesis does not happen in any of the ensembles for these sets. Significant saturation fraction increase appears to occur after the TC genesis for most of the ensembles, which means saturation fraction increase follows TC genesis rather than leading to it.

Another interesting result is that among the Moist50 and Moist25 sets, SH5 sets have the lowest saturation fraction and SH10 sets have the highest domain average saturation fraction. It appears that simulated TCs of the SH5\_Moist50 and SH5\_Moist25 sets contain the moisture and heat energy inside the tropical cyclone and utilize it efficiently to spin up the vortex. In contrast, for the drier sets under VWS  $10 \text{ m s}^{-1}$ , moisture is spread over a larger area as it is produced by convective activities. Thus, the domain becomes more and more moist but the vortex cannot

intensify and pressure cannot deepen in the drier sets of SH10. Saturation fraction over a smaller domain of 200 x 200 km around the low-level vortex center was also examined and the overall trends were similar but it showed larger fluctuations than Fig. 3.4.



**Figure 3.4:** Time series of hourly saturation fraction for all 20 ensemble members of 9 experimental sets from the Main Set. Saturation fraction is the innermost domain averaged (720 x 720 km) for the vertical layer of 0-6 km. Both the dotted vertical line and the line color indicate the timings of tropical cyclogenesis of each ensemble member.

We looked into each ensemble member under the most uncertain set, under a moderately sheared and dry environment, SH7.5\_Moist50 to investigate how the minimal random perturbation could produce such a wide gap in timing of TC genesis. Figure 3.5 contrasts the slowest and the fastest developing members of SH7.5\_Moist50 set. In addition to MSLP, the time series of vortex tilt, inner-core convective coverage (low-level and mid-level), and average vorticity (low-

level and mid-level) are shown. We chose these variables to represent the precursor events leading into TC genesis, with vortex tilt to measure vertical realignment of the vortex tower, inner-core convective coverage to measure organized deep convection near the vortex center, and inner-core vorticity to measure a well-defined vortex (Wang 2012; Tao and Zhang 2014b, 2015; Alland et al. 2021).

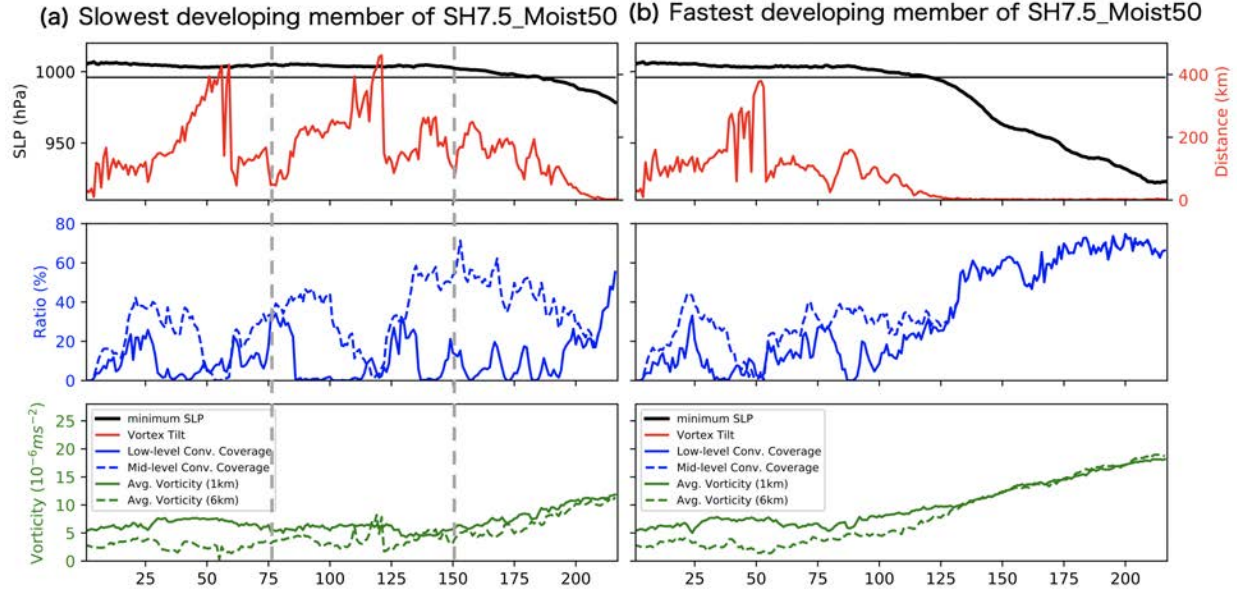


**Figure 3.5:** Time series of precursor events for (a) slowest developing ensemble member and (b) fastest developing ensemble member of SH7.5\_Moist50 experimental sets. Grey dashed lines in (a) indicates the timesteps highlighted in Figs. 3.6 and 3.7

It is necessary to explain how we calculated these variables to lay out what each variable stands for. First, vortex tilt is the distance between 0-km and 6-km vortex centers. Vortex centers are detected as the location of minimum pressure at each vertical level with the pressure field smoothed with a Gaussian filter (e.g. red and white 'x' in Fig. 3.6 a, c). Second, convective coverage indicates the portion of area inside the inner-core region ( $200 \times 200$  km box around the vortex center) is covered by convection. We used 20 dBZ at 6-km altitude as the threshold to indicate a convective grid cell. The low-level convective coverage indicates the convective coverage of the  $200 \times 200$  km box around the vortex center at 1 km, and the mid-level convective

coverage is for the 200 x 200 km box around the vortex center at 6 km (e.g. panel b, d of Figs. 3.6 and 3.7). Thus, the low-level and mid-level boxes and convective coverage will be identical if the vortex tilt is zero. Lastly, the average vorticity is the arithmetic mean of the relative vertical vorticity inside the 200 x 200 km domain surrounding the vortex center at the respective altitudes of 1 and 6 km.

Comparing the two panels of Fig.3.5 through the first 90 hours, the two ensemble members exhibit a similar trend. There is the repetition of vortex tilt increase and decrease with changing convective coverage. For the slowest developing member, multiple cycles (8 cycles when counting each distinctive low-level convective burst) occurred before genesis, whereas the fastest developing member reached tropical cyclogenesis after going through 2 cycles.

The first cycle spans about 48 hours for both members. Initially, convective coverage increases in the inner-core region in the first 36 hours. As the vortex tilt increases while the mid-level vortex is shifted eastward by westerly VWS, there emerges a discrepancy between low-level and mid-level convective coverage. Low-level convective coverage decreases as tilt increases, but mid-level convective coverage continues for a longer time.

The second cycle starts around hour-55 for both members, with convective coverage starting to increase again and then around hour-60 vortex tilt drastically decreases from 400 km to below 50 km. Similar to the first cycle, as tilt increases again, low-level convective coverage decreases around hour-85. The bifurcation point between these two members appears to be around hour-90: the slowest member's tilt keeps increasing but the fastest member's tilt starts to diminish again. As tilt approaches zero (mid-level and low-level vortices perfectly aligned), the fastest developing member quickly passes the genesis phase and enters the rapid intensification phase. The slowest developing member takes more cycles of tilt decreasing and multiple low-level convective coverage bursts until it finally has a tropical depression inside its domain.

The average vorticity lines show a very similar monotonic increasing trend same as the monotonic decreasing trend of SLP. It looks like the mid-level vorticity starts to increase a few hours earlier than the low-level vorticity. In Fig.3.5b, the mid-level vorticity starts to pick up earlier and

increases faster than the low-level vorticity, they reach a similar magnitude of vorticity in about 24 hours.

To further investigate why the cycles of tilt decreasing and convective coverage increasing in earlier hours for the slowest developing member were not successful in intensifying the system, we examined the hourly pressure and reflectivity fields of the slowest developing member. Figures 3.6 and 3.7 show the snapshots of the simulated TC of the slowest ensemble member of SH7.5\_Moist50 at hour-75 and hour-150, respectively (grey dashed lines in Fig. 3.5a). These time steps are peaks of the 2nd and 4th cycles of the slowest developing member's precursor events lining up together. Vortex tilt is in similar magnitude of 101 and 103 km, and the mid-level vortex is located at northeast and east to the low-level vortex for hour-75 and hour-150 as expected with the westerly VWS. A noticeable difference is that the mid-level vortex in hour-150 has a larger cyclonic circulation (see streamlines of Figs. 3.6a and 3.7a); the mid-level wind pattern is westerly laminar flow at the southern portion in hour-75, which is the initially prescribed environmental flow, but in hour-150 the mid-level wind is dominantly cyclonic. Figures 3.6b, d and 3.7b, d show deep convection near the low-level and mid-level vortex centers (red x and white x, respectively). Mid-level convective coverage is always larger than low-level convective coverage in this case (Fig. 3.5) because the mid-level vortex center is collocated inside the deep convection. Looking at every hourly output of reflectivity, pressure, and vorticity fields at the mid-level (not shown), we confirmed that after the pre-existing mid-level vortex is shifted away by the VWS, a new smaller scale (meso-beta scale) mid-level vortex forms at the same location of the deepest convection at that timing, likely through vortex stretching by the deep convection.

The findings to highlight from Figs. 3.5, 3.6, and 3.7 are:

- The fastest developing member and the slowest developing member have very similar trends of precursor events until the 90-hour mark.
- The slowest developing member has multiple cycles of precursor events lining up together that could possibly lead to TC genesis but they all failed until the 8th attempt.

### Hour-75 of the slowest SH7.5\_RH50

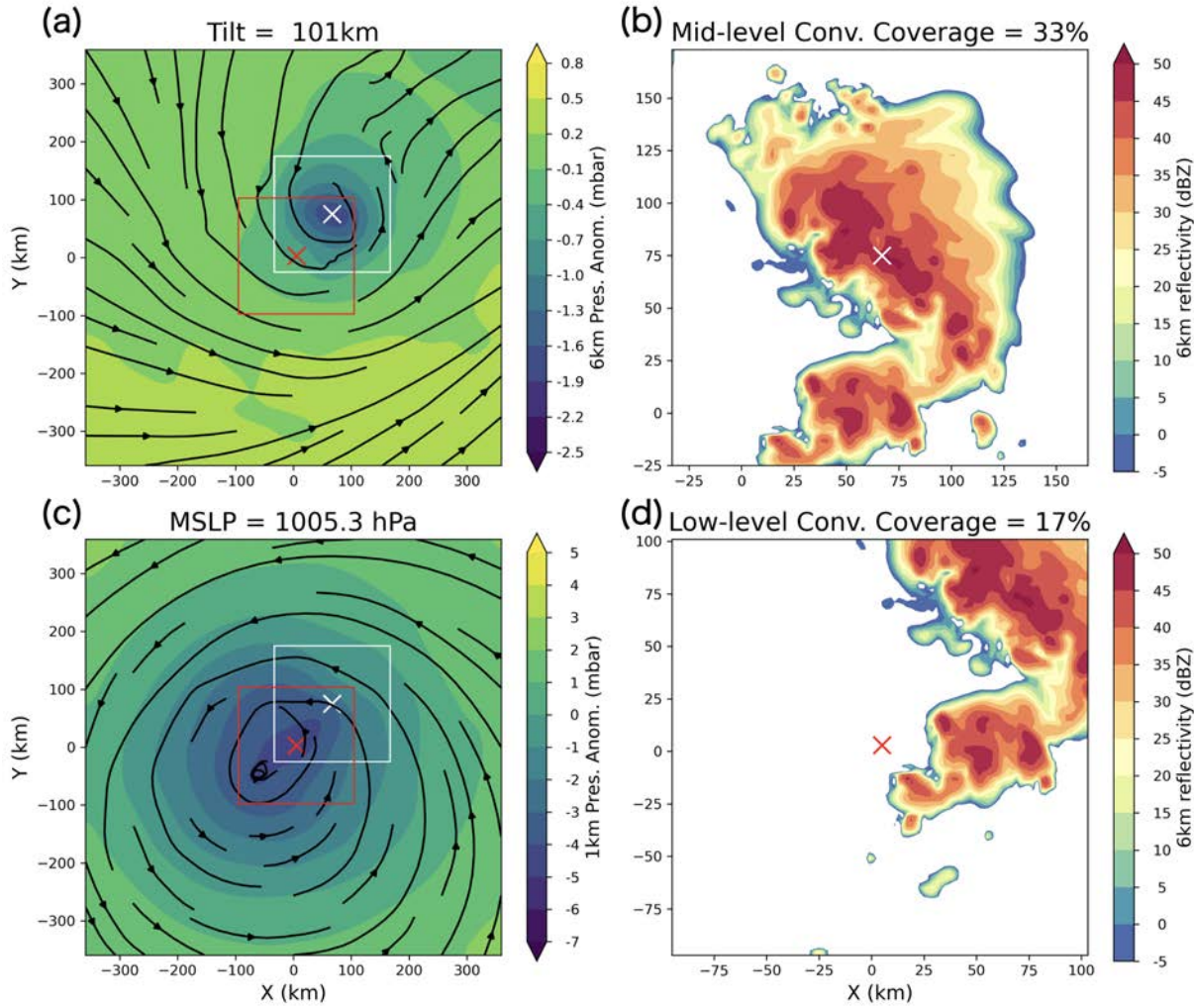


**Figure 3.6:** Snapshot of simulated TC from the slowest developing member of SH7.5\_Moist50 at hour-75 (Fig.3.5a). Pressure anomaly and the streamlines at altitude of (a) 6 km, (c) 1 km, simulated reflectivity at 6km inside 200 x 200 km box around the center of (b) mid-level vortex center, (d) low-level vortex center. Red and white 'x' indicate the vortex center at 1 km and 6 km altitude, respectively. The 200 x 2000 km red and white boxes in (a), (c) are centered on the vortex center at 1 km and 6 km. The white box is zoomed in as the domain of panel (b), and the red box corresponds to the domain of panel (d).

### Hour-150 of the slowest SH7.5\_RH50

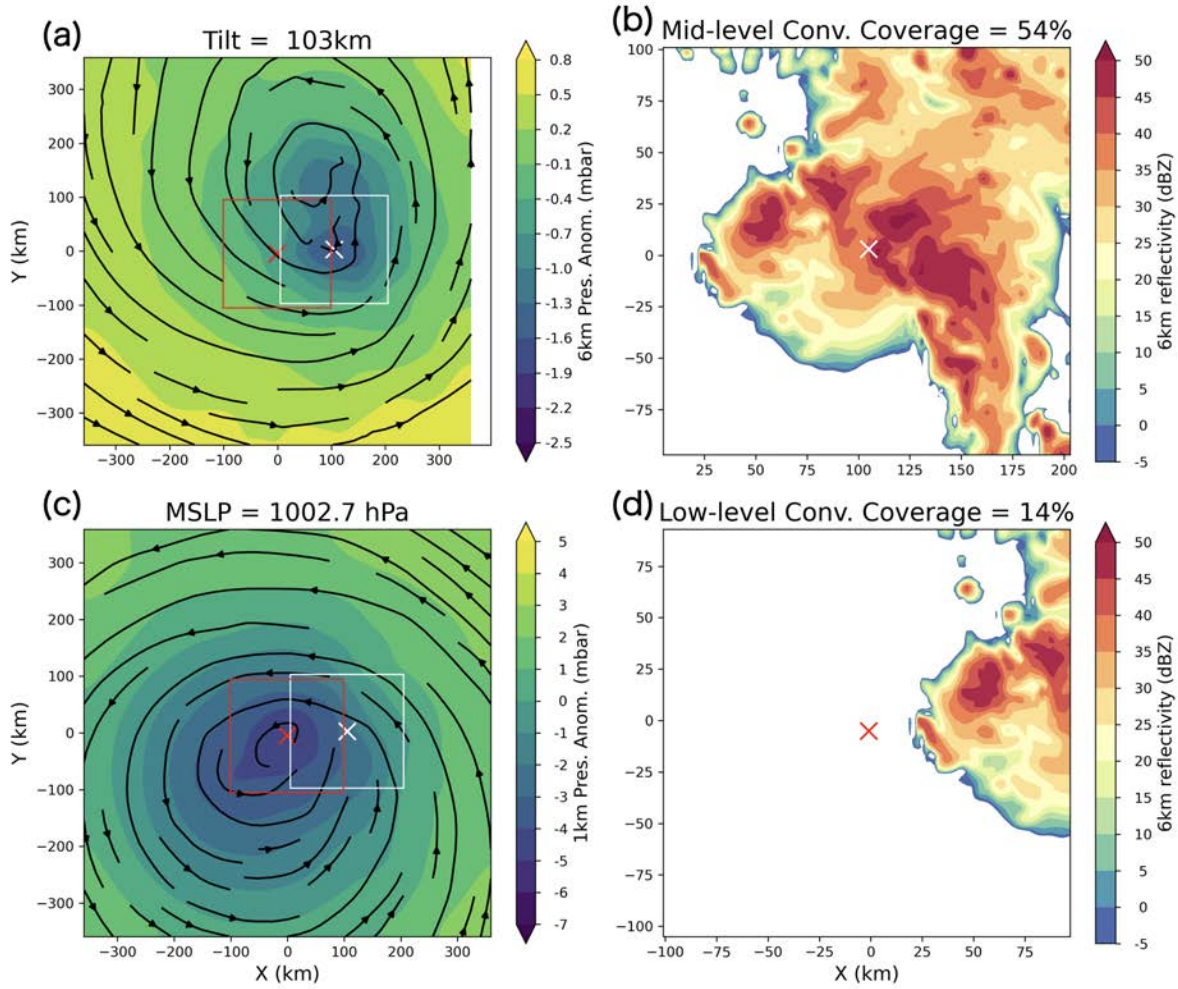


**Figure 3.7:** Snapshot of simulated TC from the slowest developing member of SH7.5\_Moist50 at hour-150 (Fig.3.5 a). Panel information is the same as Fig. 3.6.

- SLP starts to drop rapidly, only after vortex tilt decreases.
- Low-level convective coverage is more episodic compared to mid-level convective coverage, and mid-level convective coverage persists for a longer time after tilt increases again.
- Mid-level vorticity shows hints of increase slightly sooner than low-level vorticity and SLP.
- Deep convection over a wider area inside the inner-core region generates a smaller-scale mid-level vortex, which results in instantaneous vortex tilt decrease.
- A key difference between the successful and failed precursor cycles in SH7.5\_Moist50 ensembles is whether the newly generated mid-level vortex stays aligned with the low-level vortex or it is shifted away by the VWS again.

### 3.3.2 Probabilistic approach to TC genesis

To sum up what we found in Section 3.3.1, among all the configuration of VWS and dry environments setups the combination of moderate shear and dry humidity (SH7.5\_Moist50) produced the widest ensemble spread, hence the most uncertain scenario for TC genesis. The ensemble members went through similar cycles of precursors before TC genesis with deep convection emerging inside the circulation, a new meso-beta mid-level vortex forming up, and as a result, vortex tilt decreasing. One difference between fastest and slowest developing members was how many cycles of these episodes they go through to have a successful TC genesis.

Then, the question is whether there exist physical differences between the successful and unsuccessful cycles of these precursor episodes or not. Due to the stochastic characteristic of convective initiation and complicated multi-scale interactions between convection and the sheared environment (as shown in chapter 2), it is possible that TC genesis in a marginally favorable environment with moderate vertical wind shear and moderately dry atmosphere is intrinsically unpredictable in deterministic sense. Therefore, we decided to take a probabilistic approach to TC genesis by counting how many trials of precursor events were required to achieve TC genesis in each ensemble member. The statistical model we emulate is the geometric distribution, which is

the probability distribution of the number of Bernoulli trials needed to get one success. A famous example would be how many trials of coin flipping are required to get the tail side of the coin. In our case, each Bernoulli trial will be a precursor event such as tilt decreasing below a certain threshold, and the success is TC genesis (i.e., MSLP reaching 996 hPa). We note that each precursor event cannot be purely independent from each other; the vorticity or moisture produced by previous convective bursts sets up the environment for the following convective bursts. The slowest developing member of SH7.5\_Moist50 had a larger mid-level circulation and a lower SLP to begin with at its fourth cycle compared to the second cycle (Figs. 3.6, and 3.7).

We set the threshold of each precursor as the mean value of the variable at the genesis timing for all 140 developing members (except for 40 members of SH10\_Moist50 and SH10\_Moist25). For example, as shown in Fig. 3.8, the threshold of the precursor of low-level convective coverage increase is 14 %. It does not mean that having low-level convective coverage larger than the threshold of 14 % guarantees TC genesis given the spread of data points of convective coverage. However, the threshold is a tool to count the distinctive episodes such as convective bursts shown in Fig. 3.5.

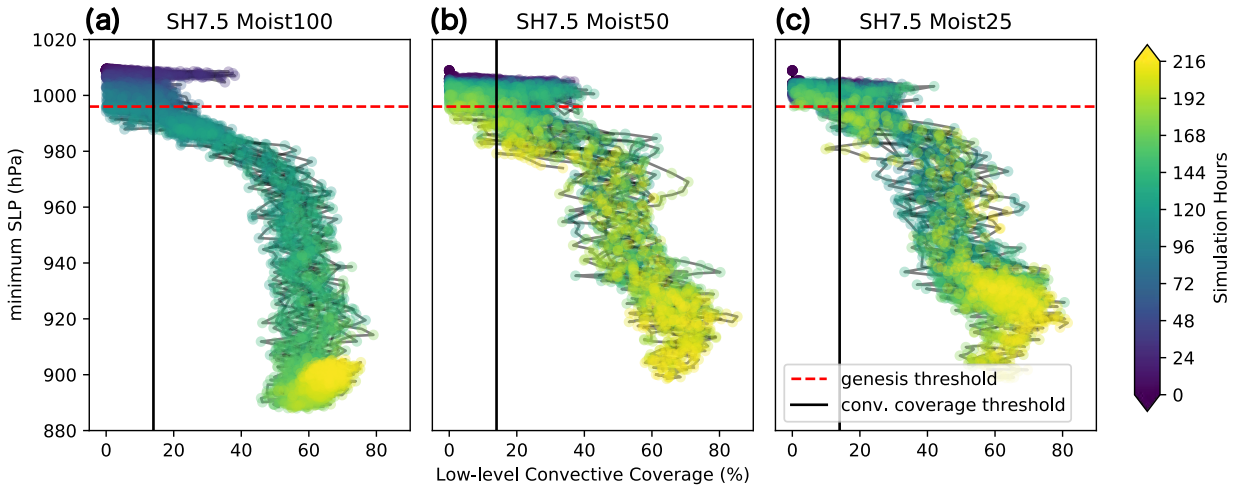


**Figure 3.8:** Low-level convective coverage as a function of minimum sea level pressure decrease with color denoting the simulation time for SH7.5 simulations. Low-level convective coverage threshold is 14%, which is an average value of low-level convective coverage for all developing members in the Main Set.

Figure 3.9 shows the number of precursor events before TC genesis. The thresholds for the four precursors of vortex tilt magnitude, inner-core average mid-level vorticity, inner-core low-level convective coverage, and inner-core mid-level coverage are 82.0 km,  $6 \times 10^{-6} \text{ m s}^{-2}$ , 14.0 %, and 37.0 %, respectively. We count it as a precursor event when the variable reached the threshold and kept the value above the threshold for at least 3 hours (vortex tilt decreasing below the threshold and the three other variables increasing above the thresholds).

A key takeaway from Fig. 3.9 is that the marginally favorable environments of SH7.5\_Moist50 and SH7.5\_Moist25 have the most attempts of precursor events (up to 7 times) among all the setups. The simulated TCs under SH5 setups do not require as many attempts to reach the point of TC genesis. In terms of mid-level vorticity increase and low-level and mid-level convective coverage increase, SH5 sets have the most narrow distribution with a peak of 1-2 attempts (blue in Fig. 3.9 c,e, and g). The only exception is vortex tilt, where SH10 sets have the smallest number of events of vortex tilt decreasing below 82 km. This is because most of the 20 ensemble members that develop despite the strong VWS (all from SH10\_Moist100) reach 996 hPa SLP with vortex tilt larger than the threshold. Among SH7.5 sets, it is the drier setups that have the widest spread of the number of precursor events that is required to reach TC genesis. Similar to SH10\_Moist100, a majority of SH7.5\_Moist100 ensemble members reach the point of TC genesis with mid-level and low-level vortex misaligned by farther than 82 km (Fig. 3.9 b). Moist100 provides a very favorable thermodynamic setup of sea surface temperatures of 29°C and moist Dunion sounding, thus it is likely that simulated TCs under Moist100 can afford a larger magnitude of vortex tilt. Moist50 and Moist25, on the other hand, have a region of drier air in the outer-core region that can easily be brought into the inner-core region through radial ventilation if the vortex tower is tilted by a lot. Mid-level vorticity, in general, has smaller numbers of attempts compared to the other variables because averaged vorticity increases more gradually than episodically (c.f. Fig. 3.5).

Figure 3.10 displays the timing of the four precursor events against the timing of TC genesis for each ensemble member of the Main Set. Vortex tilt decrease and convective coverage increase exhibit a repeated cycle with a period of 36-48 hours. An initial convective burst or vortex re-

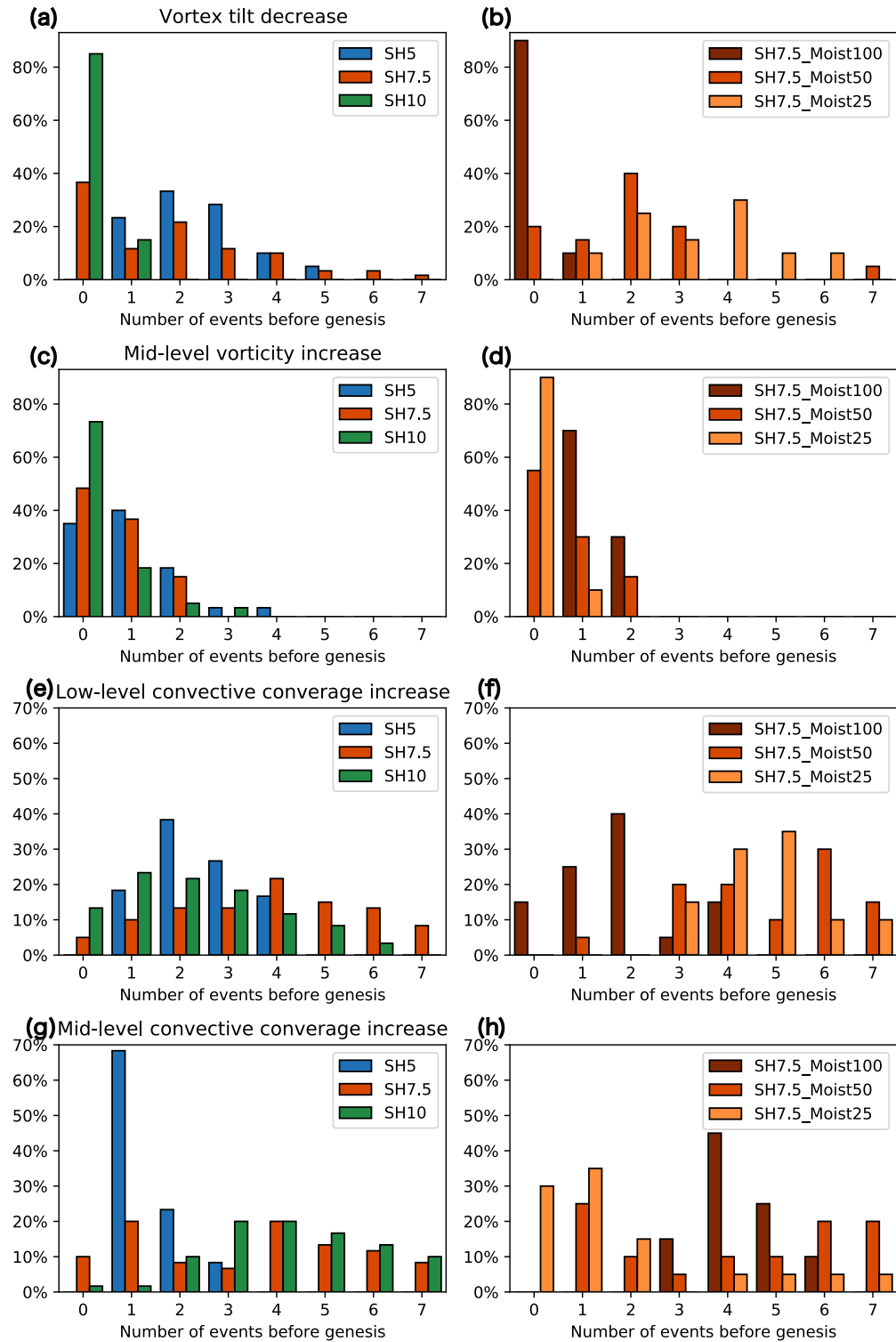


**Figure 3.9:** Histograms of the number of TC genesis precursor events occurring before the timing of genesis. Histograms of (a), (c), (g), and (e) are composed by shear magnitude. Histograms of (b), (d), (f), and (h) are for SH7.5 simulations only, and composed by environmental moisture magnitude.

alignment occurs in the first 24 hours and the second cluster of bursts occurs between hour 50-75 then the following episodes occur between 100-175 hour (if TC genesis did not happen until that point of timing). The timing of mid-level vorticity increase almost coincides with the timing of genesis, only a few hours earlier. As discussed above, for vortex tilt no data points of SH7.5\_Moist100 and SH10\_Moist100 are evident as these ensembles reach TC genesis with vortex tilt larger than 82 km. The precursor event that has the longest lead time before TC genesis appears to be mid-level convective coverage increase, especially for SH7.5\_Moist50 and SH7.5\_Moist25, which are the ensemble sets that have the widest ensemble spread. On average, the latest mid-level convective coverage increasing beyond 37 % happens 31.4 and 34.4 hours before the timing of TC genesis for SH7.5\_Moist50 and SH7.5\_Moist25, respectively. However, the latest low-level convective coverage increasing beyond 14 % happens 15.6 and 8.7 hours earlier than the timing of TC genesis for SH7.5\_Moist50 and SH7.5\_Moist25, respectively. It is consistent with Fig. 3.5 that showed mid-level convective coverage has more persistence than low-level convective coverage.

### 3.3.3 Time-lagged correlation analysis

The different distribution of the timing of each precursor event before the timing of genesis (Fig. 3.10) warranted a further investigation of causality between each physical process that is represented by the precursor variables and TC genesis. Here we present time-lagged cross-correlation analysis results. Time-lagged cross-correlation refers to the correlation between two time series shifted relatively in time. Each time series was detrended first (Shen 2015).

Figure 3.11 shows time-lagged correlations between the time series of 217 hours of hourly MSLP and the precursor variables (vortex tilt, mid-level inner-core average vorticity, and low- and mid-level inner-core convective coverage) of the 20 ensembles of SH7.5\_Moist50. Vortex tilt should have a positive correlation with MSLP for tilt decreases as MSLP decreases. Vorticity and convective coverage should have a negative correlation with MSLP for they increase as MSLP drops. Shifting the time series hour by hour, we can find a time-lag that records a maximum (vortex tilt) or minimum (vorticity and convective coverage) correlation (red dotted lines in Fig. 3.11). The red solid line denotes the mean time-lag from 16 ensembles of SH7.5\_Moist50. Four ensembles

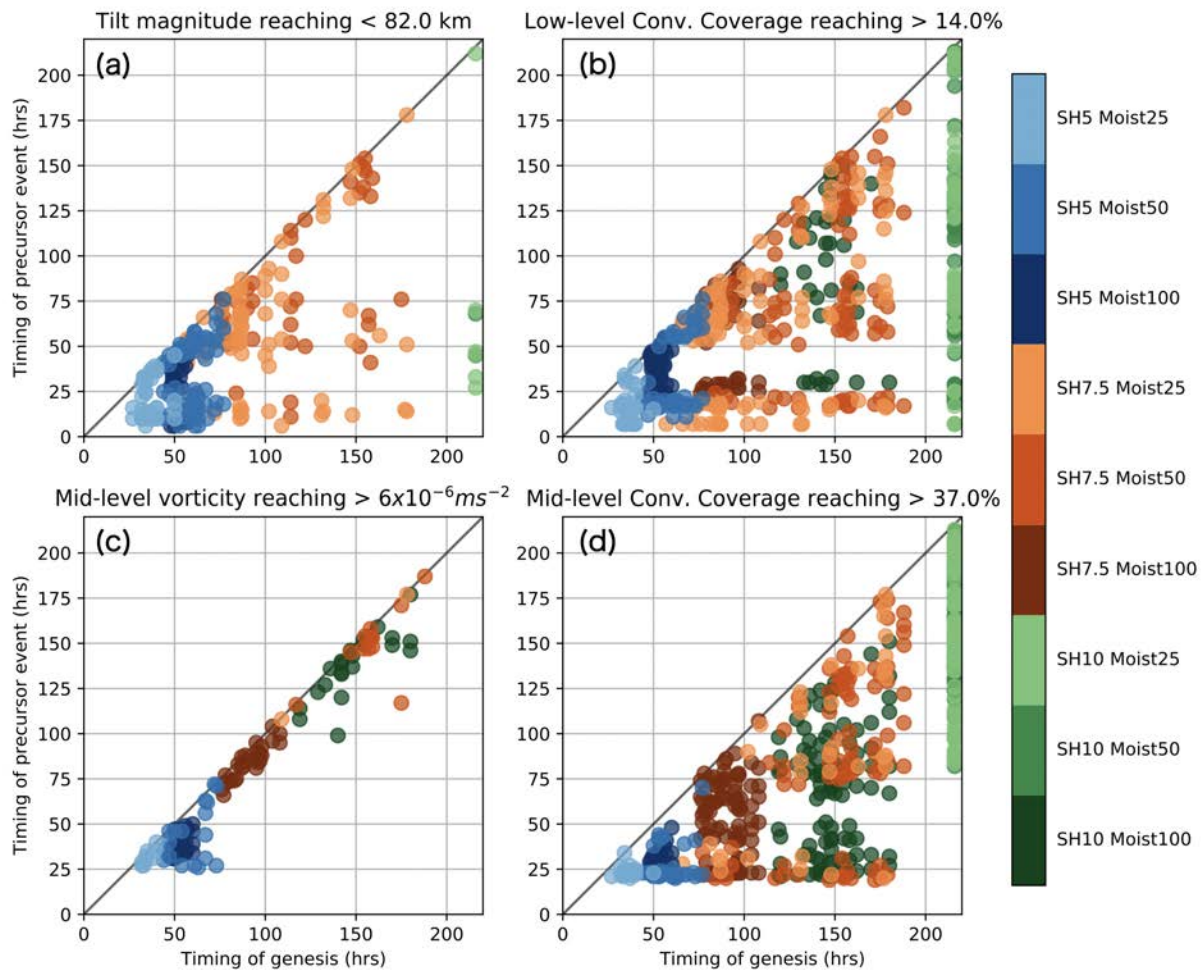


**Figure 3.10:** Timing of the TC genesis precursor events compared to timing of genesis. Each event is counted with the precursor parameter keeping its value below or beyond the threshold for 3 hours continuously.

that have TC genesis after hour-168 were excluded to ensure at least 48 hours offset from the end of simulation hours (grey lines in Fig. 3.11).

Positive time lag means the time series of the precursor variable leads the time series of MSLP, which implies predictability for TC genesis. Among the four precursor variables, mid-level convective coverage has the longest mean lead time (around 36 hours). However, mid-level convective coverage has a larger variance from ensemble to ensemble compared to the other three variables, which could be interpreted as a less reliable predictor. The reason why time-lag of mid-level convective coverage and MSLP has a large deviation is because the time-lagged correlations between mid-level convective coverage and MSLP (Fig. 3.11 d) has a wave-like pattern with multiple peaks and troughs, unlike the other variables that have a single peak (vortex tilt) or a single trough (mid-level vorticity and low-level convective coverage). There are largely two distinctive troughs at around 12-hour and 72-hour of lead time. Among the four variables in Fig. 3.11, the mid-level vorticity has the best correlation and the narrowest spread of the time-lag for SH7.5\_Moist50 ensembles, but it has a smaller mean lead time of 12 hours.

The wavy pattern of cross-correlations between mid-level convective coverage and SLP is found not only from SH7.5\_Moist50 ensembles, but also from other Main Set ensembles (Fig. 3.12). The wavy pattern is thought to be related to multiple incidences of convective coverage increase and decrease as shown in Fig. 3.5. Comparing the 3x3 panels in Fig. 3.12, there is a trend that the ensembles from more favorable setups (e.g. SH5\_Moist100) have a longer lead time of the mid-level convective coverage, better correlation, and a narrower ensemble spread. On the contrary, the ensembles that had the widest spread in SLP (i.e., SH7.5\_Moist50 and SH7.5\_Moist25) also exhibit large ensemble spread in time-lag distributions.

Figure 3.13 summarizes the results of time-lagged cross correlation analysis for all the four precursor variables in one plot. The ensemble-mean time lag is on the y-axis, and standard deviation of the time-lags is on the x-axis, such that the upper-left corner denotes the best predictor for TC genesis with a long lead time and good confidence. The marker size is proportional to the ensemble mean time-lagged correlation value. Some ensemble members of SH10\_Moist100 did

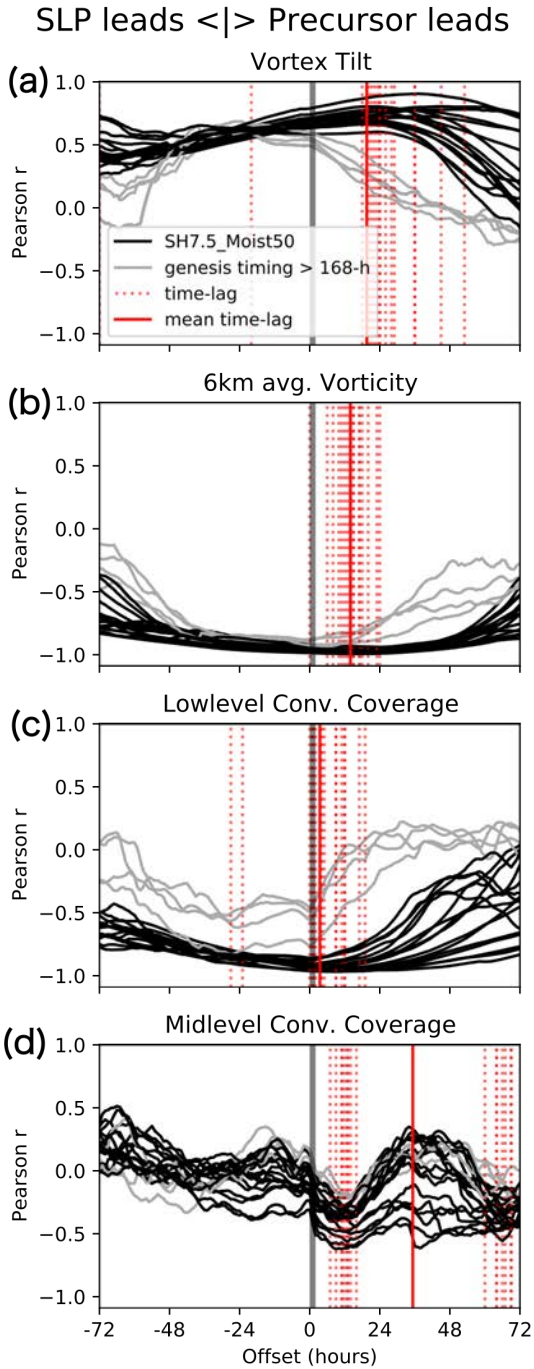


**Figure 3.11:** Time-lagged Pearson correlations between time series of minimum sea level pressure (SLP) and (a) vortex tilt, (b) mid-level vorticity, (c) low-level convective coverage, (d) mid-level convective coverage for the SH7.5\_Moist50 experimental set. Red dotted vertical lines indicate the time-lag of maximum/minimum correlation for each ensemble member, and red solid lines indicate the mean time-lag for the ensembles with genesis timing  $\leq$  168-hour. Positive time-lag means each precursor event happens before SLP drops and vice versa.

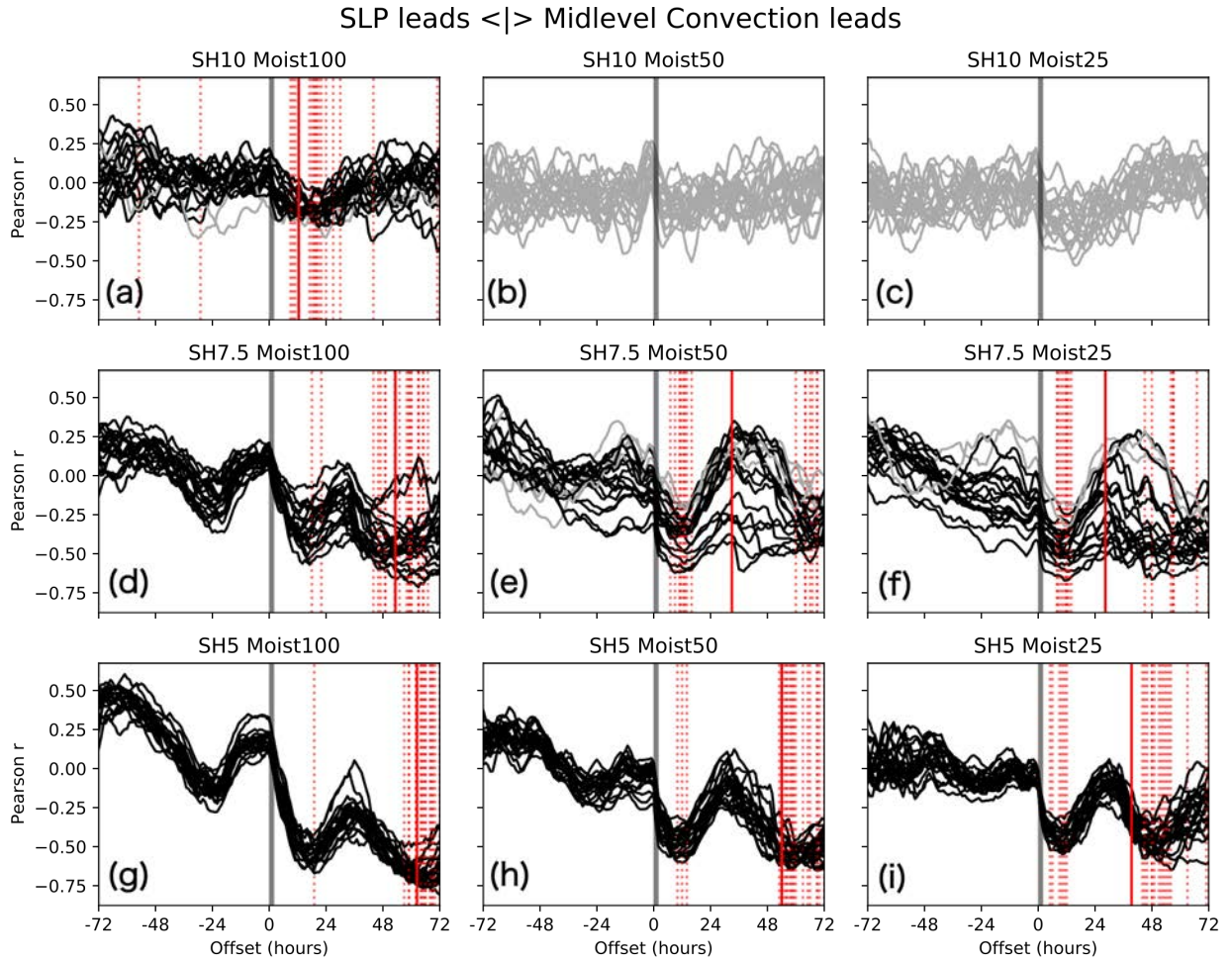


**Figure 3.12:** Time-lag Pearson correlation between time series of minimum sea level pressure (SLP) and mid-level convective coverage as a function of time-lag for the whole main set experiments. Annotation is the same as Fig. 3.11.

not have a statistically significant correlation between mid-level convective coverage and MSLP in 95 % confidence level based on a two-sided Student's t-test, thus it is marked with 'x' instead of 'o' (Figs. 3.12 a and 3.13 d). As shown in Fig. 3.12, the more favorable setups (smaller VWS and moister environments) have metrics with longer lead time, less spread, and better correlations with MSLP evolution, in general. Among the four variables of precursor events, the order of mean lead time is 1) mid-level convective coverage, 2) vortex tilt, and 3) low-level convective coverage and mid-level vorticity at a similar timing. The longer lead time, the smaller correlation, and the larger standard deviation of the mid-level convective coverage with MSLP implies that mid-level convective coverage increasing (that usually happens 48 hours before TC genesis) does not always end up with TC genesis. Higher correlation and smaller ensemble spread of mid-level vorticity means that mid-level vorticity increasing (that usually happens 12 hours before TC genesis) has a better chance to result in TC genesis soon, compared to mid-level convective coverage increasing. The time order of each precursor event and the probability of each precursor event eventually leading into TC genesis is further discussed in section 3.4.

### 3.3.4 Sensitivity to vortex structure

We explore how our findings of physical processes leading to TC genesis in sheared and dry environments are sensitive to the initial vortex intensity and depth. For the sensitivity experiments, we used a more recent WRF version of 3.9. To confirm that the results are consistent with WRF3.1.1, we ran 20 ensembles with the exact same configurations with SH7.5\_Moist50 of the Main Set (REF). The SLP evolution of REF comes close to that of SH7.5\_Moist50 with a little narrower ensemble spread and earlier genesis timing (Fig. 3.14 a). The Midlevel experiment is the same as REF except for having a mid-level centered initial vortex (600-hPa vs. 850-hPa). The Midlevel sensitivity tests are designed to mimic pre-depression systems originating from African easterly waves or extratropical disturbances. The change of vortex center from 850-hPa to 600-hPa apparently made the TC more vulnerable to VWS, so the tropical cyclogenesis was delayed or completely thwarted (Fig. 3.14 b). Also, the ensemble spread of the Midlevel set is very wide, with TC genesis timing ranging from early as hour-130 to later than hour-216. Changing initial

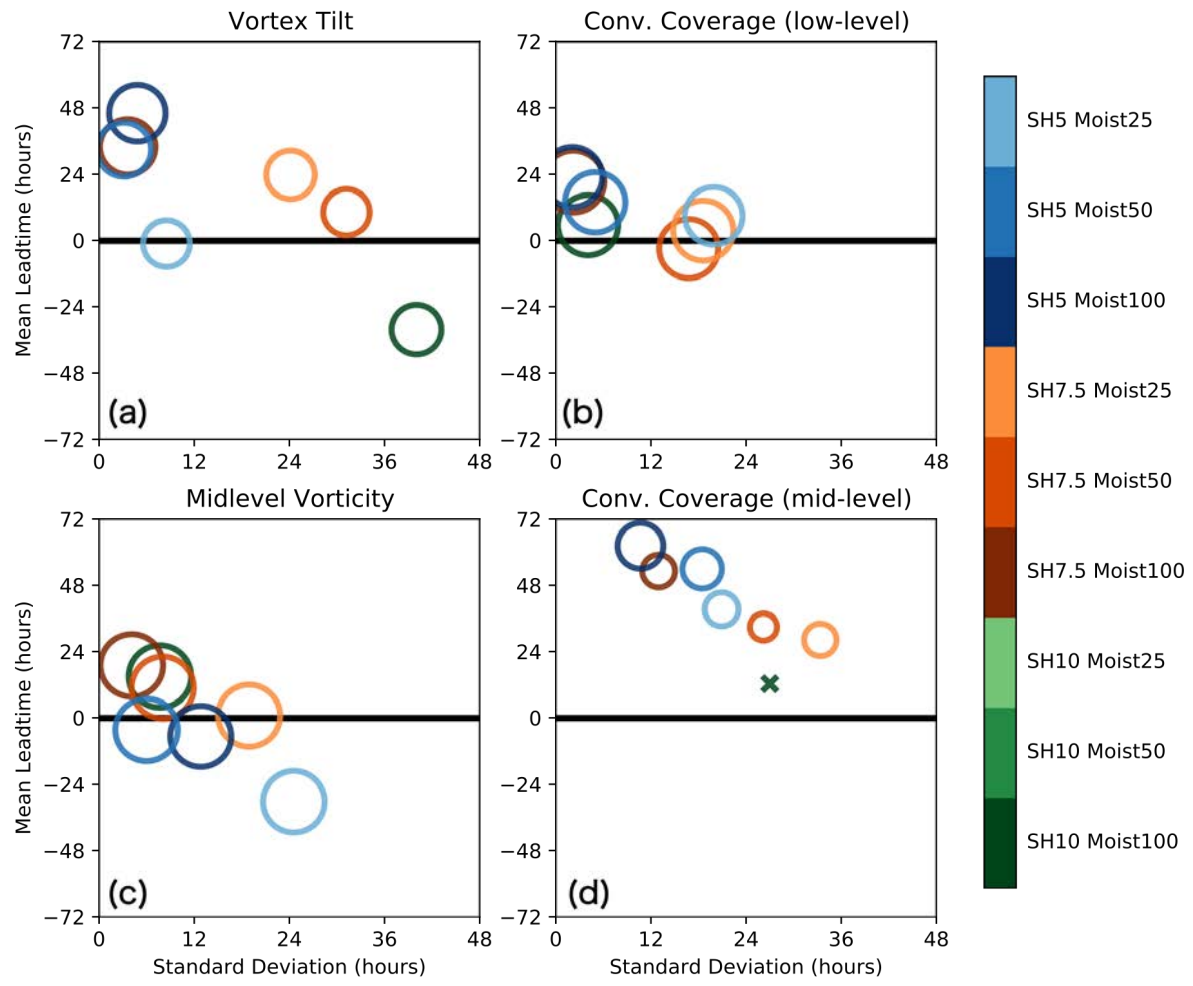


**Figure 3.13:** Time-lag correlation analysis results for the time series of minimum sea level pressure (MSLP) and each of the four precursor variables with mean of time-lag for y-axis and standard deviation of the time-lag of 20 ensemble members in x-axis. The size of the circle is proportional to the mean correlation between two time series at the time-lag. The combination that had correlation not significant at 95% level is marked with ‘x’ rather than a circle. The ensemble sets that do not have any developing members are not shown.

vortex intensity from  $15 \text{ m s}^{-1}$  to  $12.5 \text{ m s}^{-1}$  (the Weak Set) also made the vortex more vulnerable. When we tested the  $12.5 \text{ m s}^{-1}$  vortex with a  $7.5 \text{ m s}^{-1}$  VWS and Moist50 setup, none were developing (just like SH10\_Moist25), so we put Weak set under the most favorable environment of the Main Set, which is SH5\_Moist100. Then interestingly, the SLP evolution bears the widest ensemble spread, with TC genesis timing ranging from hour-100 to later than hour-216 (Fig. 3.14 c). The resilience of a TC-like vortex to a sheared and dry environment is shown to be sensitive to the intensity and vertical structure of the initial vortex.

Similar to Fig. 3.5, the slowest and the fastest developing members of the Midlevel and the Weak sensitivity experiments are contrasted in Figs. 3.15 and 3.16, respectively, in terms of the time series of MSLP, vortex tilt, low-level and mid-level convective coverage, and low-level and mid-level vorticity. The fastest developing members share the same trends: mid-level convective coverage increasing first, then vortex tilt decreasing, and low-level convective coverage increasing (see panel b of Figs. 3.5, 3.15, 3.16). One difference for the Weak Set is that mid-level vorticity picks up faster than other experimental sets (green dashed line in Fig. 3.16 b). However, the slowest developing members have different trends. The slowest member of SH7.5\_Moist50 showed multiple cycles of vortex tilt decreasing below the threshold before TC genesis, but the slowest members of Midlevel and Weak sets have the vortex tilt steadily increasing. For convective coverage, there is no appreciable low-level convective coverage increase beyond the threshold during 216 hours for the slowest member of the Midlevel and Weak sets, unlike SH7.5\_Moist50. The slowest member of the Weak Set has a wide mid-level convective coverage, and the slowest member of the Midlevel set also has some bursts of mid-level convective coverage increasing, but it was not followed by tilt decreasing nor low-level convective coverage increasing.

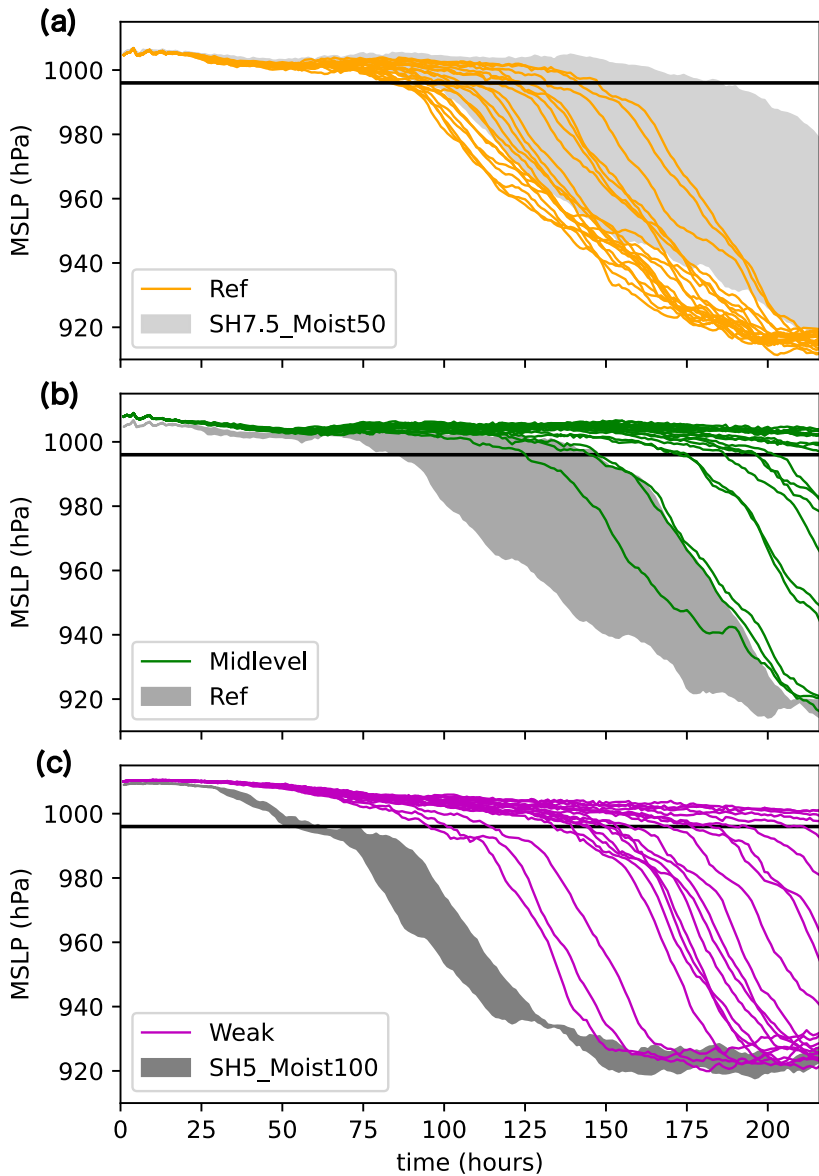


**Figure 3.14:** Time series of minimum sea level pressure deepening for 20 ensemble members of sensitivity simulations of (a) REF, (b) Midlevel, (c) Weak. REF is the same as SH7.5\_Moist50 except that it's run by WRF3.9 instead of WRF3.1.1. Midlevel is the same as REF except that the initial vortex is centered at 600-hPa instead of 850-hPa. Weak set is the same as SH5\_Moist100 but its initial vortex has maximum wind speed of  $12.5 \text{ m s}^{-1}$  instead of  $15 \text{ m s}^{-1}$  and it is run by WRF3.9 instead of WRF3.1.1.

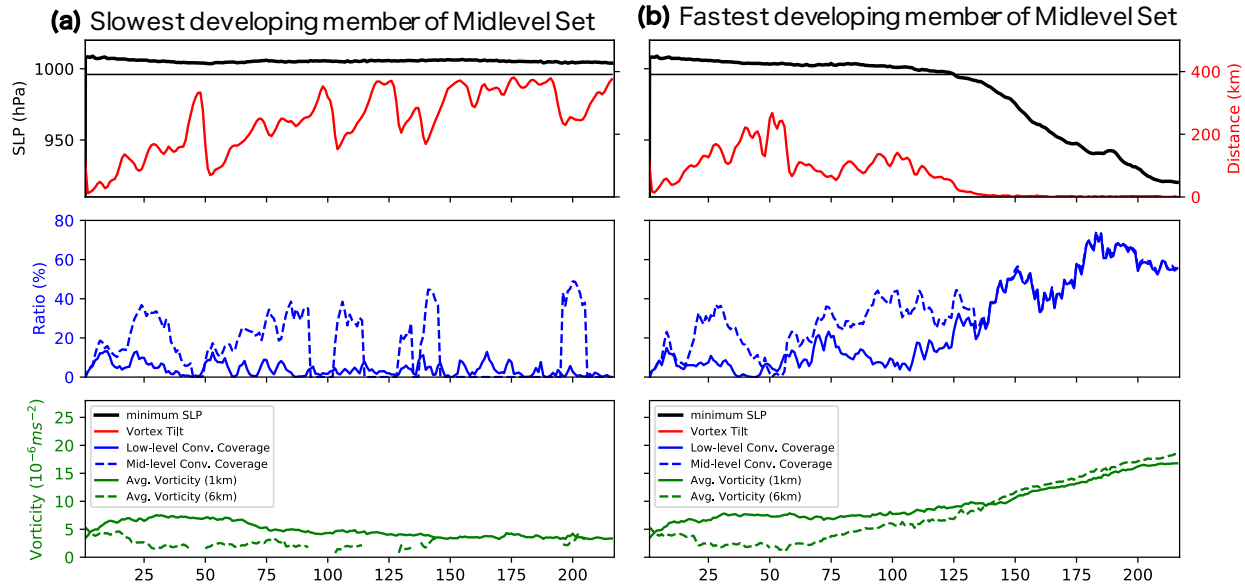


**Figure 3.15:** Time series of precursor events for **(a)** slowest developing ensemble member and **(b)** fastest developing ensemble member of the Midlevel sensitivity experimental set.

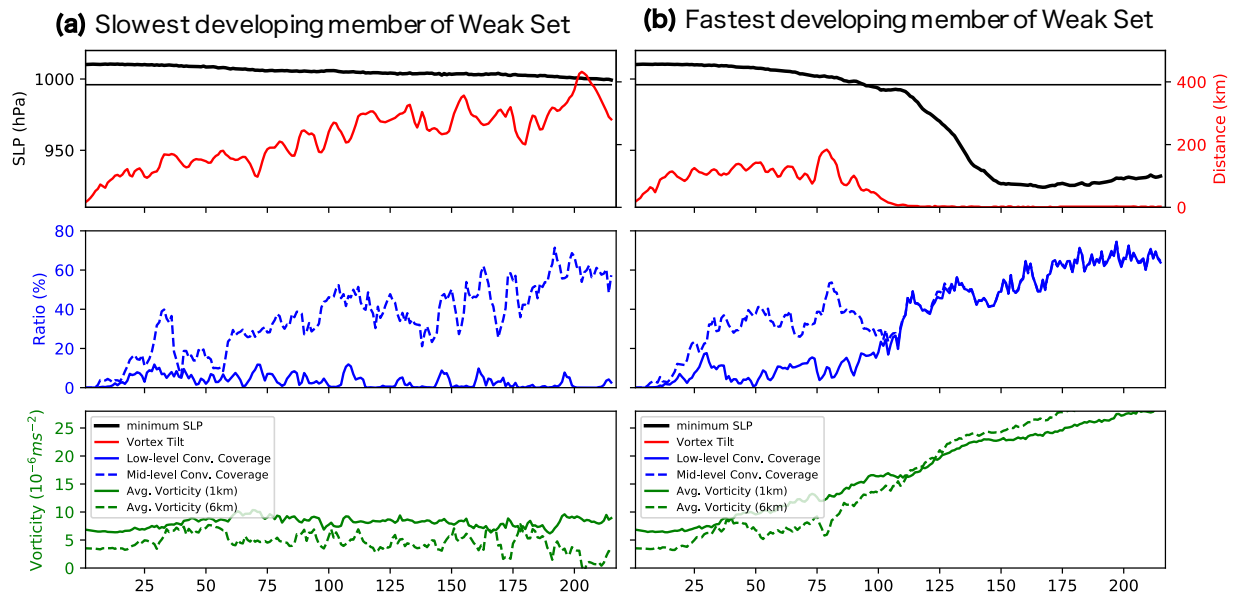


**Figure 3.16:** Time series of precursor events for **(a)** slowest developing ensemble member and **(b)** fastest developing ensemble member of the Weak sensitivity experimental set.

Figure 3.17 shows a histogram of the number of precursor events occurring before TC genesis timing for all the three sensitivity sets (threshold same as Fig. 3.9). Each of the three sensitivity sets has a widespread of ensembles. From the above results, we showed that the uncertainty of TC genesis under SH7.5\_Moist50 setup comes from the fact that each precursor event does not have a 100 % chance to lead to the next stage of development. The slowest developing ensemble members are those that have more failed attempts of precursor events. The REF set has an almost identical pattern of the histogram as SH7.5\_Moist50 with many convective coverage increase events and tilt decrease events, but only a few mid-level vorticity increase events. The Midlevel and Weak set displays distinctive patterns. For the Midlevel set, only mid-level convective coverage shows repetition, with the number of events ranging from one to seven, and other three variables do not have many repetitions before TC genesis. The Weak set is similar to the Midlevel set except for the mid-level vorticity increase. The sources of uncertainty in TC genesis scenarios can be different for the Main Set and the Sensitivity Set and will be discussed in the next section of 3.4.

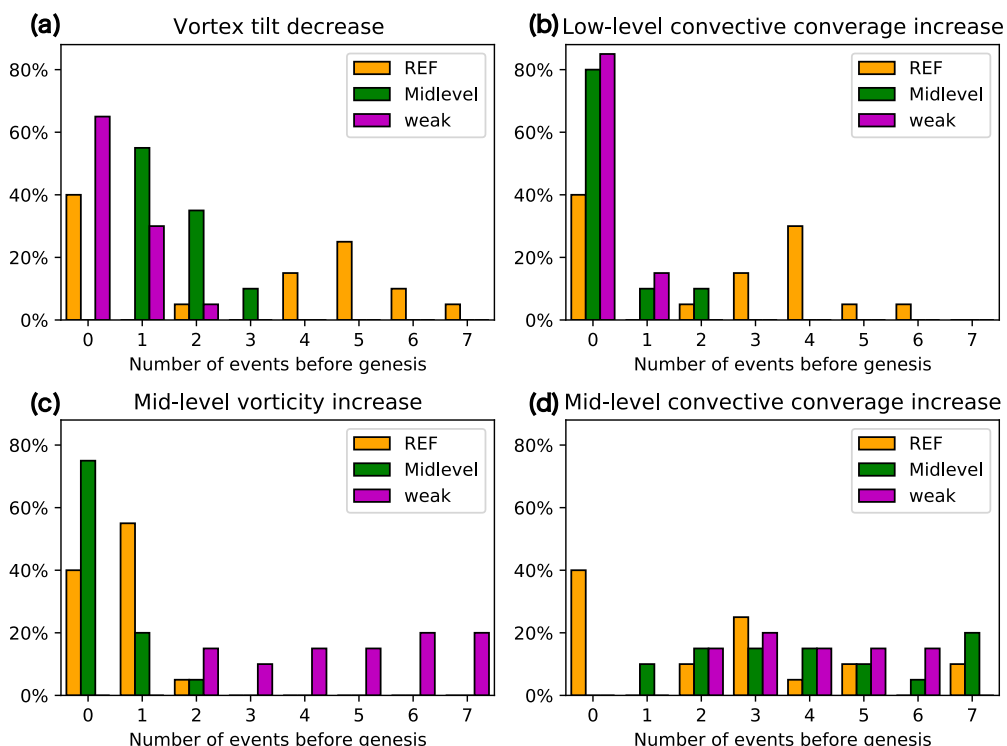


**Figure 3.17:** Histograms of the number of TC genesis precursor events occurring before the timing of genesis for the sensitivity test sets.

### 3.4 Discussion and Conclusions

Extensive mesoscale ensemble modeling conducted herein revealed that the marginally favorable environments—with not too weak nor not too strong magnitude VWS, not too dry or not too moist humidity, and not too weak or not too strong initial vortex—produced the most uncertain scenarios for tropical cyclogenesis, consistent with previous literature. A key finding was that there are repetitive cycles of precursor events lining up together before tropical cyclogenesis, and slow or non-developing ensemble members of the marginal environments go through a number of the cycles of precursor events that are very close to successful ones.

Based on the close examination of selected ensemble members and statistical analysis of geometric probability distribution and time-lagged correlations, we propose a theoretical diagram of the processes leading into tropical cyclogenesis in sheared and dry environments (Fig. 3.18).

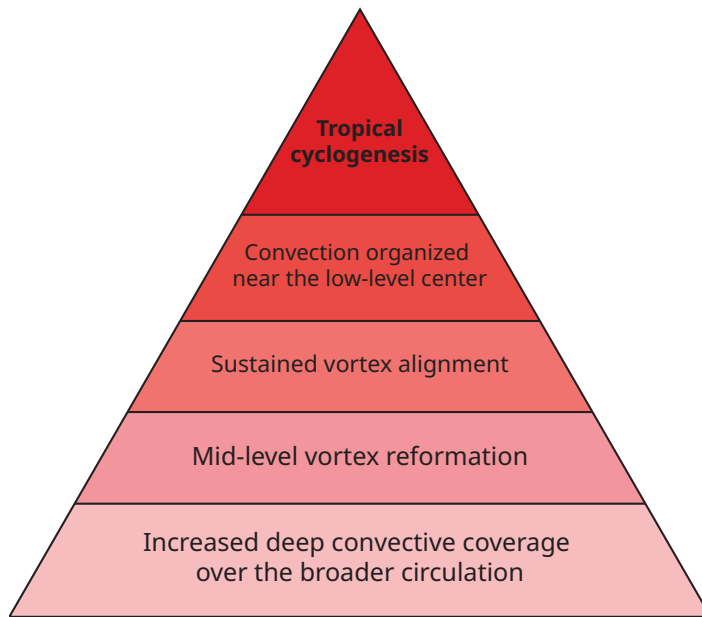


**Figure 3.18:** A pyramid diagram of tropical cyclogenesis in moderately sheared and dry environments

The first floor of the pyramid in Fig. 3.18 is that there emerges a wider area of deep convection (captured by increasing signals of both mid-level and low-level convective coverage parameters). When deep and wide convection has enough upward mass flux, a new mid-level vortex forms in-

side the broader pre-existing mid-level circulation, which results in rapid vortex tilt decrease: the second floor of the pyramid. The third floor is sustained vertical alignment of the newly reformed mid-level vortex and the low-level vortex. If the newly reformed mid-level vortex establishes itself aligned with the low-level vortex firmly, the vortex tower can be resilient against VWS (Schecter and Montgomery 2003; Reasor et al. 2004b). In our analysis, the vortex precession and alignment process appears as tilt keeps decreasing with some fluctuation (e.g., hour 100-125 of the fast-developing member and hour 150-175 of the slow-developing member from SH7.5\_Moist50 in Fig. 3.5). If the third floor was successful, vortex tilt keeps decreasing, and the wide deep convection that is centered around the mid-level center organizes itself near the low-level center: the fourth floor. Then, the mid-level vortex intensifies, as captured by mid-level vorticity increasing, and the simulated vortex finally reaches a tropical cyclone intensity: tropical cyclogenesis. We have shown that the moistening of the surrounding atmosphere is not necessarily a precursor to TC genesis but rather a result of the enhanced and organized convection of the developed TCs (Fig. 3.4).

In general, the steps illustrated in Fig. 3.18 are consistent with the downshear reformation mechanism suggested by Nguyen and Molinari (2015) and Rios-Berrios et al. (2018). However, the novelty of our research is in showing the probabilistic distribution of the precursor events and identifying the physical processes that serve as the bifurcation points between the developing and non-developing vortices in the course of the repetitive cycles of precursor events. The ensemble sets that have a narrower ensemble spread (small VWS and high humidity) need only a few cycles of precursor events, but the ensemble sets that have a wider ensemble spread have some members developing after one or two cycles and other members developing after 7-8 cycles of precursor events repeating with a 36-48 hours period (Fig. 3.9). The widespread distribution of the number of precursor events, required to reach TC genesis, is related to lower success rate of each precursor event according to the geometric probability model. Whether each cycle of precursor events is successful for TC genesis or not is somewhat random due to the stochastic characteristic of con-

vective scale phenomena, but the probability of success of each cycle can increase with time as the environment becomes moister and more favorable with each cycle (Fig. 3.6 vs. Fig. 3.7).

The critical bifurcation point appears to be the third floor of the pyramid, the sustained vortex alignment process, for SH7.5\_Moist50 and SH7.5\_Moist25 set. Mid-level convective coverage increases and vortex tilt decreases multiple times before TC genesis (Fig. 3.10), and these variables have a longer lead time with smaller correlation and larger standard deviation (Fig. 3.14), which means that not all the events of mid-level convective coverage increasing and vortex tilt decreasing end up with low-level convective coverage increasing nor mid-level vorticity increasing. We interpret this result that most of the slow-developing members of SH7.5\_Moist50 fail at the sustained vortex alignment process; there is a newly reformed mid-level vortex close to the low-level center, but the mid-level vortex is shifted away downshear side so soon before the vortices are vertically aligned and grow resilience against VWS. Then, the vortex tilt increases again, and the cycle shall be reset, going back to the first floor of the pyramid again. We cannot fully understand the differences between the mid-level vortex that can "phase-lock" with the low-level versus the ones that are carried away because some cases exhibited very similar patterns, yet one underwent TC genesis and the other failed. Nevertheless, we can infer from saturation fraction analysis and mid-level vortex cross-sections that a larger spatial scale mid-level vortex and a more moist environment helps sustain the vortex alignment process.

In addition to the SH7.5\_Moist50 and SH7.5\_Moist25 from the Main Set, the sensitivity experiments of the Midlevel Set and Weak Set also have wide ensemble spread in the timing of genesis. The bifurcation point for the Midlevel set ensembles appears to be mid-level vortex reformation process, the 2nd floor of the pyramid. The time series of mid-level convective coverage show multiple bursts even for the non-developing member of the Midlevel Set (Fig. 3.15 a), but vortex tilt shows a steadily increasing trend. We infer that the widespread convection was not persistent enough to produce a new mid-level vortex center. The non-developing members of the Weak sensitivity set also fail at the 2nd step of mid-level vortex reformation. However, unlike the Midlevel Set, mid-level convective coverage persistently increased for the Weak Set. It seems that the non-

developing members of the Weak Set did not form a new smaller scale mid-level vortex but kept increasing the pre-existing mid-level vortex by concentrating all the convective activity around the prescribed mid-level vortex center. As a result, mid-level convective coverage keeps increasing and inner-core mid-level vorticity also oscillates around the threshold value but the low-level vortex is still detached from these convective and vortical activities (see Fig. 3.16 a and Fig. 3.17 c, d).

We interpret the results of this study as representative of an 'Anna Karenina principle':

*All happy families are alike; each unhappy family is unhappy in its own way.*

The principle can be applied to our theoretical pyramid diagram in that all successfully developing TCs share a common set of precursor events that lead to TC genesis, while a deficiency in any of the precursor events dooms a failure of genesis.

Here, we address some limitations of our methodology of idealized simulations. The point-downscaling method forces VWS without imposing the temperature gradient induced by the shear, and according to the thermal wind balance equation, with  $10 \text{ m s}^{-1}$  VWS and 720 km domain size, the temperature gradient is maximum around  $1^\circ\text{C}$ , which is not negligible but still quite small (see Appendix A of Tao (2015) for details). Our idealized simulations simplify the variable space by having the other variables constant to isolate the impacts of varying VWS, environmental humidity, and vortex structure. In reality, there is a lot more complexity that contributes to the uncertainty around TC genesis. For example, we have not tested the sensitivity of our results to radiation and microphysics scheme choices. Rios-Berrios (2020) showed that the ensemble spread of TC intensification under moderate VWS decreased significantly when more realistic radiation and microphysics schemes were used. As future work, we intend to examine if our theoretical diagram holds true when short- and long-wave radiation and larger momentum microphysics schemes are used and if the bifurcation points of different marginal setups would be sensitive to the choice of these schemes. We hypothesize that an Anna Karenina principle still holds in these more complicated scenarios, with multiple ways the process can fail, but genesis still occurring when the necessary confluence of conditions comes together to produce a tropical cyclone.

# **Chapter 4**

## **Monsoon tail rainband and its effects on subsequent tropical cyclogenesis**

### **4.1 Introduction**

The western North Pacific (WNP) monsoon (i.e., the Asian-Australian monsoon) and tropical cyclones (TCs) together have enormous societal impacts. Climatologically, in the Asian monsoon region, rainfall in early summer (May-June) is due to large-scale monsoon southwesterlies, and much of the rainfall in late summer (July-September) is produced by TCs (Chen and Yoon 2000; Takahashi et al. 2015).

Monsoons and TCs are not independent of each other. During the Propagation of Intra-Seasonal Tropical OscillatioNs (PISTON) field campaign, which was conducted in the summer of 2018 and 2019 over the WNP, we observed that most of the TCs had an elongated rainband in their southwestern (SW) quadrant. A great example was Typhoon Jebi (2018). Jebi started to exhibit enhanced convection in its SW quadrant around August 31st, 2018 (Fig. 4.1). During PISTON, we called the rainband in the SW quadrant of the TC the "monsoon tail," assuming that the low-level convergence of monsoon southwesterlies and the TC-induced cyclonic circulation produced the particularly vigorous convection in the SW quadrant. As Jebi was moving northwestward, the monsoon tail rainband became detached from the main TC circulation, but the widespread convection persisted for a couple of days afterward (Fig. 4.2). The widespread convective area had a closed low-level circulation observed by satellite and was also monitored for potential TC development. It was tracked as an Invest 98W by the Joint Typhoon Warning Center (JTWC). Invest 98W dissipated before it reach TC intensity (Fig. 4.2 d).

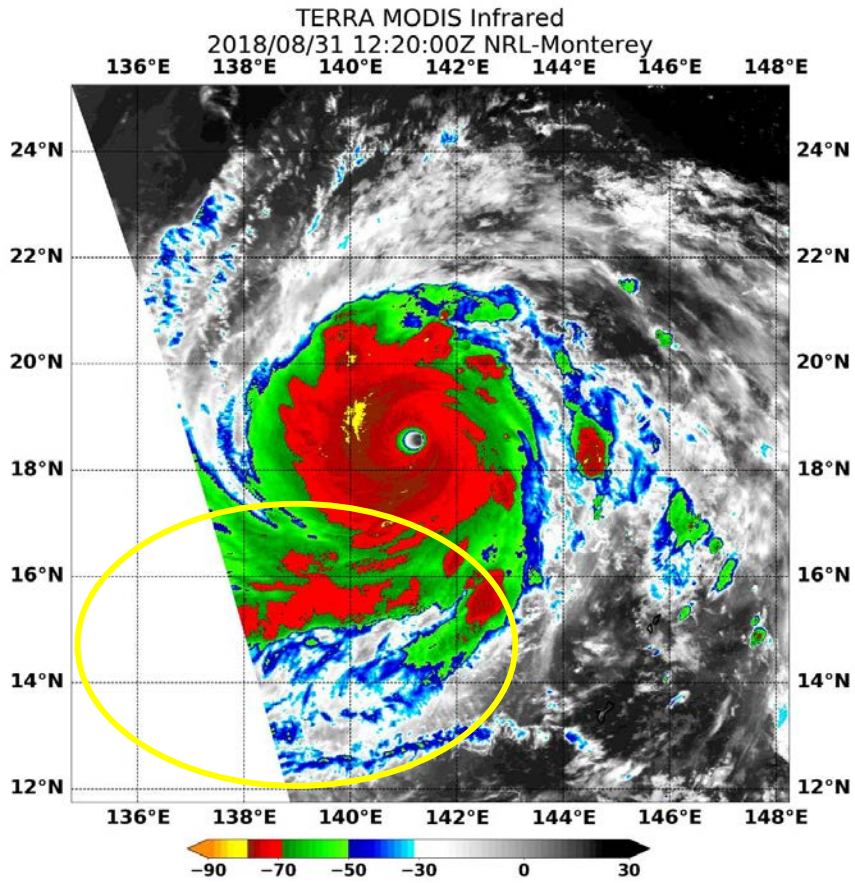


**Figure 4.1:** TERRA MODIS Infrared image of Supertyphoon Jebi (2018) at 12:20 UTC 31st August. The brightness temperature is in Fahrenheit. The elongated rainband in the southwestern quadrant (i.e., “monsoon tail” rainband) is highlighted with a yellow circle. Modified image courtesy of the US Naval Research Laboratory (NRL).

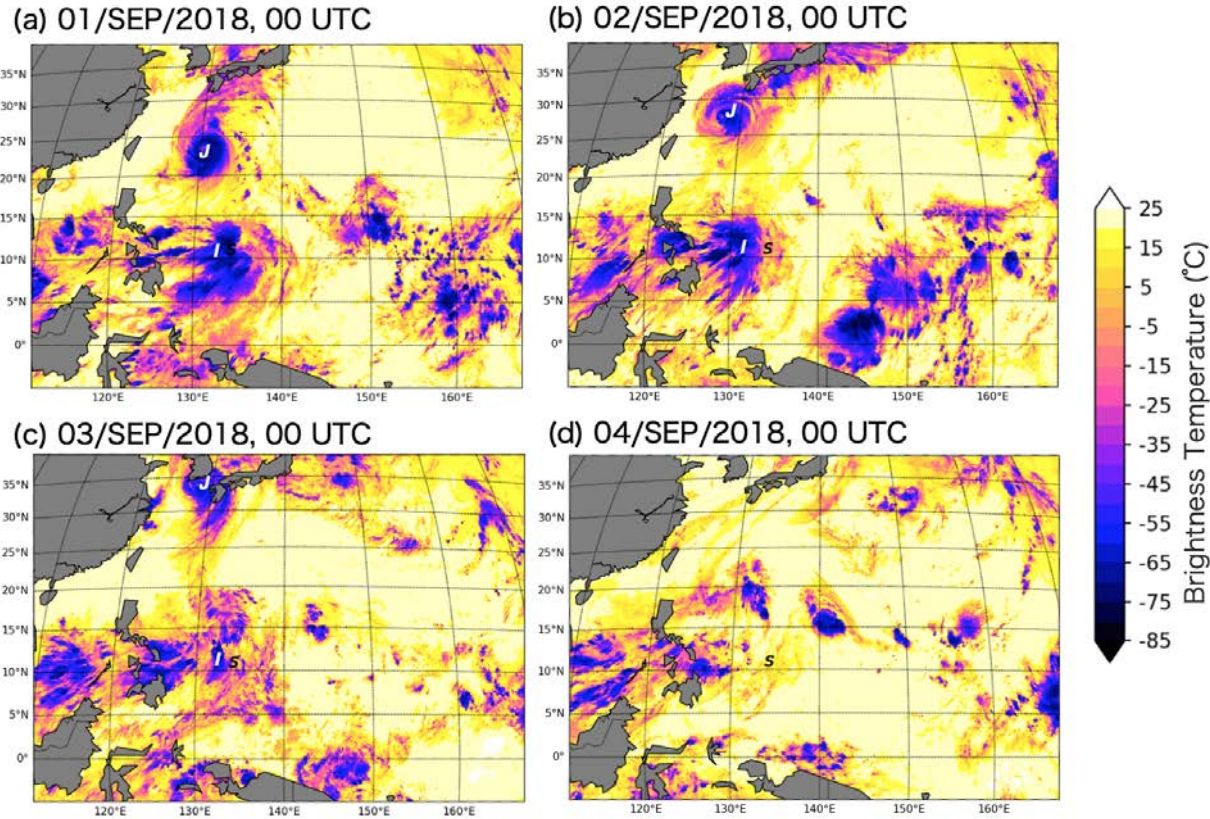


**Figure 4.2:** Daily Gridsat-B1 infrared brightness temperature over the western North Pacific from 01/09/2018 to 04/09/2018. Typhoon Jebi is marked with a ‘J’ and the research vessel (R/V) Thompson’s location is marked with an ‘S’. The area marked with an ‘I’ is an area of widespread convection, which was monitored as an Invest for potential tropical cyclogenesis by the Joint Typhoon Warning Center.

The late summer monsoonal environment is usually favorable for TC genesis in the WNP. TC genesis in the WNP is often characterized as affected by five environmental precursors: monsoon shear lines (SLs), monsoon gyres (GYs), confluence regions (CRs), easterly waves (EWs), and energy dispersion by preexisting TCs (PTC). SLs, GYs, and CRs are all parts of the monsoon westerly regime extending eastward to the central Pacific in the summer, and EW and PTC are tropical disturbances that are westward-propagating. Over 70% of WNP TCs on average form within the monsoon trough region with interannual variations ranging from 50% to 100% (Molinari and Vollaro 2013). Previous studies reported that SL and CR patterns explained the majority of TC genesis cases in the WNP (Ritchie and Holland 1999; Yoshida and Ishikawa 2013), but Chen et al. (2008) argued that over 80% of tropical cyclogenesis occurrences in the WNP were, directly and indirectly, due to EWs, including TCs developing via monsoon trough-easterly wave interaction.

The discrepancy among the statistical studies arises due to TC genesis cases that had multiple environmental precursors acting together. The EW and PTC patterns were often found to be collocated with the CR pattern (Yoshida and Ishikawa 2013). The monsoon confluence provides abundant moisture, and easterly waves can grow there with the help of diabatic heating from deep convection (Serra et al. 2008). In the monsoon confluence region disturbances may also grow from barotropic energy conversion (e.g. wave accumulation; Holland 1995; Sobel and Bretherton 1999; Au-Yeung and Tam 2018).

Tropical cyclogenesis from a monsoon tail rainband could also be a case of multiple environmental precursors acting together. Zehr (1992) found that localized monsoon westerly wind surges appear prior to deep convection in most TC genesis cases in the WNP during 1983–1984. Briegel and Frank (1997) documented that 20 % of TC genesis in the WNP during 1988–1989 seemed to be supported by monsoon westerly surge that was further enhanced by the cyclonic wind field from preexisting TCs. The efficiency of upscale growth and merger process inside the wave pouch could depend on the monsoon flow that is impinging on the southwestern side of the wave pouch.

Large-scale environments of PISTON 2018 were reviewed by Sobel et al. (2021), and the coupling between convective modes and the large scale environments during PISTON 2018 and 2019

were examined by Chudler and Rutledge (2021). These PISTON studies mention the "monsoon tail" feature but did not investigate it in detail. Although Invest 98W did not undergo tropical cyclogenesis, our observation of monsoon tail rainband during PISTON and, in particular, Invest 98W case prompted several scientific questions:

- How common is it for TCs in the WNP to have a monsoon tail rainband?
- How does the monsoon tail rainband sustain itself after it is detached from the TC?
- How common and likely is it for the monsoon tail rainband to lead to subsequent TC genesis?

This study answers the above three science questions through climatological analysis and case studies of the monsoon tail rainbands of Typhoons Jebi (2018) and Lingling (2019) that were observed during PISTON. We show that the monsoon tail rainband is a common feature for TCs in the WNP monsoonal area, and its presence and longevity are a result of TCs interacting with both the low-level and upper-level flow. Despite the convective enhancement, the environment around the separated monsoon tail rainband is not generally found to be favorable for subsequent genesis due to enhanced VWS. The chapter is organized as follows. Section 4.2 introduces the data and methods used in this study. Section 4.3 discusses the climatology of the monsoon tail rainband, including its interannual variability as related to indices of both the monsoon and ENSO. The section also discusses monsoon tail rainband cases that led to TC genesis. Finally, section 4.4 summarizes the results and presents some ideas for future work.

## 4.2 Data and Methods

### 4.2.1 Data

Satellite brightness temperature data are from the Gridded Satellite (GridSat-B1) dataset, which is provided by the NOAA Climate Data Record Program (Knapp 2014). GridSat-B1 has data from January 1980 to the present for the entire globe. The data is at three-hourly temporal resolution and  $0.07^\circ \times 0.07^\circ$  horizontal resolution. To map the satellite data into the equirectangular projection, the satellite pixel nearest the value of the latitude and longitude was selected (i.e., resampling).

The version used in this analysis is v02r01, which was released in April 2014. We used the  $11\text{ }\mu\text{m}$  infrared window channel, which is of Climate Data Record quality; Climate Data Record quality is defined as “a time series of measurements of sufficient length, consistency, and continuity to determine climate variability and change” (National Research Council 2004).

Environmental fields at three-hourly timescales were obtained from the ECMWF’s fifth generation reanalysis dataset (ERA5) of the global climate (Hersbach et al. 2020). ERA5 reanalysis data are currently available from 1 January 1979 to the present. The gridded ERA5 reanalysis has a horizontal resolution of  $0.25^\circ \times 0.25^\circ$ . Monthly mean of daily mean ERA5 data were utilized to create monthly climatologies.

For TC data, the location of the TC center and the TC’s intensity, were obtained from best track data from the International Best Track Archive for Climate Stewardship (IBTrACS) version 4 (Knapp et al. 2010, 2018). We used three-hourly data (interpolated from six-hourly data by IBTrACS) for TCs over the western North Pacific (WNP) from 1980 to 2019 for June–September. For the 40-year period, there were 1,392 TCs recorded in the WNP IBTrACS data set, with 850 TCs in the WNP monsoonal area, defined as  $0^\circ\text{N}–30^\circ\text{N}$  and  $100^\circ\text{E}–150^\circ\text{E}$ .

There are many different monsoon indices that examine various parts of the monsoon domain using different environmental variables (e.g., Webster and Yang 1992; Wang et al. 2008). Here we look at the western North Pacific (WNP), and we use the East Asian - Western North Pacific monsoon index as defined by Wang et al. (2008). This index is calculated using zonal wind at 850 hPa (U850): average U850 over the box spanning  $5^\circ\text{N}–15^\circ\text{N}$ ,  $90^\circ\text{E}–130^\circ\text{E}$  minus average U850 over the box spanning  $0^\circ\text{N}–20^\circ\text{N}$ ,  $110^\circ\text{E}–140^\circ\text{E}$ . This index measures how far monsoon westerlies extend northeastward. The index was averaged for June through September (JJAS) to represent the summertime monsoon over the WNP.

To investigate the relationship between the monsoon tail rainband feature and El Niño-Southern Oscillation (ENSO), we used the ENSO Longitude Index (ELI) developed by Williams and Patricola (2018). The ELI is a sea surface temperature (SST)-based index that approximates the longitudinal center of the Walker Circulation. The ELI has been shown to better capture the nonlinear

Walker circulation than other traditional ENSO indices. We downloaded monthly ELI data and calculated seasonal means for June–September for the 1980–2019 period.

Both the East Asian - WNP monsoon index and the ELI were normalized with a mean of zero and the standard deviation ( $\sigma$ ) of one, and anomalous seasons were defined to be seasons whose index value were larger than  $+1\sigma$  or smaller than  $-1\sigma$ .

#### 4.2.2 Methods

To track the "monsoon tail" rainband, we use the infrared brightness temperature (BT) as a proxy for convection, with colder BT representing higher cloud tops. Thus, colder BTs are indicative of deep and vigorous convection. We track the center of each TC in the western North Pacific using the IBTrACS track data. Then, we take all of the Gridsat-B1 grid points inside the  $10^\circ$  radius circle centered the TC center if the TC center was located in the area bounded by  $0^\circ\text{N}$ – $30^\circ\text{N}$  and  $100^\circ\text{E}$ – $150^\circ\text{E}$ .

Two metrics are then calculated: radial mean BT and radial convective coverage. Both metrics are calculated over an annulus using a  $1^\circ$  interval (Fig. 4.3). For example, the mean BT for the annulus at  $4^\circ$  radius means that all BT grid points inside an annulus with a radius range from  $3$ – $4^\circ$  are averaged. The BT data has  $0.07^\circ$  grid resolution, so 14 BT grid points fit in a  $1^\circ$  annulus. The minimum radius in our calculation is  $1^\circ$ , and this indicates a circle with a radius of  $1^\circ$  rather than an annulus because in the range from  $0$ – $1^\circ$ , the center is filled. The convective coverage is calculated as the percentage of grid points that have a BT below a threshold over all of the grid points inside the annulus. We tested two different thresholds suggested by previous literature on tropical convection: the 215-K deep convection index of Fu et al. (1990) and the 225-K cold cloud index of Nakazawa (1988). The results were consistent between the two thresholds, and we consequently only show the deep convection index 215-K figures here. The annulus area is divided into four quadrants — northeast (NE), northwest (NW), southwest (SW), and southeast (SE). The quadrant anomaly is calculated as the mean/coverage value over the quadrant of the annulus minus the mean/coverage value over the whole annulus area.

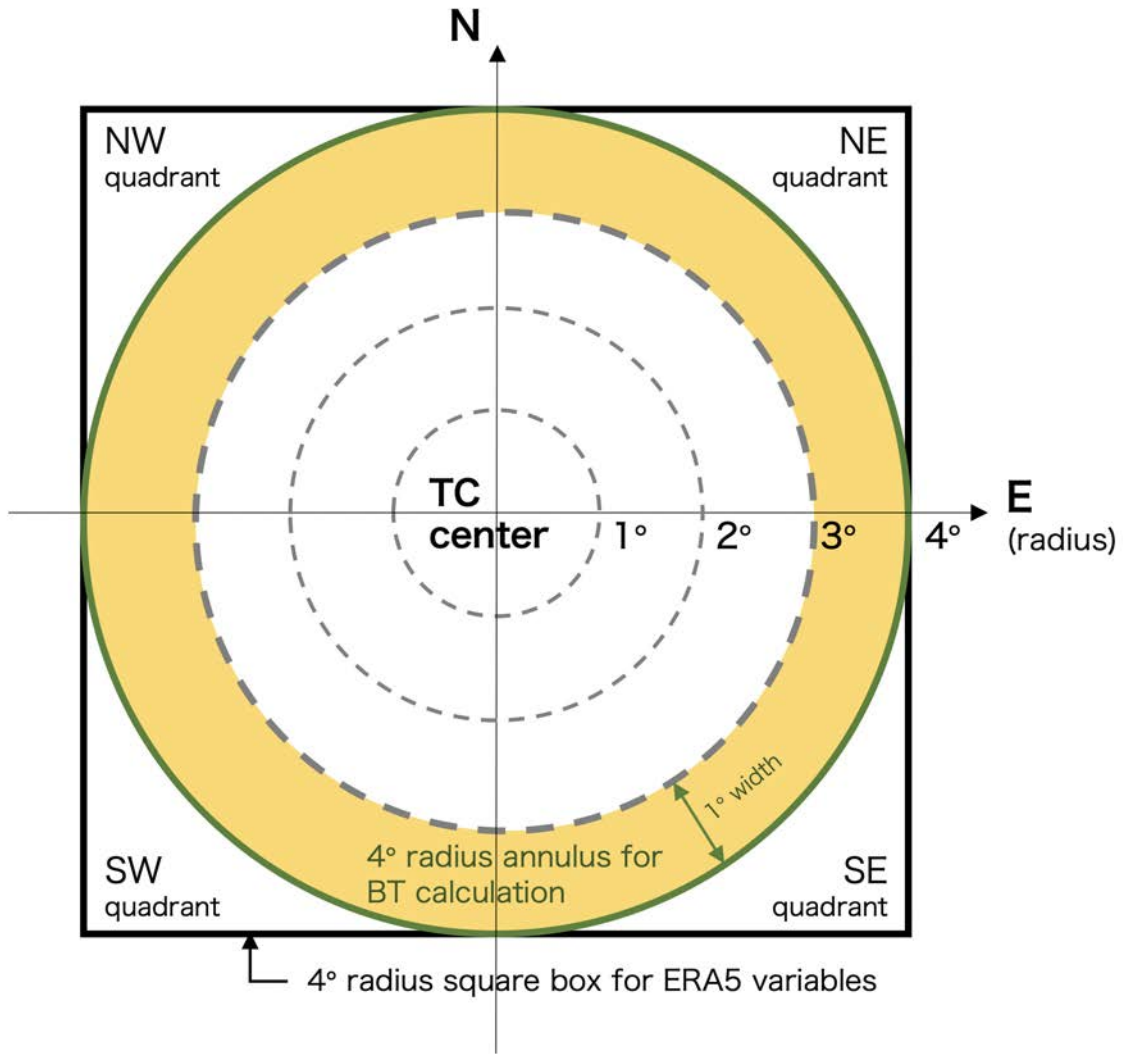


**Figure 4.3:** A diagram of the methodology used to calculate infrared brightness temperature (BT) and environmental variables from ERA5 in our TC-centered analysis. BT data are taken as an annulus with  $1^{\circ}$  width, and ERA5 data are calculated using a square box. For example, for an analysis st  $4^{\circ}$  radius, BT grid points inside the yellow area are used, and ERA5 grid points spanning an  $8^{\circ} \times 8^{\circ}$  box are used.

Three-hourly wind data from ERA5 were synced with the BT data. Zonal vertical wind shear (U-shear) and meridional vertical wind shear (V-shear) were calculated as the wind difference between 200–850 hPa. Unlike BT data that were taken in an annulus shape, the wind data were averaged over a square box centered on the TC location at a specific time. For example, matching with a  $4^\circ$  radius annulus of BT data is an  $8^\circ \times 8^\circ$  square of ERA5 data (Fig. 4.3).

To track the vortex center of still developing systems in our case studies of Typhoon Jebi(2018)'s monsoon tail and Typhoon Lingling(2019)'s monsoon tail, the Okubo-Weiss parameter was calculated from ERA5 wind data:

$$W = S_n^2 + S_s^2 - \omega^2 \quad (4.1)$$

We found that Okubo-Weiss parameter ( $W$ ) is better than relative vorticity ( $\omega$ ) for tracking developing TCs in that it takes into account the normal strain ( $S_n$ ) and the shear strain ( $S_s$ ) so that the parameter measures the relative importance of rotation over deformation. Eddies in which vorticity dominates strain are denoted by a negative  $W$ . The Okubo-Weiss parameter has been frequently used to track TC genesis (Dunkerton et al. 2009; Tang et al. 2020).

## 4.3 Results

### 4.3.1 Climatology of “monsoon tail” rainbands

We first investigated how common the monsoon tail rainband is for the 850 TCs over the monsoonal area in the WNP during 1980–2019. We tracked deep convection using infrared brightness temperature (BT) as described in the Methods section.

Figure 4.4 shows the anomaly in BT from the radial mean (i.e., anomaly from the axisymmetric BT at each radius) for each TC quadrant. The BT is the lowest in the southwest (SW) quadrant, which means stronger and deeper convection in the SW quadrant. The fact that enhanced convection in the SW quadrant appears in a 40-year climate composite highlights that the monsoon tail rainband is a climatologically common feature for TCs in the WNP monsoonal region. In general, southern quadrants have colder BTs than northern quadrants. As you move closer to the center of

the TC, all of the anomalies are concentrated around 0, meaning axisymmetric convection in the inner-core region of TCs. As the radius increases, the quadrant-dependent asymmetry becomes more apparent. At  $8\text{-}10^{\circ}$  radius, the SW quadrant annulus has about a  $20^{\circ}\text{C}$  colder BT than the radial average BT.

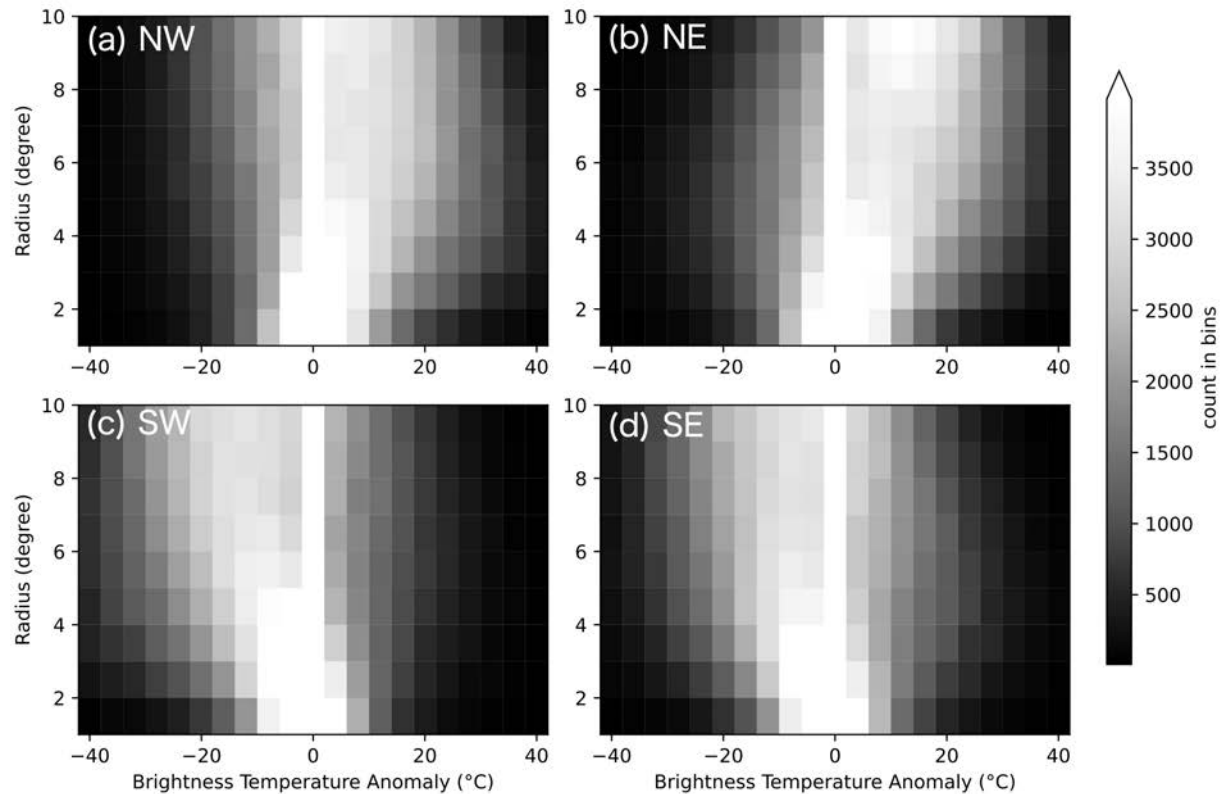


**Figure 4.4:** 2-D histogram of infrared brightness temperature anomalies from the radial mean of the annulus around the tropical cyclone (TC) center for  $0\text{-}30^{\circ}\text{N}$ ,  $100\text{-}150^{\circ}\text{E}$  for June-September 1980-2019 for the (a) northwestern, (b) northeastern, (c) southwestern, (d) southeastern quadrant of the TC.

Figure 4.5 shows quadrant-dependent convective activity as in Fig. 4.4 but with deep convection coverage. Similar to Fig. 4.4, the SW quadrant shows the largest area covered by deep convection (BT < 215 K). The quadrants in order of broadest convective coverage to smallest are SW, SE, NE, and NW quadrants. The largest spread in convective coverage depending on quadrants is found around  $4\text{-}6^{\circ}$  radius. For  $8\text{-}10^{\circ}$  radius, the spread is smaller because the area of the annulus is so large that the deep convective coverage ratio is in general small across all quadrants.

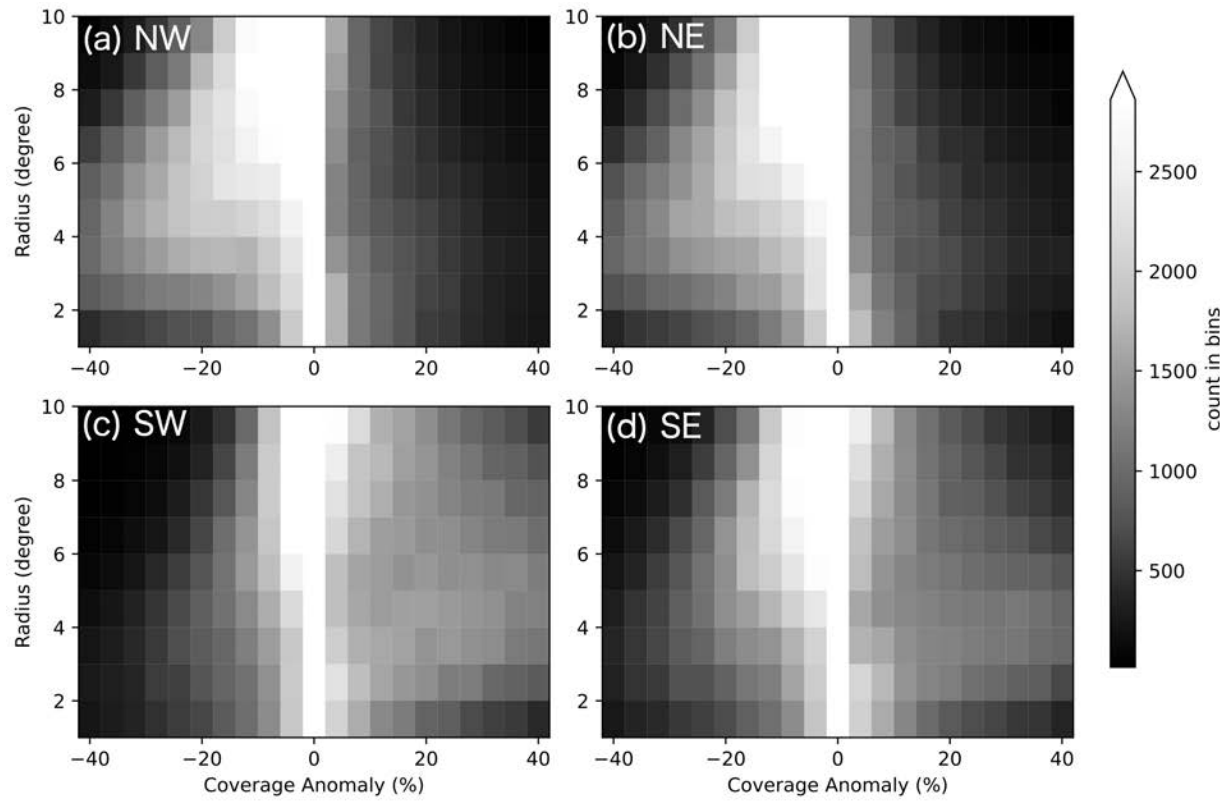


**Figure 4.5:** As in Fig. 4.4 but for deep convection coverage anomalies.

From Figs. 4.4 and 4.5, we find that the monsoon tail feature is not just limited to the 2018-2019 typhoon seasons but is more of a common feature for TCs over the WNP. Given these findings, we now ask the following research questions: What organized the enhanced convection in the SW quadrant? Was the cause of this enhanced convection the monsoon southwesterlies? Or, was the cause of enhanced convection related to the characteristics of each TC, such as the TC's location or intensity? We calculated correlations between the mean BT anomalies in the SW quadrant (monsoon tail rainband proxy) and other environmental/TC variables at each radius (Fig. 4.6). All of the six variables in Fig. 4.6 have significant correlations with the monsoon tail proxy. The significance of correlations is measured at the 99% confidence level corresponding to a p-value <0.01 based on a two-sided Student's t-test. The correlation increases with radius as the mean BT anomaly increases with radius (Fig. 4.4).

Somewhat surprisingly, zonal vertical wind shear (200–850 hPa) (U-shear) had the best correlation with the monsoon tail rainband feature rather than 850 hPa zonal wind (U850) or low-level convergence. U-shear had a correlation  $> 0.6$  with the monsoon tail rainband at the radii larger than  $5^{\circ}$ s. A positive correlation means that the two variables have the same signal in that easterly shear (negative U-shear) is correlated with the monsoon tail rainband (negative BT anomaly in SW). This finding makes physical sense as VWS shifts convection to the downshear side of the TC. The next best correlation with the monsoon tail rainband feature is found in the meridional vertical wind shear (V-shear) and U850 with magnitudes of correlations around 0.4. Negative V-shear (northerly shear) acts to shift convection southward from the TC center (negative BT anomaly in the SW quadrant). For U850, the correlation is negative since low-level westerlies (positive U850) enhance the monsoon tail rainband (negative BT in the SW quadrant). The three other variables, low-level convergence, TC intensity, and TC longitude, all have significant but small correlations of 0.2 with the monsoon tail feature. Positive low-level convergence, weaker TC intensity, and a westward shift in TC location are all associated with an enhanced monsoon tail rainband.

The results of the correlation analysis imply that enhanced convection in the SW quadrant is more associated with VWS (U-shear and V-shear) than low-level monsoonal flow (U850 and

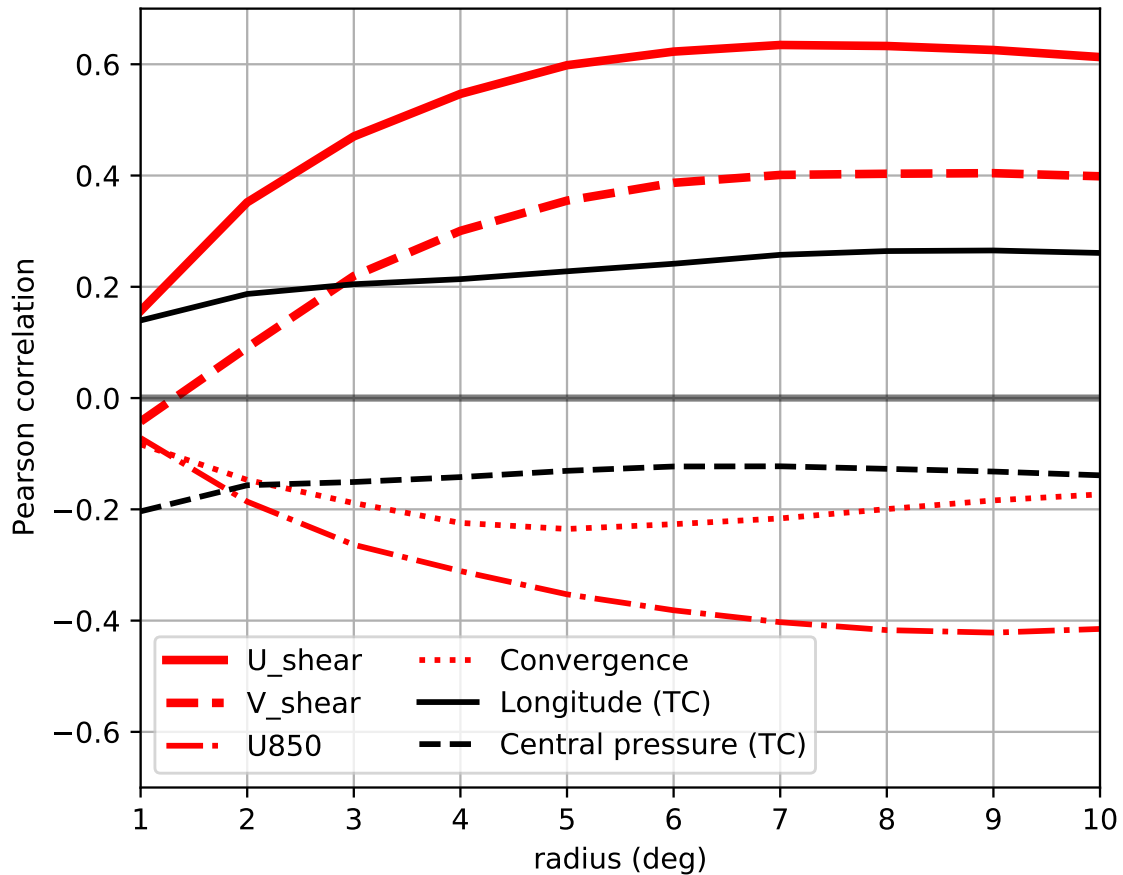


**Figure 4.6:** Pearson correlation between southwestern quadrant brightness temperature (“monsoon tail” proxy) and environmental/tropical cyclone (TC) variables as a function of radius from the TC center. Environmental variables are in red and TC variables are in black.

low-level convergence). Figure 4.7 shows the summertime climatology of WNP dynamic and thermodynamic fields. The zonally-elongated band of enhanced 200 hPa divergence, 850 hPa vorticity, and 850 hPa relative humidity indicates the monsoon trough region. Around the monsoon trough region, there are northeasterlies at upper levels, and southwesterlies at lower levels producing large northeasterly vertical wind shear. The climatological northeasterly VWS is consistent with the climatological convective asymmetry in the SW quadrant of TCs. Thus, the convective asymmetry in the SW quadrant of TCs over the monsoonal region in the WNP can be partly explained by the climatological northeasterly VWS. The positive relationship between the westward shift in longitude and the monsoon tail rainband can also be explained by the wind field. The direction of the low-level winds changes around 130-140 °E; with low-level southwesterly flow farther west and easterly trade wind flow farther east. Between 110-150 °E, the farther west a TC tracks, the greater the chance for the TC to experience larger northeasterly VWS, favoring the development of a monsoon tail rainband feature.

If the monsoon tail rainband was a product of low-level convergence, stronger TCs would have a better chance of having a monsoon tail rainband because stronger cyclonic winds (northwesterlies) in the SW quadrant would produce larger convergence meeting with the monsoon southwesterlies. However, the correlation analysis revealed that the monsoon tail feature was only weakly correlated with intensity, consistent with the fact that VWS is the most influential factor for the monsoon tail. Stronger TCs are more resilient to VWS, and they tend to maintain axisymmetric organization in spite of shear. Weaker TCs are more vulnerable to VWS, and consequently, their convection is more susceptible to be shifted to the downshear side.

### 4.3.2 Interannual variability of the "monsoon tail" rainband

Vertical wind shear, low-level winds, and predominant TC tracks all have interannual variability. Since the monsoon tail rainband has significant correlations with the environment, we can infer that the monsoon tail rainband would also have interannual variability. We explored the relationships with two interannual oscillation indices: the ENSO longitude index (ELI) and the WNP-East Asia monsoon index. Figure 4.8 displays the time series of the normalized ELI and the WNP mon-

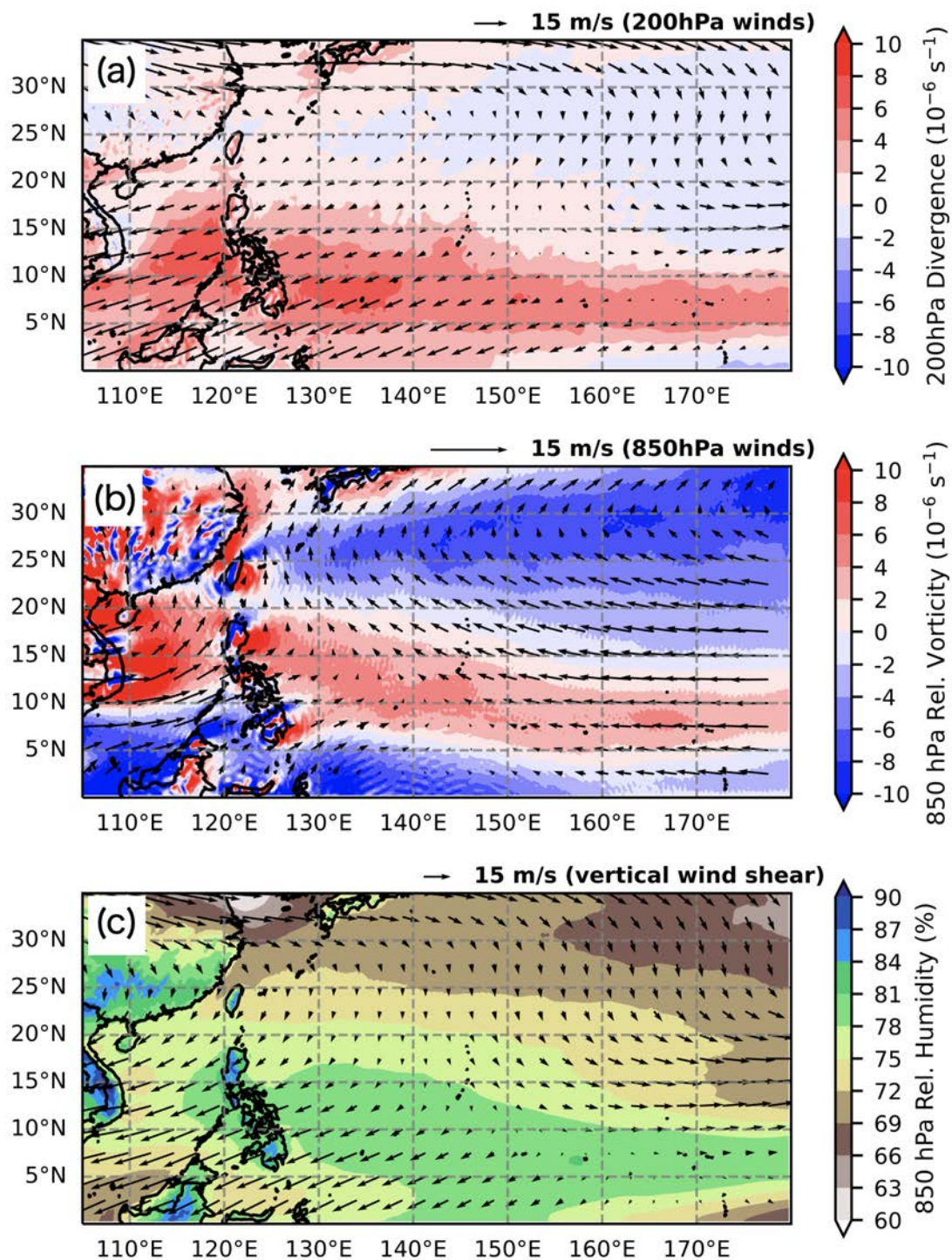


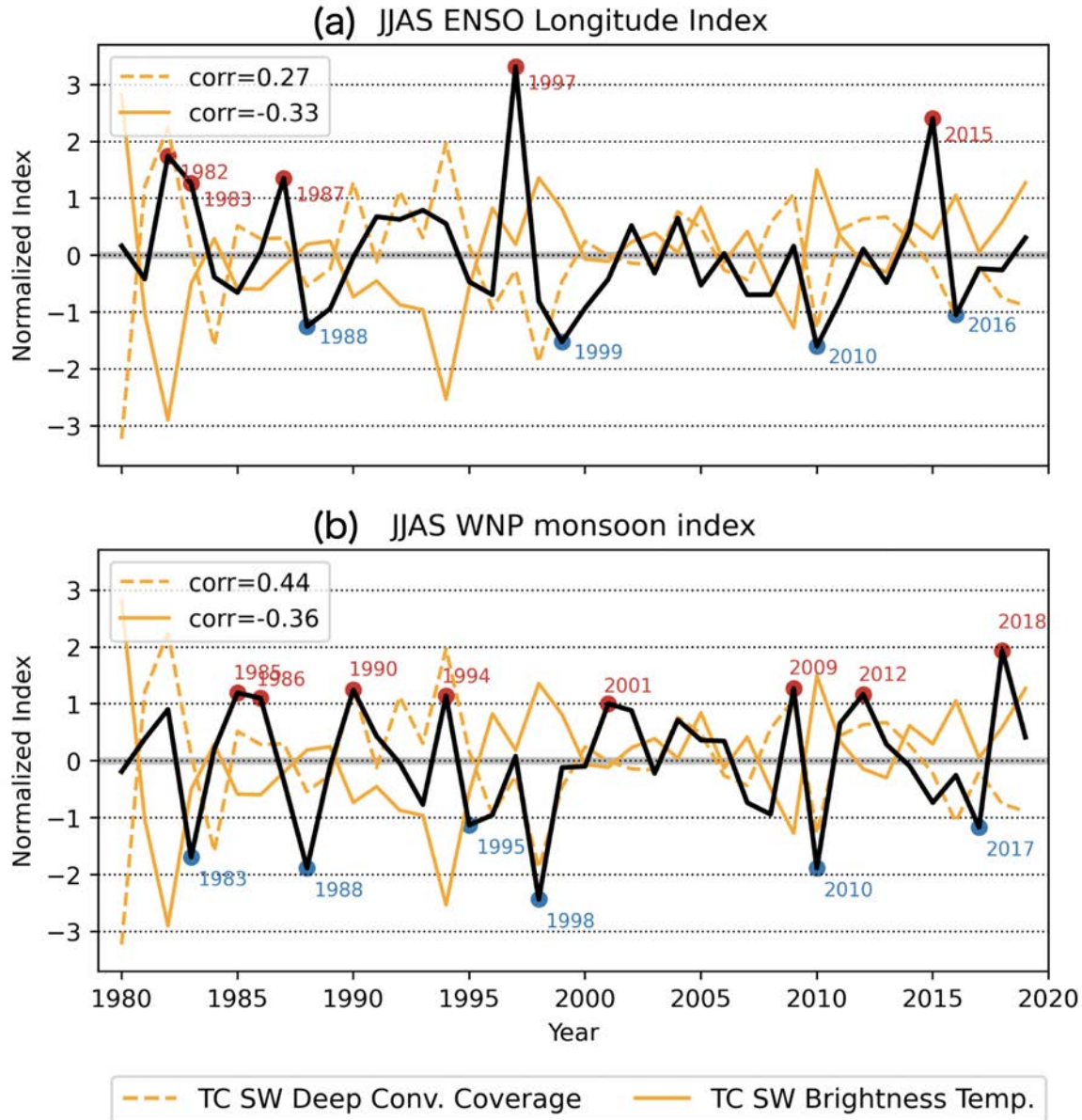
**Figure 4.7:** 40-year summertime (June–September) climatology of (a) divergence and winds at 200 hPa, (b) relative vorticity and winds at 850 hPa, (c) relative humidity at 850 hPa and deep-layer (200–850 hPa) vertical wind shear over the western North Pacific.

soon index for the boreal summer (June–September). The ELI and the WNP monsoon index do not significantly correlate with each other ( $r = 0.18$ , p-value > 0.27). The ELI captures the SST variance in association with ENSO and its impact on the Walker Circulation. The monsoon index measures how far east the monsoon westerlies extended each year.

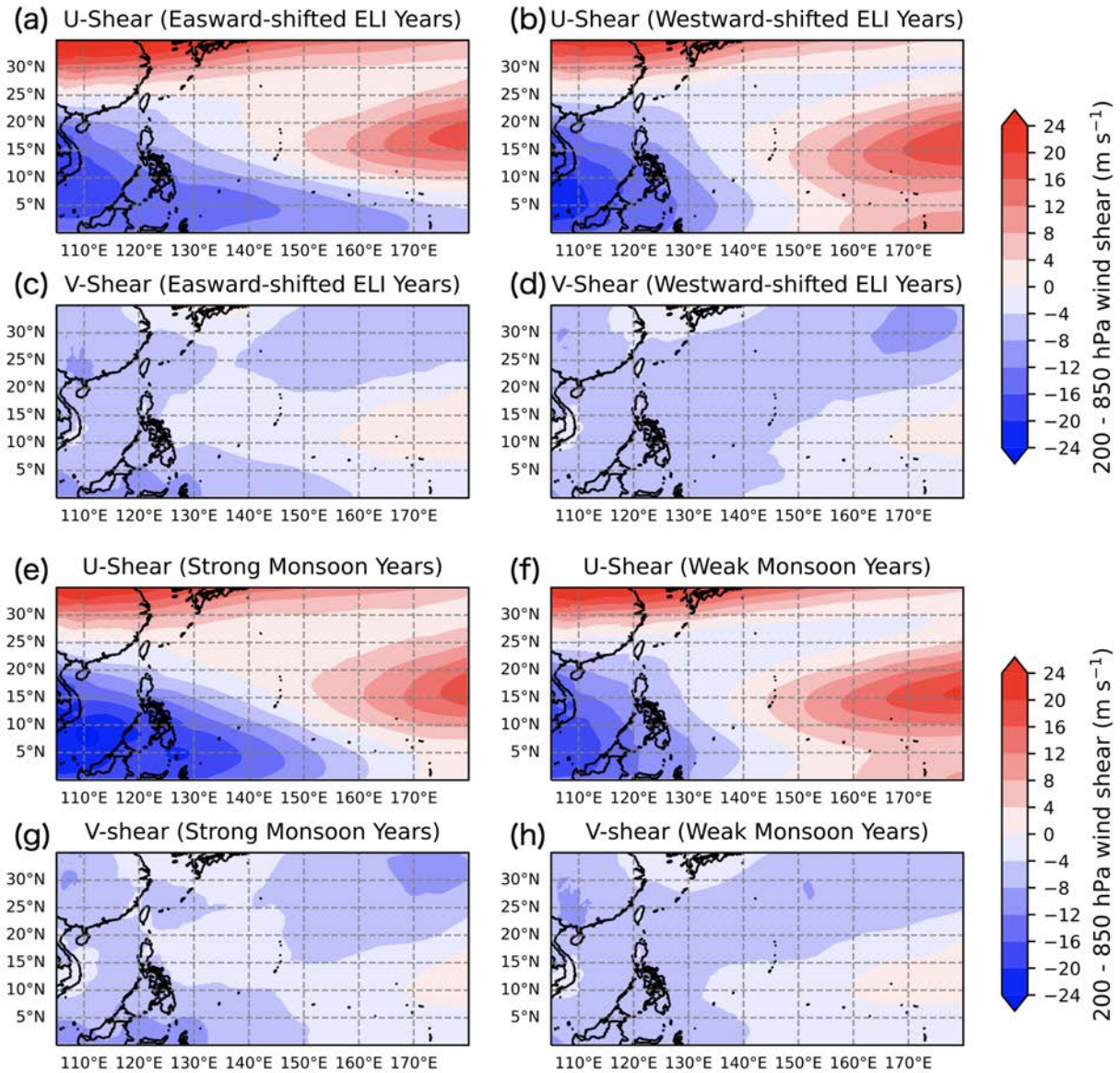
Orange lines in Fig. 4.8 show interannual variability of the monsoon tail rainband proxy (i.e., the BT anomalies in the SW quadrant). The solid orange line is the normalized seasonal mean of the BT anomalies in the SW quadrant for the annulus of radius ranging from 4–10° (Fig. 4.4). The dashed orange line is the normalized seasonal mean of the deep convection coverage for radius ranging from 4–10° (Fig. 4.5). The two orange lines are strongly correlated with each other ( $r = -0.88$ ). The ENSO and monsoon indices have modest but statistically significant correlations with both of the normalized monsoon tail indices. A more pronounced monsoon tail rainband is associated with an eastward-shifted ELI and a greater WNP monsoon index. The WNP monsoon index has slightly higher correlations with the monsoon tail indices than ENSO.

Figure 4.9 contrasts the vertical wind shear patterns in strong monsoon seasons and El Niño years against the shear patterns in weak monsoon seasons and La Niña years. Comparing Figs. 4.9 (e) versus (f) and (a) versus (b), the stronger monsoon/El Niño years have a greater longitudinal extent of easterly shear than weaker monsoon/La Niña years. With a more extended area of easterly shear, more TCs have a chance to experience the interaction of easterly VWS that consequently pushes convection westward. Thus, TCs are more likely to exhibit monsoon tail features in those seasons. The meridional shear does not show much interannual variability, regardless of ENSO phase or monsoon strength (Figs. 4.9 c, d, g, h). However, zonal shear has the strongest correlation, so it explains how both the monsoon index and ELI co-vary with the monsoon tail indices despite the monsoon index and the ELI not correlating well with each other (Fig. 4.8).

Figure 4.10 shows the distribution of the mean BT by quadrants depending on the ELI and the WNP monsoon index. Strong monsoon or El Niño years correspond to red circles in Fig. 4.8, and weak monsoon or La Niña years correspond to blue circles in Fig. 4.8. The remaining years (index between  $\pm 1$ ) are denoted as moderate years. First, as shown in Fig. 4.4, the SW quadrant



**Figure 4.8:** Time series of the normalized **(a)** ENSO Longitude Index (ELI) and the **(b)** Western North Pacific (WNP) monsoon index averaged for JJAS from 1980–2019. Normalized index values exceeding  $\pm 1$  standard deviation are denoted with red (positive) and blue (negative) circles. Orange lines indicate the normalized JJAS mean “monsoon tail” rainband anomaly over the WNP. For more details, refer to section 4.3.2.



**Figure 4.9:** Zonal and meridional deep-layer (200-850 hPa) vertical wind shear composit for the seasons that have anomalous (greater than  $\pm 1$  standard deviation) ENSO longitude index values (a, b, c, d) and western North Pacific monsoon index values (e, f, g, h).

has the coldest BT relative to the other three quadrants. Second, El Niño years have colder BTs in the SW quadrant than moderate ENSO or La Niña years, but the relationship was different in the NW and SE quadrants. Strong monsoon years give colder BTs in all quadrants than weak monsoon years, but the medium monsoon years have even colder mean and median BTs than strong monsoon years. The difference between eastward-shifted ELI years vs. westward-shifted ELI years or strong monsoon years vs. weak monsoon years is not large compared to differences between quadrants. The boxplots for the deep convection index were also examined and showed very similar trends as those displayed in Fig. 4.10.

Although the composite maps of shear patterns are very similar between the eastward-shifted ELI and strong monsoon years (Figs. 4.9 a and e) or the westward-shifted ELI and weak monsoon years (Figs. 4.9 b and f), there are some differences. In terms of spatial coverage, on average the eastward-shifted ELI years have a more extended area of easterly shear than strong monsoon years. However, in terms of shear magnitude, the strong monsoon years composite has a stronger easterly VWS than the eastward-shifted ELI years composite map at the same longitude ( $4 \text{ m s}^{-1}$  difference). These differences could be responsible for distinctive trends in the box plots mentioned above. Also, even for weak monsoon years or La Niña years, west of  $140^{\circ}\text{E}$  it is dominantly by northeasterly VWS (Fig. 4.9 b, d, f, h). Thus, it seems that the interannual variability of the monsoon tail feature is somewhat muted because there is always some monsoonal forcing and northeasterly VWS regardless of ENSO phase or monsoon intensity.

### 4.3.3 Subsequent tropical cyclogenesis from the "Monsoon tail" rainband

So far, we have examined the climatology and interannual variability of the monsoon tail. In this section, we investigate two particularly strong monsoon tail rainband cases: Jebi (2018) and Lingling (2019). Both Jebi and Lingling formed and intensified during the PISTON field campaign, so they were closely tracked by PISTON scientists. Their monsoon tail rainbands had reflectivity as strong as the reflectivity in the eyewalls. The rainbands became isolated from the TCs as the rainband stayed in the monsoonal flow region while the TCs moved northward. Then, the wide-spread convective area that was originally the rainband of Jebi or Lingling developed

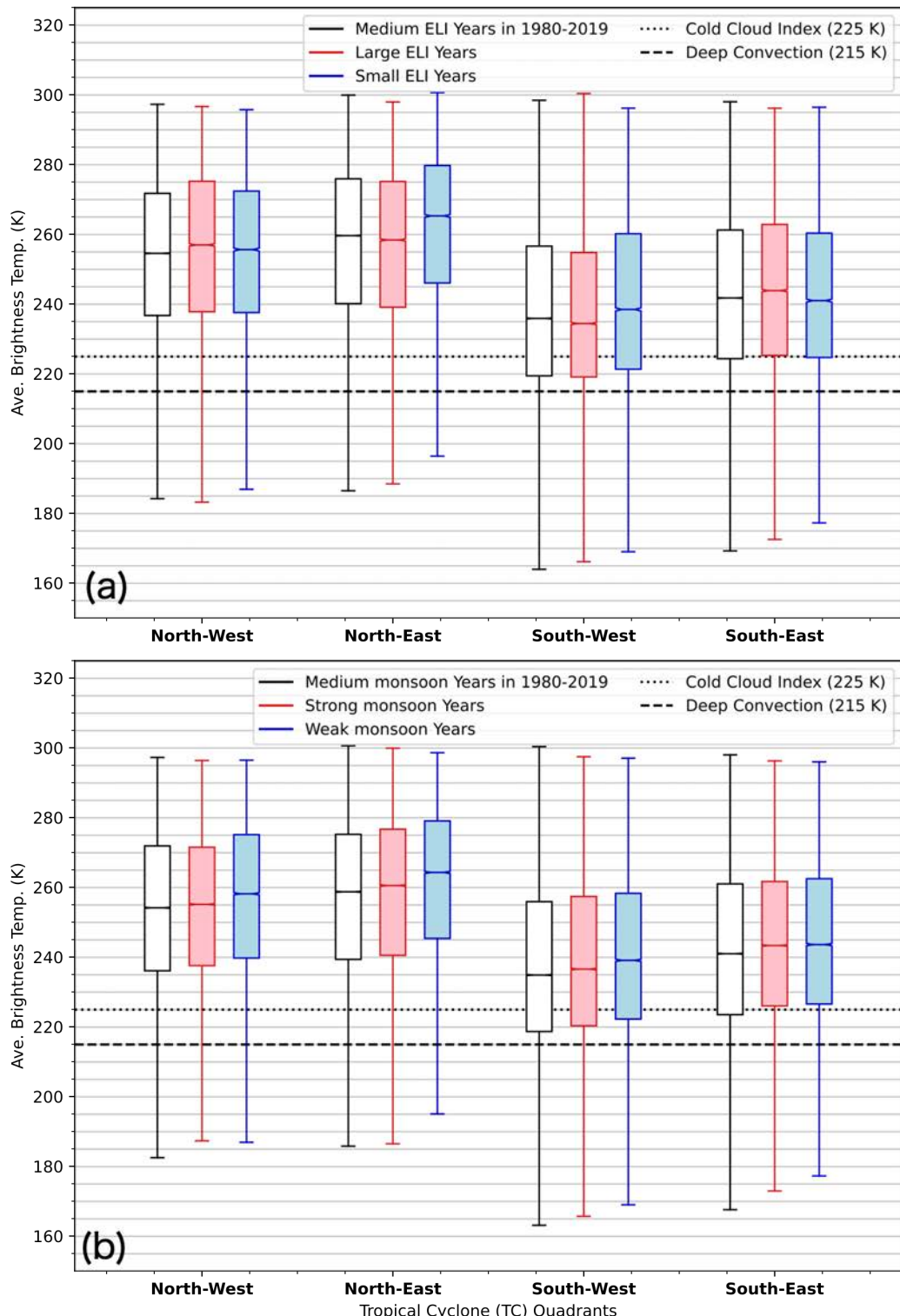


**Figure 4.10:** Boxplots of mean brightness for a radius range from  $4\text{--}10^\circ$  composed by TC quadrants and (a) the ENSO longitude index (ELI) or (b) the western North Pacific (WNP) monsoon index

low-level circulations of their own and exhibited the potential to become another TC. Figures 4.11 and 4.12 show the evolution of the low-level wind field and the Okubo-Weiss parameter (a measure of rotation over strain; Eq. 4.1) for Jebi-Invest 98W and Lingling-TD19, respectively.

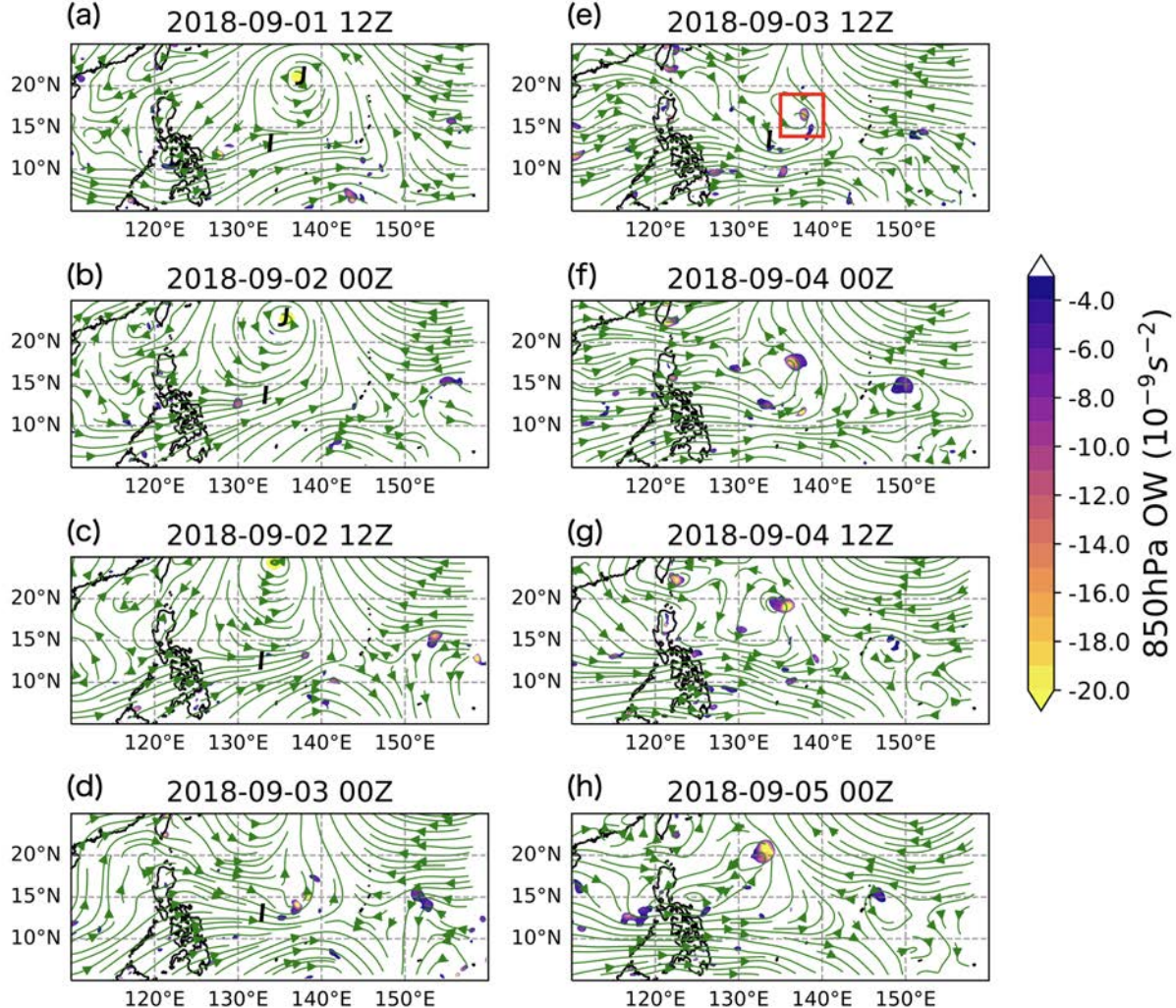


**Figure 4.11:** Okubo-Weiss parameter and streamlines at 850 hPa for 12-hourly observations from 01/09/2018 12 UTC to 05/09/2018 00 UTC. A ‘J’ marks the location of Super Typhoon Jebi, and an ‘I’ indicates the broad convective area tracked as Invest 98W (Fig. 4.2). The red  $5^\circ \times 5^\circ$  square in (b) marks the cross-section area in Fig. 4.13.

Invest 98W (formerly Jebi’s monsoon tail) recorded 35-40 knot gusts according to radiosonde data launched from the R/V Thompson and yielded more than 200 mm rainfall over the SeaPol ship-borne radar domain during September 2nd–3rd, 2018 (SeaPol and radiosonde data available

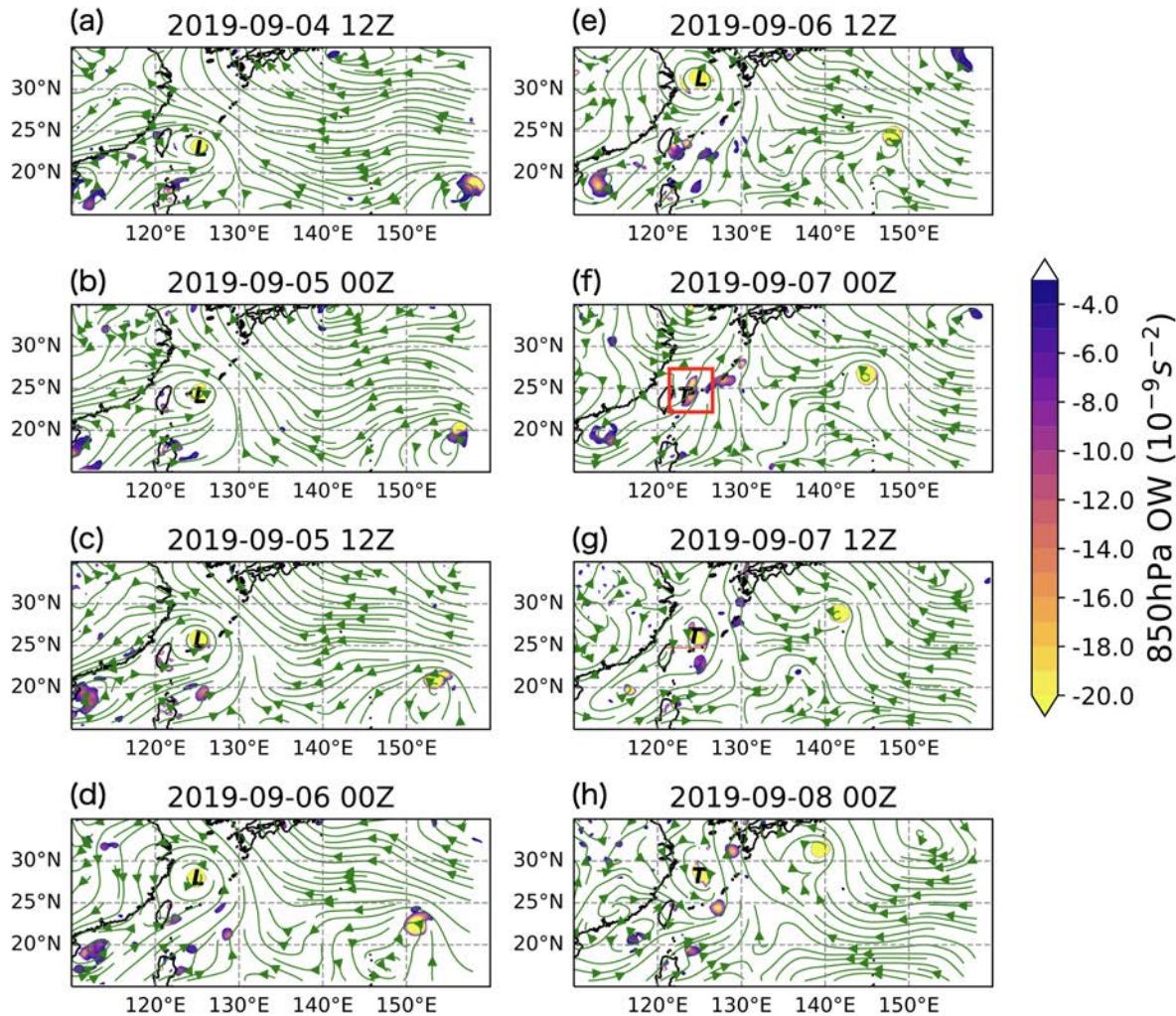


**Figure 4.12:** Okubo-Weiss parameter and streamlines at 850 hPa for 12-hourly observations from 04/09/2019 12 UTC to 08/09/2019 00 UTC. An 'L' marks the location of Typhoon Lingling, and a 'T' marks the location of TD19 that emerged from the monsoon tail rainband of Lingling. The red  $5^\circ \times 5^\circ$  square in (d) marks the cross-section area in Fig. 4.13.

at <https://radarmet.atmos.colostate.edu/piston/>). As shown in Fig. 4.2, Invest 98W had wide-spread deep convection separate from Jebi from September 1st to September 3rd. Invest 98W was located in the strong monsoon southwesterly regime. The area was originally predominated by weak southwesterlies but as Jebi was approaching, the southwesterlies were enhanced and extended farther to the east. Invest 98W managed to develop a small area of low-level rotation around  $13^{\circ}\text{N}$   $138^{\circ}\text{E}$ , which was about  $10^{\circ}$  separated from Jebi, at 12 UTC of September 2nd, 2018 (Fig. 4.11 c). The vorticity was collocated inside the convection from 00-12 UTC of September 3rd before convection dissipated on the 4th. After convection dissipated, vorticity remained inside the pouch of the low-level circulation for several days (Fig. 4.11 f-h).

Lingling's monsoon tail rainband was observed by the SeaPol radar on September 5th, 2019. Similar to Invest 98W's case, even after Lingling moved northward, organized convection lingered around eastern Taiwan where the monsoon southwesterlies were blowing. Some weak rotational elements appeared at 2019-09-06, 00 UTC around  $6^{\circ}$  southwest from Lingling (Fig. 4.12 d). One day later, more patches of small rotational elements were embedded in the southwesterlies east of Taiwan (Fig. 4.12 e). At 00 UTC of 2019-09-07, the system reached tropical depression intensity (TD19) as the vortices merged and became larger and intensified (Fig. 4.12 f). TD19 moved northeastward for the next couple of days and made landfall along the west coast of the Korean Peninsula on September 10th at 18 UTC. TD19 never reached tropical storm intensity; its maximum intensity was recorded at 00 UTC of September 8th with maximum sustained wind of 29 knots and minimum central sea-level pressure of 996 hPa.

For both cases, the monsoon tail rainband was characterized by persistent convection and developed a low-level circulation inside the convective area after it separated from the pre-existing TCs. The sea surface temperatures around both Invest 98W and TD19 were above  $28^{\circ}\text{C}$ , and the systems were located inside the wet westerly monsoon regime. Given the favorable thermodynamic environment, we asked why Invest 98W did not undergo tropical cyclogenesis and TD19 did not intensify beyond tropical depression strength.

Figure 4.13 shows vertical cross-sections of the vortex towers of TD19 and Invest 98W at the time of TD19's genesis (Fig. 4.12 d) and at the time when Invest 98W had the best chance of development with a closed low-level circulation collocated inside the widespread convective area (Fig. 4.11 b). There was strong vertical wind shear ( $>16 \text{ m s}^{-1}$  for 200–850 hPa deep-layer shear) around both TD19 and Invest 98W (see red contours in Fig. 4.13) collocated with dry air. The northerly VWS for TD19 and northeasterly VWS for Invest 98W came from the anticyclonic upper-level outflow of Typhoon Lingling and Typhoon Jebi, respectively. Both systems were vertically tilted on their downshear side, but the tilt magnitude of Invest 98W was much larger than that of TD19. The vortex tower of Invest 98W was tilted westward by larger than 300 km between 300–1000 hPa (Fig. 4.13 d). Since Invest 98W's vortex was so tilted, the cross-section at 138°E looks like a dwarf vortex tower only extending upward to 700 hPa (Fig. 4.13 c). The vortex tower of TD19 is also tilted to its downshear side (southward) but not as much as Invest 98W (Fig. 4.13 a). Strong VWS penetrated the core of the vortex tower for Invest 98W. Between 600–850 hPa, there was  $10 \text{ m s}^{-1}$  of VWS. On the other hand, the VWS around TD19 was confined to the upper-levels and did not appear to affect the vortex center directly. Invest 98W had stronger vorticity in its core, but TD19 had a wider area covered by rotation.

From observations of Fig. 4.13, VWS was likely the limiting factor for further development of TD19 and Invest 98W despite favorable thermodynamic conditions, and the VWS was in part produced by the pre-existing TC. We conclude that the likelihood of subsequent TC genesis from the monsoon tail rainband is low due to negative interaction with the pre-existing TC's outflow. We scrutinized possible TC genesis cases from the monsoon tail rainband by checking all TC genesis in the south of a pre-existing TC in the monsoon southwesterly regime over the WNP. The majority of the cases were related to ITCZ or monsoon trough breakdown that producing multiple TCs simultaneously or related to Vortex Rossby Wave energy dispersion (Li and Fu 2006), and we found no clear evidence of a monsoon tail leading to subsequent genesis in any case other than TD19 discussed above.

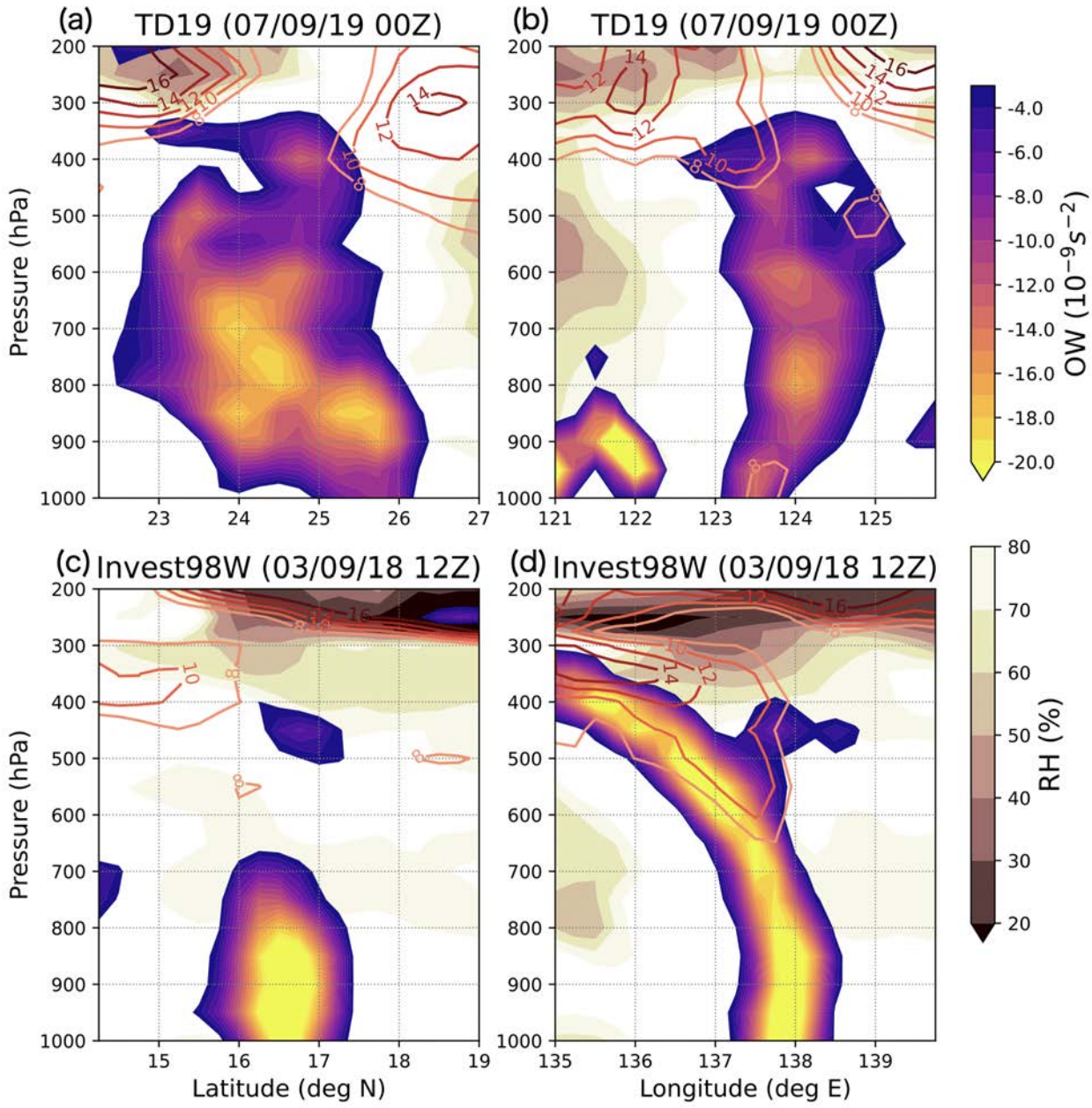


**Figure 4.13:** Meridional and zonal cross-sections of the vortex tower of (a), (b) TD19 at 0 UTC 07/09/2019 — the time when TD19 was declared as a tropical depression, (c), (d) Invest 98W at 12 UTC 03/09/2018 — the time when Invest 98W had the best chance of development with a closed low-level circulation inside the widespread convective area. The Okubo-Weiss (OW) parameter and Relative Humidity (RH) are in color, and vertical wind shear from 850 hPa winds are in red contours in a range of  $8-16 m s^{-1}$  magnitude from light red to dark red. The cross section area is marked with red squares in Figs. 4.11 and 4.12.

#### **4.4 Discussion and Conclusion**

This study investigated the monsoon tail rainband—an elongated strong rainband in the SW quadrant of TCs over the monsoonal area of the WNP—which was observed for the majority of TCs during the PISTON field campaign (2018–2019).

Here, we answer the three research questions that we raised in the Introduction. First, we found that enhanced convective activity in the SW quadrant is common from a 40-year composite analysis of all TCs in the monsoonal area of the WNP. The correlation analysis of brightness temperatures with the synoptic wind fields revealed that the monsoon tail rainband had the strongest correlation with zonal vertical wind shear. Low-level monsoon westerlies and low-level convergence appeared as secondary factors for the monsoon tail rainband. The monsoon tail rainband showed small interannual variability. This limited interannual variability was attributed to the WNP in the boreal summer always being characterized by northeasterly VWS, moist humidity, and warm SSTs that are conducive for an SW convective asymmetry even in less favorable La Niña or weak monsoon years. We have not looked at other TC basins to see if monsoon tail feature is common in the Atlantic or the East Pacific, but we can infer that it is unlikely because climatologically, the Atlantic has westerly VWS during the boreal summer, and the eastern North Pacific does not have distinct northeasterly VWS like the WNP (Finocchio and Majumdar 2017).

For the second question, the case studies and climatology suggest that higher humidity and background vorticity in the monsoon trough region (Fig. 4.7) may have helped the monsoon tail rainband to sustain convective activity even after it was detached from the pre-existing TC. The monsoon tail rainband index was correlated with weaker TC intensity and stronger VWS. Thus, VWS seems to be the primary factor shaping the convective asymmetry in the SW quadrant. Nam and Bell (2021) discussed complex multi-scale VWS interactions with an incipient tropical disturbance and showed that low- to mid-level VWS may actually help convection in developing disturbances better organize upscale and produce vorticity through the generation of horizontal vorticity. Then, moisture convergence from the southwesterly monsoonal flow would help the monsoon tail rainband to sustain its organization for a longer time, separate from the pre-existing TC.

The third question was on the subsequent TC genesis from the monsoon tail rainband. VWS may be helpful for upscale growth of the convective organization; however, VWS is detrimental in terms of tropical cyclogenesis. The pre-existing TCs are still nearby from the ex-monsoon tail rainband around  $6\text{--}10^\circ$  away, and the upper-level anticyclonic outflow of the TCs can amplify existing northeasterly VWS over the ex-monsoon tail rainband. Our inspection of possible monsoon tail-related TC genesis cases was not successful in finding more cases like TD19 spinning off from Linling's monsoon tail rainband. Thus, we conjecture that it is unlikely for a monsoon tail rainband to become a TC by itself even if the rainband shows some promising features such as a closed low-level circulation and persistent widespread convection due to the negative interaction with the outflow of the pre-existing TC.

The set up of Invest 98W comes close to the Weak sensitivity test in Chapter 3 in that it is a quite humid environment, but the vortex was not well established when it encountered the strong VWS. Based on our findings in Chapter 3, Invest 98W only achieved the first floor of "increased deep convective coverage over the broader circulation" but could not reach the vortex reformation nor vortex realignment process (see the pyramid diagram in Fig. 3.18). Comparing TD19 and Invest 98W as success and failure cases for TC genesis (although TD19 was a marginal TC genesis case), the vertical depth of VWS and the spatial scale of the vortex appeared as important differences between the two. VWS was more detrimental to Invest 98W than TD19 as the strong VWS extended to the mid-levels, directly penetrating the mid-level vortex center (Fig. 4.13), and disrupting TC development (Finocchio et al. 2016). TD19 had a much larger mid-level vortex than Invest 98W, and a larger mid-level vortex was shown to be advantageous for vortex realignment process under sheared environments in Chapter 3.

Chapter 2 showed that the vorticity generated through the convective life-cycle outlives the convection, and vorticity can be accumulated inside the closed circulation. Invest 98W also had vortices lingering around for a longer time after convection dissipated (Fig. 4.11). Hagupit (2008) had a structure somewhat similar to Invest 98W in that vortex was tilted, and convection was shifted to SW side from the vortex center (Figs. 2.3 and 2.13), but Hagupit (2008) survived through strong

VWS and eventually intensified to Typhoon as it left outside of the strong shear area (Fig. 2.6). One difference is that Hagupit (2008) developed from an easterly wave, thus it was constantly moving westward; Invest 98W was more stagnant in the monsoon southwesterly regime, thus VWS was more of a persistent influence over the system.

Our methodology of monsoon tail rainband detection has a limitation in that we did not distinguish each cell's convective organization but looked at the composite of BT. We had two different metrics that included mean BT in the area and the convective coverage in the SW quadrant of TCs, but still, this method does not track individual monsoon tail rainbands. For some cases, there could be some noises or unrelated convective systems in the SW quadrant that were detected as a monsoon tail rainband. For future work, we could employ the objective tracking of the convective clusters following the methodology of Dias et al. (2012). Also, for the monsoon index, we note that the monsoon trough has intraseasonal variability on top of interannual variability, but as Molinari and Vollaro (2013) pointed out, the intraseasonal variability signal is highly affected by TCs and the Madden-Julian oscillation. Thus, we decided to use the seasonal mean monsoon index to better understand interannual variability.

# **Chapter 5**

## **Conclusions**

This research investigated factors that contribute to the uncertainty of tropical cyclogenesis, namely, vertical wind shear (VWS), environmental humidity, and the structure of the precursor vortex. The research aimed to identify the sources of increased uncertainty of tropical cyclogenesis in marginally favorable environments through the understanding of the key multi-scale precursors leading to tropical cyclogenesis in such environments. Based on the results herein, the uncertainty can be largely attributed to the probabilistic characteristics of precursor events lining up together before TC genesis (Chapter 3). In an extremely favorable or hostile environment, the success rate of each precursor event is either very high or very low, so the probability of ultimate TC genesis is skewed to 1 or 0. However, in a marginal environment, the success rate is moderate such that a TC can undergo TC genesis with a first trial, or it could exhibit robust signals such as deep convective organization or low-level closed circulation but still fail to intensify. Later, some systems could develop into a TC after more trials in a more favorable environment (e.g., Hagupit (2008) in Chapter 2), or it could miss the window of opportunity and dissipate as the environment becomes more hostile (e.g., Invest 98W in Chapter 4).

Based on results from the controlled experiments in Chapter 3, we proposed a theoretical pyramid framework (Fig. 3.18), in which a pre-depression starts at the bottom and works its way up toward TC genesis. The successfully developing ensemble members in the sheared and dry environments shared common precursors regardless of different environmental setups. First, inside their low-level circulations, deep convection emerged over a wider area. Second, a new smaller scale mid-level vortex formed inside the deep convection where the pre-existing mid-level vortex was carried away by VWS. Third, the mid-level vortex and low-level vortex went through a vertical alignment process. Fourth, with sustained vortex alignment, convection organized near the

low-level center. Fifth, central pressure fell and wind speed increased; and the system reached tropical cyclone intensity.

Even for the failed genesis cases, most of the simulations showed evidence of increasing deep convective coverage over the broader circulation. In the most uncertain environments, with a low-level centered vortex of  $15 \text{ m s}^{-1}$  maximum wind speed in a moderately sheared and dry environment, the number of cycles for precursor events to line up together before TC genesis had a wide range from 2 to 8. The bifurcation points between successful and failed trials were primarily found in the vortex alignment process; all ensemble members in the Main Set of simulations showed deep convection, which reformed a mid-level vortex, but for the failed cycles, the new mid-level vortex could not sustain vertical alignment with the low-level center and was carried away by VWS shortly again. For a weaker vortex or mid-level centered vortex, the bifurcation points appeared to be in the mid-level vortex reformation process; a mid-level vortex was not reformed, and vortex tilt kept increasing for the non-developing ensemble members. These results can be interpreted from the perspective of an 'Anna Karenina principle': *"All happy families are alike; each unhappy family is unhappy in its own way."*

The case study of Hagupit (2008) in Chapter 2 and the climatological study of the monsoon tail rainband in Chapter 4 shed light on the multifaceted roles of VWS in different spatiotemporal scales. Even though it was evident that the strong deep-layer VWS had detrimental impacts on TC development, depending on the depth of shear and thermodynamic environments, VWS could also help convective organization inside an incipient pre-depression. In Chapter 2, high-resolution radar observations revealed that low-level and mid-level VWS in meso-beta scale supported the linear convective organization and vorticity generation through providing horizontal vorticity that can be tilted to vertical vorticity through convective updrafts. In Chapter 4, climatological VWS in the WNP enhanced convective organization in the southwestern quadrant of TCs along with the moisture convergence of monsoon westerlies.

Ooyama (1982) said, "History tells us, at least, that understanding the problems to be solved is as important as solving them." This dissertation does not claim to solve the fundamental TC

genesis problem, but it clarifies some sources of uncertainty in which process the developing and non-developing systems diverge the most. More studies of high-resolution observations for a pre-depression and surrounding environment for systems that are actively interacting with VWS will be needed. More research flights during the pre-genesis stage when genesis is uncertain but possible (i.e., bifurcation point), such as September 14th, 2008 over Hagupit (Chapter 2), would open the door to directly investigate the bifurcation points with high-resolution observations, verifying our findings from numerical simulations. Carefully designed ensemble modeling studies focusing on the timing of bifurcation points among the ensemble members would also advance the implications of our results. It is worthwhile to explore how choices of radiation and microphysics schemes, the vertical depth of VWS, and the size of the initial vortex affect the uncertainty of TC genesis and test if our hypothesis and theoretical diagram hold true regardless of the different environments.

## References

- Aiyyer, A., Z. Wang, R. McTaggart-Cowan, and S. K. R. Bhowmik, 2014: *Cyclogenesis: review of latest science*, chap. 2.1. 13, World Meteorological Organization, [Available online at [https://www.wmo.int/pages/prog/arep/wwrp/new/documents/IWTC\\_VIII\\_Topic2\\_1\\_Cyclogenesis\\_Final.pdf](https://www.wmo.int/pages/prog/arep/wwrp/new/documents/IWTC_VIII_Topic2_1_Cyclogenesis_Final.pdf).].
- Alland, J. J., B. H. Tang, and K. L. Corbosiero, 2017: Effects of midlevel dry air on development of the axisymmetric tropical cyclone secondary circulation. *J. Atmos. Sci.*, doi: 10.1175/JAS-D-16-0271.1.
- Alland, J. J., B. H. Tang, K. L. Corbosiero, and G. H. Bryan, 2021: Combined effects of midlevel dry air and vertical wind shear on tropical cyclone development. part i: Downdraft ventilation. *Journal of the Atmospheric Sciences*, **78** (3), 763 – 782, doi: 10.1175/JAS-D-20-0054.1.
- Au-Yeung, A. Y. M., and C.-Y. Tam, 2018: Dispersion characteristics and circulation associated with boreal summer westward travelling mixed rossby-gravity wave-like disturbances. *J. Atmos. Sci.*, **75**, 513–533.
- Bell, M. M., and M. T. Montgomery, 2010: Sheared deep vortical convection in pre-depression Hagupit during TCS08. *Geophysical Research Letters*, doi: 10.1029/2009GL042313.
- Bell, M. M., and M. T. Montgomery, 2019: Mesoscale processes during the genesis of hurricane karl (2010). *Journal of the Atmospheric Sciences*, **76** (8), 2235–2255, doi: 10.1175/JAS-D-18-0161.1.
- Bell, M. M., M. T. Montgomery, and K. A. Emanuel, 2012: Air–Sea Enthalpy and Momentum Exchange at Major Hurricane Wind Speeds Observed during CBLAST. *Journal of the Atmospheric Sciences*, doi: 10.1175/JAS-D-11-0276.1.

Bister, M., and K. A. Emanuel, 1997: The genesis of hurricane guillermo: Texmex analyses and a modeling study. *Mon. Weather Rev.*, doi: 10.1175/1520-0493(1997)125<2662:TGOHGT>2.0.CO;2.

Bracken, W. E., and L. F. Bosart, 2000: The role of synoptic-scale flow during tropical cyclogenesis over the north atlantic ocean. *Monthly Weather Review*, **128** (2), 353–376, doi: 10.1175/1520-0493(2000)128<0353:TROSSF>2.0.CO;2.

Briegel, L. M., and W. M. Frank, 1997: Large-scale influences on tropical cyclogenesis in the western north pacific. *Monthly Weather Review*, **125**, 1397–1413.

Chang, M., C.-H. Ho, J. C. L. Chan, M.-S. Park, S.-W. Son, and J. Kim, 2019: The tropical transition in the western north pacific: The case of tropical cyclone peipah (2007). *Journal of Geophysical Research: Atmospheres*, **124** (10), 5151–5165, doi: 10.1029/2018JD029446.

Chavas, D. R., K. A. Reed, and J. A. Knaff, 2017: Physical understanding of the tropical cyclone wind-pressure relationship. *Nat. Commun.*, **8**, 1360.

Chen, T.-C., S.-Y. Wang, M.-C. Yen, and A. J. Clark, 2008: Are tropical cyclones less effectively formed by easterly waves in the western north pacific than in the north atlantic? *Monthly Weather Review*, **136** (11), 4527 – 4540, doi: 10.1175/2008MWR2149.1.

Chen, T.-C., and J.-H. Yoon, 2000: Interannual variation in indochina summer monsoon rainfall: Possible mechanism. *Journal of Climate*, **13**, 1979–1986.

Chen, X., Y. Wang, J. Fang, and M. Xue, 2018: A Numerical Study on Rapid Intensification of Typhoon Vicente (2012) in the South China Sea. Part II: Roles of Inner-Core Processes. *Journal of the Atmospheric Sciences*, **75** (1), 235–255, doi: 10.1175/JAS-D-17-0129.1.

Chudler, K., and S. A. Rutledge, 2021: The coupling between convective variability and large-scale flow patterns observed during piston 2018–19. *Journal of Climate*, **34** (17), 7199 – 7218, doi: 10.1175/JCLI-D-20-0785.1.

Corbosiero, K. L., and J. Molinari, 2002: The Effects of Vertical Wind Shear on the Distribution of Convection in Tropical Cyclones. *Monthly Weather Review*, **130** (8), 2110–2123, doi: 10.1175/1520-0493(2002)130<2110:TEOVWS>2.0.CO;2.

Courtney, J., and J. A. Knaff, 2009: Adapting the knaff and zehr wind-pressure relationship for operational use in tropical cyclone warning centres. *Australian Meteorological and Oceanographic Journal*, **58**(3), 167–179.

Dare, R. A., and J. L. McBride, 2011: The threshold sea surface temperature condition for tropical cyclogenesis. *J. Clim.*, doi: 10.1175/JCLI-D-10-05006.1.

Davis, C. A., 2015: The Formation of Moist Vortices and Tropical Cyclones in Idealized Simulations. *Journal of the Atmospheric Sciences*, **72** (9), 3499–3516, doi: 10.1175/JAS-D-15-0027.1.

Davis, C. A., and D. A. Ahijevych, 2013: Thermodynamic Environments of Deep Convection in Atlantic Tropical Disturbances. *Journal of the Atmospheric Sciences*, **70** (7), 1912–1928, doi: 10.1175/JAS-D-12-0278.1.

Davis, C. A., and L. F. Bosart, 2003: Baroclinically Induced Tropical Cyclogenesis. *Monthly Weather Review*, **131** (11), 2730–2747, doi: 10.1175/1520-0493(2003)131<2730:BITC>2.0.CO;2.

Davis, C. A., and T. J. Galarneau, 2009: The vertical structure of mesoscale convective vortices. *Journal of the Atmospheric Sciences*, **66** (3), 686–704, doi: 10.1175/2008JAS2819.1.

DeHart, J. C., J. Houze, Robert A., and R. F. Rogers, 2014: Quadrant Distribution of Tropical Cyclone Inner-Core Kinematics in Relation to Environmental Shear. *Journal of the Atmospheric Sciences*, **71** (7), 2713–2732, doi: 10.1175/JAS-D-13-0298.1.

Dias, J., S. N. Tulich, and G. N. Kiladis, 2012: An object-based approach to assessing the organization of tropical convection. *Journal of the Atmospheric Sciences*, **69**(8), 2488–2504.

Dunion, J. P., 2011: Rewriting the climatology of the tropical north atlantic and caribbean sea atmosphere. *J. Climate*, **24**, 893–908.

Dunkerton, T. J., M. T. Montgomery, and Z. Wang, 2009: Tropical cyclogenesis in a tropical wave critical layer: easterly waves. *Atmospheric Chemistry and Physics*, **9 (15)**, 5587–5646, doi: 10.5194/acp-9-5587-2009.

Elsberry, R. L., and P. A. Harr, 2008: Tropical Cyclone Structure (TCS08) Field Experiment Science Basis, Observational Platforms, and Strategy. *Asia-Pacific Journal of Atmospheric Sciences*.

Fang, J., and F. Zhang, 2011: Evolution of multiscale vortices in the development of hurricane dolly (2008). *Journal of the Atmospheric Sciences*, **68 (1)**, 103–122, doi: 10.1175/2010JAS3522.1.

Finocchio, P. M., and S. J. Majumdar, 2017: A statistical perspective on wind profiles and vertical wind shear in tropical cyclone environments of the northern hemisphere. *Monthly Weather Review*, **145 (1)**, 361 – 378, doi: 10.1175/MWR-D-16-0221.1.

Finocchio, P. M., S. J. Majumdar, D. S. Nolan, and M. Iskandarani, 2016: Idealized tropical cyclone responses to the height and depth of environmental vertical wind shear. *Monthly Weather Review*, **144 (6)**, 2155–2175, doi: 10.1175/MWR-D-15-0320.1.

Fischer, M. S., B. H. Tang, and K. L. Corbosiero, 2019: A Climatological Analysis of Tropical Cyclone Rapid Intensification in Environments of Upper-Tropospheric Troughs. *Monthly Weather Review*, **147 (10)**, 3693–3719, doi: 10.1175/MWR-D-19-0013.1.

Foerster, A. M., M. M. Bell, P. A. Harr, and S. C. Jones, 2014: Observations of the eyewall structure of typhoon sinlaku (2008) during the transformation stage of extratropical transition. *Monthly Weather Review*, **142 (9)**, 3372–3392, doi: 10.1175/MWR-D-13-00313.1.

Fu, R., A. D. D. Genio, and W. B. Rossow, 1990: Behavior of deepconvective clouds in the tropical pacific deduced from isccpradiances. *J. Climate*, **3**, 1129–1152.

Goni, G., and Coauthors, 2009: Applications of satellite-derived ocean measurements to tropical cyclone intensity forecasting. *Oceanography*, doi: 10.5670/oceanog.2009.78.

Gray, W. M., 1968: Global view of the origin of tropical disturbances and storms. *Mon. Weather Rev.*, doi: 10.1175/1520-0493(1968)096<0669:GVOTOO>2.0.CO;2.

Gray, W. M., 1979: *Hurricanes: Their Formation, Structure and likely Role in the Tropical Circulation*, 155–218. James Glaisher House.

Hendricks, E. A., M. T. Montgomery, and C. A. Davis, 2004: The role of “vortical” hot towers in the formation of tropical cyclone diana (1984). *Journal of the Atmospheric Sciences*, **61** (11), 1209–1232, doi: 10.1175/1520-0469(2004)061<1209:TROVHT>2.0.CO;2.

Hersbach, H., and Coauthors, 2020: The ERA5 global reanalysis. *Quart. J. Roy. Meteor. Soc.*, **146** (730), 1999–2049, doi: 10.1002/qj.3803.

Holland, G. J., 1995: Scale interaction in the western pacific monsoon. *Meteor. Atmos. Phys.*, **56**, 57–79.

Holton, J., 2004: *An Introduction to Dynamic Meteorology*. Elsevier Science.

Hong, S.-Y., J. Dudhia, and S.-H. Chen, 2004: A revised approach to ice microphysical processes for the bulk parameterization of clouds and precipitation. *Mon. Wea. Rev.*, **132**, 103–120.

Hong, S.-Y., Y. Noh, and J. Dudhia, 2006: A new vertical diffusion package with an explicit treatment of entrainment processes. *Mon. Wea. Rev.*, **134**, 2318–2341.

Houze Jr., R. A., 2004: Mesoscale convective systems. *Reviews of Geophysics*, **42** (4), doi: 10.1029/2004RG000150.

James, R. P., and P. M. Markowski, 2010: A numerical investigation of the effects of dry air aloft on deep convection. *Monthly Weather Review*, **138** (1), 140 – 161, doi: 10.1175/2009MWR3018.1.

Johnson, R. H., S. L. Aves, P. E. Ciesielski, and T. D. Keenan, 2005: Organization of oceanic convection during the onset of the 1998 east asian summer monsoon. *Monthly Weather Review*, **133**, 131—148, doi: 10.1175/MWR-2843.1.

Johnson, R. H., T. M. Rickenbach, S. A. Rutledge, P. E. Ciesielski, and W. H. Schubert, 1999: Trimodal characteristics of tropical convection. *Journal of Climate*, **12** (8), 2397–2418, doi: 10.1175/1520-0442(1999)012<2397:TCOTC>2.0.CO;2.

Jones, S. C., 1995: The evolution of vortices in vertical shear. i: Initially barotropic vortices. *Quarterly Journal of the Royal Meteorological Society*, **121** (524), 821–851, doi: 10.1002/qj.49712152406.

Kilroy, G., R. K. Smith, and U. Wissmeier, 2014: Tropical convection: The effects of ambient vertical and horizontal vorticity. *Quarterly Journal of the Royal Meteorological Society*, doi: 10.1002/qj.2261.

Klotzbach, P. J., M. M. Bell, S. G. Bowen, E. J. Gibney, K. R. Knapp, and C. J. Schreck, 2020: Surface pressure a more skillful predictor of normalized hurricane damage than maximum sustained wind. *Bulletin of the American Meteorological Society*, **101** (6), E830 – E846, doi: 10.1175/BAMS-D-19-0062.1.

Knaff, J. A., and R. M. Zehr, 2007: Reexamination of tropical cyclone pressure wind relationships. *Wea. Forecasting*, **22**(1), 71–88.

Knapp, K. R., 2014: Noaa climate data record (cdr) of gridded satellite data from isccp b1 (gridsat-b1) infrared channel brightness temperature, version 2. NOAA National Centers for Environmental Information, access date: 13/09/2020, doi: 10.7289/V59P2ZKR.

Knapp, K. R., H. J. Diamond, J. P. Kossin, M. C. Kruk, and C. J. Schreck, 2018: International best track archive for climate stewardship (ibtracs) project, version 4. Data NOAA National Centers for Environmental Information, <https://www.ncdc.noaa.gov/ibtracs/index.php?name=ib-v4-access>, doi: 10.25921/82ty-9e16.

- Knapp, K. R., M. C. Kruk, D. H. Levinson, H. J. Diamond, and C. J. Neumann, 2010: The international best track archive for climate stewardship (ibtracs): Unifying tropical cyclone best track data. *Bulletin of the American Meteorological Society*, **91**, 363–376, doi: 10.1175/2009BAMS2755.1.
- Komaromi, W. A., 2013: An Investigation of Composite Dropsonde Profiles for Developing and Nondeveloping Tropical Waves during the 2010 PREDICT Field Campaign. *Journal of the Atmospheric Sciences*, **70** (2), 542–558, doi: 10.1175/JAS-D-12-052.1.
- LeMone, M. A., E. J. Zipser, and S. B. Trier, 1998: The role of environmental shear and thermodynamic conditions in determining the structure and evolution of mesoscale convective systems during toga coare. *Journal of the Atmospheric Sciences*, **55** (23), 3493–3518, doi: 10.1175/1520-0469(1998)055<3493:TROESA>2.0.CO;2.
- Li, T., and B. Fu, 2006: Tropical cyclogenesis associated with rossby wave energy dispersion of a preexisting typhoon. part i: Satellite data analyses. *J. Atmos. Sci.*, **63**, 1377–1389.
- Lin, I. I., G. J. Goni, J. A. Knaff, C. Forbes, and M. M. Ali, 2013: Ocean heat content for tropical cyclone intensity forecasting and its impact on storm surge. *Nat. Hazards*, doi: 10.1007/s11069-012-0214-5.
- Lorenz, E. N., 1969: The predictability of a flow which possesses many scales of motion. *Tellus*, **21** (3), 289–307, doi: 10.1111/j.2153-3490.1969.tb00444.x.
- McTaggart-Cowan, R., J. Galarneau, Thomas J., L. F. Bosart, R. W. Moore, and O. Martius, 2013: A Global Climatology of Baroclinically Influenced Tropical Cyclogenesis\*. *Monthly Weather Review*, **141** (6), 1963–1989, doi: 10.1175/MWR-D-12-00186.1.
- Melhauser, C., and F. Zhang, 2012: Practical and intrinsic predictability of severe and convective weather at the mesoscales. *J. Atmos. Sci.*, 3350–3371.

Molinari, J., P. Dodge, D. Vollaro, K. L. Corbosiero, and F. Marks, 2006: Mesoscale aspects of the downshear reformation of a tropical cyclone. *Journal of the Atmospheric Sciences*, **63** (1), 341–354, doi: 10.1175/JAS3591.1.

Molinari, J., and D. Vollaro, 2013: What percentage of western north pacific tropical cyclones form within the monsoon trough? *Monthly Weather Review*, **141** (2), 499 – 505, doi: 10.1175/MWR-D-12-00165.1.

Montgomery, M. T., M. E. Nicholls, T. A. Cram, and A. B. Saunders, 2006: A Vortical Hot Tower Route to Tropical Cyclogenesis. *Journal of the Atmospheric Sciences*, doi: 10.1175/JAS3604.1.

Montgomery, M. T., and Coauthors, 2012: The pre-depression investigation of cloud-systems in the tropics (PREDICT) experiment: Scientific basis, new analysis tools, and some first results. *Bulletin of the American Meteorological Society*, doi: 10.1175/BAMS-D-11-00046.1.

Moon, Y., and D. S. Nolan, 2010: Do gravity waves transport angular momentum away from tropical cyclones? *J. Atmos. Sci.*, **67**, 117–135.

Nakazawa, T., 1988: Tropical super clusters within intraseasonal variations over the western pacific. *J. Meteor. Soc. Japan*, **66**, 823–839.

Nam, C. C., and M. M. Bell, 2021: Multiscale shear impacts during the genesis of hagupit (2008). *Monthly Weather Review*, **149** (2), 551 – 569, doi: 10.1175/MWR-D-20-0133.1.

National Research Council, 2004: *Climate Data Records from Environmental Satellites: Interim Report*. The National Academies Press, Washington, DC, doi: 10.17226/10944.

Nguyen, L. T., and J. Molinari, 2015: Simulation of the downshear reformation of a tropical cyclone. *Journal of the Atmospheric Sciences*, **72** (12), 4529–4551, doi: 10.1175/JAS-D-15-0036.1.

Nolan, D., and M. McGauley, 2012: *Tropical cyclogenesis in wind shear: Climatological relationships and physical processes*, 1–36. Nova Science Publishers, Inc.

Nolan, D. S., E. D. Rappin, and K. A. Emanuel, 2007: Tropical cyclogenesis sensitivity to environmental parameters in radiative–convective equilibrium. *Q. J. R. Meteorol. Soc.*, **133**, 2085–2107, doi: 10.1002/qj.170.

Ooyama, K., 1969: Numerical Simulation of the Life Cycle of Tropical Cyclones. *Journal of the Atmospheric Sciences*, **26** (1), 3–40, doi: 10.1175/1520-0469(1969)026<0003:NSOTLC>2.0.CO;2.

Ooyama, K. V., 1982: Conceptual evolution of the theory and modeling of the tropical cyclone. *J. Meteor. Soc. Japan*, doi: 10.2151/jmsj1965.60.1\_369.

Palmen, E. H., 1948: On the formation and structure of tropical cyclones. *Geophysica*, **3**, 26–38.

Pendergrass, A. G., and H. E. Willoughby, 2009: Diabatically induced secondary flows in tropical cyclones. part i: Quasi-steady forcing. *Monthly Weather Review*, **137** (3), 805–821, doi: 10.1175/2008MWR2657.1.

Peng, M. S., B. Fu, T. Li, and D. E. Stevens, 2012: Developing versus nondeveloping disturbances for tropical cyclone formation. part i: North atlantic. *Monthly Weather Review*, **140** (4), 1047–1066, doi: 10.1175/2011MWR3617.1.

Pytharoulis, I., and C. Thorncroft, 1999: The low-level structure of african easterly waves in 1995. *Monthly Weather Review*, **127** (10), 2266–2280, doi: 10.1175/1520-0493(1999)127<2266:TLLSOA>2.0.CO;2.

Raymond, D., and S. L. Sessions, 2014: Tropical cyclogenesis and mid-level vorticity. *Australian Meteorological and Oceanographic Journal*, **64**, 11–25.

Raymond, D. D. J., C. López-Carrillo, and L. L. Cavazos, 1998: Case-studies of developing east pacific easterly waves. *Quarterly Journal of the Royal Meteorological Society*, **124** (550), 2005–2034, doi: 10.1002/qj.49712455011.

Raymond, D. J., and H. Jiang, 1990: A theory for long-lived mesoscale convective systems. *Journal of the Atmospheric Sciences*, **47** (24), 3067–3077, doi: 10.1175/1520-0469(1990)047<3067:ATFLLM>2.0.CO;2.

Raymond, D. J., and S. L. Sessions, 2007: Evolution of convection during tropical cyclogenesis. *Geophys. Res. Lett.*, doi: 10.1029/2006GL028607.

Reasor, P. D., and M. T. Montgomery, 2015: Evaluation of a heuristic model for tropical cyclone resilience. *Journal of the Atmospheric Sciences*, **72** (5), 1765–1782, doi: 10.1175/JAS-D-14-0318.1.

Reasor, P. D., M. T. Montgomery, and L. D. Grasso, 2004a: A new look at the problem of tropical cyclones in vertical shear flow: Vortex resiliency. *Journal of the Atmospheric Sciences*, **61** (1), 3–22, doi: 10.1175/1520-0469(2004)061<0003:ANLATP>2.0.CO;2.

Reasor, P. D., M. T. Montgomery, and L. D. Grasso, 2004b: A new look at the problem of tropical cyclones in vertical shear flow: Vortex resiliency. *Journal of the Atmospheric Sciences*, **61** (1), 3 – 22, doi: 10.1175/1520-0469(2004)061<0003:ANLATP>2.0.CO;2.

Reed, R. J., and E. E. Recker, 1971: Structure and properties of synoptic-scale wave disturbances in the equatorial western pacific. *Journal of the Atmospheric Sciences*, **28** (7), 1117–1133, doi: 10.1175/1520-0469(1971)028<1117:SAPOSS>2.0.CO;2.

Riehl, H., and R. J. Shafer, 1944: The recurvature of tropical storms. *J. Meteorol.*, **1**, 42–54, doi: 10.1175/1520-0469(1944)001<0001:TROTS>2.0.CO;2.

Rienecker, M., and Coauthors, 2008: *The GEOS-5 Data Assimilation System - Documentation of Versions 5.0.1, 5.1.0, and 5.2.0*, 1–97. NASA.

Rios-Berrios, R., 2020: Impacts of radiation and cold pools on the intensity and vortex tilt of weak tropical cyclones interacting with vertical wind shear. *Journal of the Atmospheric Sciences*, **77** (2), 669 – 689, doi: 10.1175/JAS-D-19-0159.1.

Rios-Berrios, R., C. A. Davis, and R. D. Torn, 2018: A hypothesis for the intensification of tropical cyclones under moderate vertical wind shear. *Journal of the Atmospheric Sciences*, **75** (12), 4149–4173, doi: 10.1175/JAS-D-18-0070.1.

Rios-Berrios, R., and R. D. Torn, 2017: Climatological analysis of tropical cyclone intensity changes under moderate vertical wind shear. *Monthly Weather Review*, **145** (5), 1717–1738, doi: 10.1175/MWR-D-16-0350.1.

Ritchie, E. A., and G. J. Holland, 1999: Large-scale patterns associated with tropical cyclogenesis in the western pacific. *Mon. Wea. Rev.*, doi: 10.1175/1520-0493(1999)127<2027:LSPAWT>2.0.CO;2.

Schecter, D. A., and M. T. Montgomery, 2003: On the symmetrization rate of an intense geophysical vortex. *Dynamics of Atmospheres and Oceans*, **37** (1), 55–88, doi: 10.1016/S0377-0265(03)00015-0.

Serra, Y. L., G. N. Kiladis, and M. F. Cronin, 2008: Horizontal and Vertical Structure of Easterly Waves in the Pacific ITCZ. *Journal of the Atmospheric Sciences*, **65**, 1266–1284, doi: 10.1175/2007JAS2341.1.

Shen, C., 2015: Analysis of detrended time-lagged cross-correlation between two nonstationary time series. *Physics Letters A*, **379** (7), 680–687, doi: <https://doi.org/10.1016/j.physleta.2014.12.036>.

Skamarock, W. C., and Coauthors, 2008: A description of the advanced research wrf version 3. Tech. rep., University Corporation for Atmospheric Research. doi: 10.5065/D68S4MVH.

Sobel, A. H., and C. S. Bretherton, 1999: Development of synoptic-scale disturbances over the summertime tropical north-west pacific. *J. Atmos. Sci.*, **56**, 3106–3127.

Sobel, A. H., J. Sprintall, E. D. Maloney, Z. K. Martin, S. Wang, S. P. de Szoeke, B. C. Trabing, and S. A. Rutledge, 2021: Large-scale state and evolution of the atmosphere and ocean during piston 2018. *Journal of Climate*, **34** (12), 5017 – 5035, doi: 10.1175/JCLI-D-20-0517.1.

Takahashi, H. G., H. Fujinami, T. Yasunari, J. Matsumoto, and S. Baimoung, 2015: Role of tropical cyclones along the monsoon trough in the 2011 thai flood and interannual variability. *Journal of Climate*, **28**(4), 1465–1476.

Tang, B., and K. Emanuel, 2010: Midlevel Ventilation's Constraint on Tropical Cyclone Intensity. *Journal of the Atmospheric Sciences*, **67** (6), 1817–1830, doi: 10.1175/2010JAS3318.1.

Tang, B., and K. Emanuel, 2012: Sensitivity of tropical cyclone intensity to ventilation in an axisymmetric model. *Journal of the Atmospheric Sciences*, **69** (8), 2394–2413, doi: 10.1175/JAS-D-11-0232.1.

Tang, B. H., and Coauthors, 2020: Recent advances in research on tropical cyclogenesis. *Tropical Cyclone Research and Review*, **9** (2), 87–105, doi: 10.1016/j.tcrr.2020.04.004.

Tao, D., 2015: Dynamics and predictability of tropical cyclones under vertical wind shear. Ph.D. thesis, The Pennsylvania State University.

Tao, D., and F. Zhang, 2014a: Effect of environmental shear, sea-surface temperature, and ambient moisture on the formation and predictability of tropical cyclones: An ensemble-mean perspective. *Journal of Advances in Modeling Earth Systems*, **6** (2), 384–404, doi: 10.1002/2014MS000314.

Tao, D., and F. Zhang, 2014b: Effect of environmental shear, sea-surface temperature, and ambient moisture on the formation and predictability of tropical cyclones: An ensemble-mean perspective. *J. Adv. Model. Earth Syst.*, **6**, 384–404.

Tao, D., and F. Zhang, 2015: Effects of vertical wind shear on the predictability of tropical cyclones: Practical versus intrinsic limit. *J. Adv. Model. Earth Syst.*, **7**, 1534–1553.

Van Sang, N., R. K. Smith, and M. T. Montgomery, 2008: Tropical-cyclone intensification and predictability in three dimensions. *Quarterly Journal of the Royal Meteorological Society*, **134** (632), 563–582, doi: 10.1002/qj.235.

- Vigh, J. L., and W. H. Schubert, 2009: Rapid development of the tropical cyclone warm core. *Journal of the Atmospheric Sciences*, **66** (11), 3335–3350, doi: 10.1175/2009JAS3092.1.
- Wang, B., Z. Wu, J. Li, J. Liu, C.-P. Chang, Y. Ding, and G. Wu, 2008: How to measure the strength of the east asian summer monsoon. *J. Climate*, **21**, 4449–4463.
- Wang, Z., 2012: Thermodynamic aspects of tropical cyclone formation. *Journal of the Atmospheric Sciences*, **69** (8), 2433–2451, doi: 10.1175/JAS-D-11-0298.1.
- Wang, Z., 2014: Role of cumulus congestus in tropical cyclone formation in a high-resolution numerical model simulation. *Journal of the Atmospheric Sciences*, **71** (5), 1681–1700, doi: 10.1175/JAS-D-13-0257.1.
- Wang, Z., M. T. Montgomery, and T. J. Dunkerton, 2010: Genesis of Pre–Hurricane Felix (2007). Part I: The Role of the Easterly Wave Critical Layer. *Journal of the Atmospheric Sciences*, doi: 10.1175/2009JAS3420.1.
- Webster, P., and S. Yang, 1992: Monsoon and enso: Selectively interactive systems. *Quart. J. Roy. Meteor. Soc.*, **118**, 877–926.
- Weightman, R. H., 1919: The west india hurricane of september, 1919, in the light of sounding observations. *Monthly Weather Review*, **47** (10), 717–721, doi: 10.1175/1520-0493(1919)47<717:TWIROS>2.0.CO;2.
- Williams, I. N., and C. M. Patricola, 2018: Diversity of enso events unified by convective threshold sea surface temperature: A nonlinear enso index. *Geophysical Research Letters*, **45** (17), 9236–9244, doi: 10.1029/2018GL079203.
- Wing, A. A., S. J. Camargo, and A. H. Sobel, 2016: Role of radiative–convective feedbacks in spontaneous tropical cyclogenesis in idealized numerical simulations. *J. Atmos. Sci.*, **73**, 2633–2642.

- Wissmeier, U., and R. K. Smith, 2011a: Tropical cyclone convection: The effects of ambient vertical vorticity. *Q. J. R. Meteorol. Soc.*, doi: 10.1002/qj.819.
- Wissmeier, U., and R. K. Smith, 2011b: Tropical cyclone convection: The effects of ambient vertical vorticity. *Quarterly Journal of the Royal Meteorological Society*, doi: 10.1002/qj.819.
- Yoshida, R., and H. Ishikawa, 2013: Environmental factors contributing to tropical cyclone genesis over the western north pacific. *Monthly Weather Review*, **141**, 451–467, doi: 10.1175/MWR-D-11-00309.1.
- Zawislak, J., and E. J. Zipser, 2014: Analysis of the Thermodynamic Properties of Developing and Nondeveloping Tropical Disturbances Using a Comprehensive Dropsonde Dataset. *Monthly Weather Review*, **142** (3), 1250–1264, doi: 10.1175/MWR-D-13-00253.1.
- Zehr, R. M., 1992: Tropical Cyclogenesis in the Western North Pacific. Ph.D. thesis, Colorado State University.
- Zhang, F., and D. Tao, 2013: Effects of vertical wind shear on the predictability of tropical cyclones. *J. Atmos. Sci.*, **70**, 975–983.